UNIVERSITY OF OKLAHOMA

GRADUATE COLLEGE

IMPROVED METHODS FOR SCALE-RESOLVED TURBULENCE MODELING IN COMPUTATIONAL FLUID DYNAMICS SIMULATIONS

A DISSERTATION

SUBMITTED TO THE GRADUATE FACULTY

In partial fulfillment of the requirements for the

Degree of

Doctor of Philosophy

By

Olalekan O. Shobayo
Norman, Oklahoma
2021

IMPROVED METHODS FOR SCALED-RESOLVED TURBULENCE

MODELING

IN COMPUTATIONAL FLUID DYNAMICS SIMULATIONS

A DISSERTATION APPROVED FOR THE SCHOOL OF AEROSPACE AND MECHANICAL ENGINEERING

BY THE COMMITTEE CONSISTING OF

Dr. D. Keith Walters, Chair

Dr. Edgar O'Rear

Dr. Jivtesh Garg

Dr. Hamidreza Shabgard

Dr. Prakash Vedula

Dr. Keisha B. Walters

ABSTRACT

The present study presents improved methods for modeling turbulent fluid flow and heat transfer within the context of computational fluid dynamics (CFD) simulations. Specifically, the study proposes and investigates two novel methods for improved turbulent flow simulation. The first is an improved method for blending the Reynolds-averaged Navier-Stokes (RANS) and large-eddy simulation (LES) components within the dynamic hybrid RANS-LES (DHRL) modeling framework. The objective is to improve the performance of the DHRL model for prediction of turbulent heat transfer for cases in which the mean velocity and mean temperature gradients are not well aligned. Analysis of the current baseline version of DHRL shows that significant error can arise in such a situation, and the new method is specifically designed to address this shortcoming. The second new contribution is a method for generating synthetic turbulence to provide initial and/or boundary conditions in scale-resolving CFD simulations that adopt either an LES or hybrid RANS-LES modeling approach. Each of these methods is investigated for canonical flow test cases which are intended to highlight their potential strengths and weaknesses. The results of these investigations are presented in a series of chapters that correspond to published or submitted manuscripts, each of which focuses on one particular aspect of the overall research plan.

In order to investigate the newly proposed DHRL blending function, simulations are performed for an idealized fully-developed planar channel flow case for which the mean velocity gradient is non-zero only in the wall-normal direction, and the mean temperature gradient is imposed to be uniform and non-zero in the streamwise or spanwise direction. Turbulent heat flux predictions are obtained for three different classes of modeling approach: Reynolds-averaged Navier-Stokes (RANS), large-eddy simulation (LES), and hybrid RANS-LES. Results are compared to available DNS data at Prandtl number of 0.71 and Reynolds number of 180 based on

friction velocity and channel half-width. Specific models evaluated are the k-ω SST RANS model, monotonically integrated LES (MILES), delayed detached eddy simulation (DDES), improved delayed detached eddy simulation (IDDES), and dynamic hybrid RANS-LES (DHRL). The DHRL model includes both the standard formulation that has been previously documented in the literature as well as the new modified version developed specifically to improve predictive capability for flows in which the primary mean velocity and mean temperature gradients are not closely aligned. The modification consists of using separate RANS-to-LES blending parameters in the momentum and energy equations. Results are interrogated to evaluate the performance of the three different model types and specifically to evaluate the performance of the new modified DHRL variant compared with the baseline version. Overall, the modified variant of DHRL, relative to IDDES, DDES and baseline DHRL (hybrid RANS-LES models) showed improved performance in predicting turbulent heat flux both in streamwise and spanwise directions.

The new proposed method for synthetic turbulence generation—denoted as statistically targeted forcing (STF)—seeks to introduce a fluctuating velocity field with a distribution of first and second moments that match a user-specified target mean velocity and Reynolds stress tensor, by incorporating deterministic time-dependent forcing terms into the momentum equation for the resolved flow. The STF method is formulated to extend the applicability of previously documented methods and provide flexibility in regions where synthetic turbulence needs to be generated or damped, for use in engineering level large-eddy and hybrid large-eddy/Reynolds-averaged Navier-Stokes CFD simulations. The performance of the proposed STF method is evaluated in LES simulations of isotropic and anisotropic homogeneous turbulent flow, spatially-developing freestream turbulence, and temporally-developing mixing layer test cases. Results are interrogated and compared to target statistical velocity and turbulent stress distributions and

evaluated in terms of energy spectra. Analysis of the influence of STF model parameters, mesh resolution, and LES subgrid stress model on the results is investigated. Overall, results show that the new STF method can successfully reproduce desired target statistical distributions, reproduces spectral energy distributions consistent with the known characteristics of three-dimensional turbulence, and allows control of the characteristic integral length scale via the use of spatial filtering.

ACKNOWLEDGEMENTS

First, I am thankful to my God for all His blessings, grace, mercy, guidance, and comfort that He has bestowed upon me throughout my life. I also extend my gratitude to my parents and siblings who have been supportive throughout their lives to give me a better future.

I am also very thankful for my wife, Temitope Shobayo, for her relentless, invaluable support throughout the years that I have known her. Furthermore, I would like to thank the rest of my family members for their consistent motivation and support.

I would also like to thank my research colleagues and friends for their expertise, support and help throughout my graduate program and research. I am so glad and thankful to have such wonderful colleagues and friends.

The computing for this project was performed at the OU Supercomputing Center for Education & Research (OSCER) at the University of Oklahoma (OU). My sincere gratitude to OSCER team support.

I also extend my gratitude to my committee members, who have been very supportive, flexible and accommodating throughout my graduate program and research.

Finally, I would also like to thank my advisor and mentor, Dr. Keith Walters, for all his invaluable support throughout my graduate program. He has provided positive direction and rock-solid support to me in my professional and personal development. His professional guidance, work ethic, kindness, and intellectual curiosity has positively impacted my work. He is the best advisor any student can ask for. I am extremely grateful to him for his continual support and patience.

TABLE OF CONTENTS

ABSTRACT..... ……iv

ACKNOWLEDGEMENTS..... vii

TABLE OF CONTENTS..... viii

LIST OF PUBLICATIONS..... xiv

LIST OF FIGURES..... xvii

LIST OF TABLES..... xxviii

NOMENCLATURE..... xxix

CHAPTER I

INTRODUCTION.....1

CHAPTER II

OBJECTIVES AND RESEARCH OUTLINE.....7

2.1.Hybrid RANS-LES Simulation of Turbulent Heat Transfer in a Channel Flow 7

2.2.Homogeneous Synthetic Turbulence Generation 8

2.3.Freestream Synthetic Turbulence Generation 9

2.4.Synthetic Generation of Initial Conditions for Temporally-Developing Turbulent Mixing Layer 10

CHAPTER III

A NEW ENERGY BLENDING FORMULATION : HYBRID RANS-LES SIMULATION OF TURBULENT HEAT TRANSFER IN A CHANNEL FLOW WITH IMPOSED SPANWISE AND STREAMWISE MEAN TEMPERATURE GRADIENT 11

3.1. Introduction 11

3.2. Simulation Details 15

3.2.1. Governing Equations 16

3.2.2. Shear-Stress Transport (SST) *k*-w Model 17

3.2.3. Monotonically Integrated LES (MILES) Model Formulation 18

3.2.4. Detached Eddy Simulation (DES) Model 19

3.2.5. Dynamic Hybrid RANS-LES (DHRL) Model 20

3.2.5.1. Baseline DHRL Formulation 20

3.2.5.2. Modified DHRL Formulation 23

3.2.6. Boundary and Forcing Conditions. 25

3.2.7. Computational Grid 28

3.2.8. Computational Fluid Dynamics Solver 30

3.3. Results and Discussion 31

3.3.1. Mean and Fluctuating Velocity 31

3.3.2. Streamwise Mean Temperature Gradient Test Case 38

3.3.3. Spanwise Mean Temperature Gradient Test Case 44

3.3.4. Summary of Model Performance and Cost 47

3.4. Summary and conclusion 49

CHAPTER IV

A NEW STATISTICALLY TARGETED FORCING (STF) FORMULATION: EVALUATION OF A STATISTICALLY TARGETED FORCING METHOD FOR SYNTHETIC TURBULENCE GENERATION IN SCALE-RESOLVING SIMULATIONS..... 52

4.1. Introduction 52

4.2. Statistically Targeted Forcing Method 56

4.2.1. General Description of the Method.....56

4.2.2. Ensemble Averaging 60

4.2.3. Spatial Filtering.....61

4.2.4. Prescription of the Forcing Time Scale.....63

4.3. Simulation Details 64

4.4. Test Cases.....65

4.5. Results and Discussion.....68

4.5.1. Homogeneous Isotropic Turbulence 68

4.5.1.1. Baseline Results. 69

4.5.1.2. Effect of Averaging Technique 78

4.5.1.3. Effect of Spatial Filtering 82

4.5.2. Homogeneous Anisotropic Turbulence 91

4.6. Summary and Conclusion 96

CHAPTER V

SCALE-RESOLVING SIMULATIONS OF A STATISTICALLY TARGETED FORCING METHOD FOR SYNTHETIC TURBULENCE GENERATION IN A FREESTREAM TURBULENCE. 99

5.1. Introduction 99

5.2. Simulation Details 104

5.2.1. STF Method Formulation 105

5.2.2. Spatial Filtering 109

5.2.3. Shear-Stress Transport (SST) Model 112

5.2.4. Monotonically Integrated LES (MILES) and LES Subgrid Stress Model. 113

5.2.5. Dynamic Hybrid RANS-LES (DHRL) Formulation 114

5.2.6. FST Channel Flow (FST-CF) Test Case. 116

5.2.7. STF Forcing Region with Boundary and Initial (B/I) Conditions 118

5.2.8. Computational Fluid Dynamics Solver 118

5.2.9. Computational Grid 119

5.3. Result and Discussion 120

5.3.1. Instantaneous and Mean velocity 122

5.3.2. Streamwise Normal Reynold Stress. 125

5.3.3. Turbulent Kinetic Energy 127

5.3.4. Effect of Mesh Resolution 132

5.3.5. Effect of Forcing Coefficient. 135

5.3.6. Effect of Explicit LES modelling and Spatial filtering. 140

5.3.7. Effect of Time-scale Coefficient 145

5.4. Summary and Conclusions 149

CHAPTER VI

STATISTICALLY TARGETED FORCING (STF) METHOD FOR SYNTHETIC TURBULENCE GENERATION OF INITIAL CONDITIONS IN TEMPORALLY-DEVELOPING TURBULENT MIXING LAYER FLOW 152

6.1. Introduction 152

6.2. STF Method Formulation 156

6.2.1. General Description of the Method 156

6.2.2. Prescription of the Forcing Time scale 161

6.2.3. Ensemble Averaging 162

6.3. Simulation Details 163

6.3.1. Computational Fluid Dynamics Solver 164

6.3.2. Temporally-Developing TML Test Case 165

6.4. Result and Discussion 168

6.4.1. Instantaneous and Mean Velocity. 172

6.4.2. Resolved Turbulent Stress. 175

6.4.3. Energy Spectrum 177

6.4.4. Effect of Mesh Resolution 178

6.4.5. Effect of Forcing Coefficient 183

6.4.6. Effect of Subgrid Stress Modeling 188

6.5. Summary and Conclusion 190

CHAPTER VII

CONCLUSIONS & FUTURE WORK 192

7.1. Summary 192

7.2. Conclusions 196

7.3. Future Work 199

LIST OF REFERENCES 201

LIST OF PUBLICATIONS

This dissertation is presented as an integrated accumulation of five scientific American Society of Mechanical Engineers (ASME) publications. The first manuscript has been published in a peer-reviewed journal and the other three have been published in ASME Conferences and improved versions submitted for publication in peer-reviewed journals.

Published manuscripts

Peer-reviewed journal:

- Chapter III: **Shobayo, O. O.,** and Walters, D. K., 2021. "Hybrid RANS–LES Simulation of Turbulent Heat Transfer in a Channel Flow with Imposed Streamwise or Spanwise Mean Temperature Gradient," *J. Fluids Eng*., 143(8): 081104, doi:10.1115/1.4051067.

Conference publications:

- Not included in the dissertation: **Shobayo, O. O.,** and Walters, D. K., 2018. "Evaluation of Performance and Code-to-code Variation of a Dynamic Hybrid RANS/LES Model for Simulation of Backward-facing Step Flow," *Proceedings of the ASME 2018 5th Joint US-European Fluids Engineering Division Summer Meeting*. *Volume 1*: V001T08A002, doi:10.1115/FEDSM2018-83160.
- Chapter III: **Shobayo, O. O.,** and Walters, D. K., 2019. "Hybrid RANS–LES Simulation of Turbulent Heat Transfer in a Channel Flow With Imposed Streamwise or Spanwise Mean Temperature Gradient," *Proceedings of the ASME-JSME-KSME 2019 8th Joint Fluids Engineering Conference. Volume 2*: V002T02A052, doi: 10.1115/AJKFluids2019-4920.

- Chapter IV: **Shobayo, O. O.,** and Walters, D. K., 2020. " Evaluation of a Statistically Targeted Forcing Method for Synthetic Turbulence Generation in Large-Eddy Simulations and Hybrid RANS-LES Simulations," *Proceedings of the ASME 2020 Fluids Engineering Division Summer Meeting. Volume 3*: V003T05A043, doi: 10.1115/FEDSM2020-20376.

Submitted and in progress manuscripts

Peer-reviewed journals:

- Chapter IV: **Shobayo, O. O.,** and Walters, D. K., 2021. "Evaluation of a Statistically Targeted Forcing Method for Synthetic Turbulence Generation in Large-Eddy Simulations and Hybrid RANS-LES Simulations," submitted to *J. Fluids Eng*.
- Chapter V: **Shobayo, O. O.,** and Walters, D. K., 2021. "Scale-Resolving Simulations of a Statistically Targeted Forcing Method for Synthetic Turbulence Generation in Freestream Turbulence," submitted to *J. Fluids Eng*.

  Not included in the dissertation: **Shobayo, O. O.,** and Walters, D. K., 2021. "Statistically Targeted Forcing (STF) Method for Synthetic Turbulence Generation of Scale-resolving Simulations for a Turbulent Channel Flow," expected submission Fall 2021.

Conference publications

Chapter VI: **Shobayo, O. O.,** and Walters, D. K., 2021. " Statistically Targeted Forcing (STF) Method for Synthetic Turbulence Generation of Initial Conditions in Three-Dimensional Turbulent Mixing Layer Flow," presented at the *ASME Fluids Engineering Division Summer Meeting FEDSM 2021*: FEDSM2021-65916, publication in progress.

- Not included in the dissertation: Tausif J., **Shobayo, O. O.,** and Walters, D. K., 2018. " A New Variant of the Dynamic Hybrid Rans-Les Model for Complex Turbulent Flows," submitted for presentation and publication at the *ASME International Mechanical Engineering Congress and Exposition IMECE 2021*: IMECE2021-72185.

LIST OF FIGURES

CHAPTER III

Figure 1: Illustration of computational mesh 29

Figure 2: Mean velocity profiles on (a) coarse grid, and (b) refined grid for SST, DHRL, DDES, and IDDES models 32

Figure 3: Contours of instantaneous and mean velocity on coarse grid (left), and refined grid (right) for (a) SST, (b) DHRL (c) DDES, and (d) IDDES models 32

Figure 4: Predicted root mean square (RMS) of fluctuating velocity components in the streamwise (u'), wall-normal (v'), and spanwise (w') directions on coarse and refined grids for the hybrid RANS-LES models used in this study.....34

Figure 5: Turbulent Kinetic Energy (TKE) profiles of (a)coarse grid, and (b)refined grid across the channel width for SST and hybrid RANS-LES models.....36

Figure 6: Mean velocity profiles on coarse and refined grids, highlighting mesh sensitivity for (a) SST, (b) DHRL, (c) DDES, and (d) IDDES models 37

Figure 7: Mean temperature profiles for SST and hybrid RANS-LES models on (a) coarse grid, and (b) refined grid 38

Figure 8: Contours of Instantaneous and mean excess temperature (θ) on coarse grid (left), and refined grid (right) for (a) SST, (b) DHRL, (c) DDES, and (d)IDDES model 39

Figure 9: Root mean square (RMS) fluctuating temperature profiles on (a)coarse grid, and (b)refined grid with imposed streamwise mean temperature gradient for DHRL, DDES, and IDDES models compared with DNS data of Kawamura et al. [29] and Kasagi et al. [34] 41

Figure 10: Streamwise turbulent heat flux profile on (a)coarse grid, and (b)refined grid for SST, DHRL, DDES, and IDDES models 42

Figure 11: Predicted Nusselt number compared to DNS data [50] 43

Figure 12: Fluctuating temperature profiles on (a)coarse grid, and (b)refined grid with imposed spanwise mean temperature gradient for DHRL, DDES, and IDDES models 46

Figure 13: Spanwise turbulent heat flux profile on (a)coarse grid, and (b)refined grid for SST, DHRL, DDES, and IDDES models 47

CHAPTER IV

Figure 14: Planar view of the computational grids for homogeneous turbulence cases showing four mesh resolution levels (a) 32^3, (b) 64^3, (c) 128^3, and (d) 192^3 67

Figure 15: Contours of instantaneous velocity magnitude for forcing simulation of homogeneous isotropic turbulence with forcing time scale $\tau_f = 0.045$, taken at a simulation time $t = 2\tau_s$. Four mesh resolution levels are shown: (a) 32^3, (b) 64^3, (c) 128^3, and (d) 192^3 .71

Figure 16: Planar view contours of instantaneous velocity magnitude for forcing simulation of homogeneous isotropic turbulence on 128^3 mesh, taken at a simulation time $t = 2\tau_s$. Results are shown for three different values of the forcing time scale.....72

Figure 17: Time evolution of turbulent kinetic energy (k/k^*) for forcing simulation of homogeneous isotropic turbulence with volume averaging and no spatial filtering: (a) effect of mesh resolution, (b) effect of forcing time scale. 73

Figure 18: Ratio of resolved-to-target turbulent kinetic energy, k/k^* for (a) different mesh sizes and (b) on 128^3 mesh at different values of the forcing time scale parameter τ_f. 74

Figure 19: Normalized energy density spectrum for forcing simulation of homogeneous isotropic turbulence with volume averaging on (a) different meshes at $C_f = 10, \tau_f = 0.45$, (b) 128^3 mesh, $\tau_f = 0.45, 0.045, 0.0045$ and 0.00033. Similar profiles to that of Fig. 18. 76

Figure 20: (a) Contours of instantaneous velocity magnitude and (b) normalized energy spectra for implicit LES simulation with no subgrid stress model, on the 128^3 grid, using three different values of τ_f. 77

Figure 21: Contours of instantaneous velocity magnitude for forcing simulation of homogeneous isotropic turbulence using volume-averaging (VA, above) and time-averaging (TA, below)
to compute turbulence statistics on 128^3 grid at $\tau_f = 4.5, 0.45$ and 0.045. 79

Figure 22: Time evolution of turbulent kinetic energy, k/k^* for forcing simulation of homogeneous isotropic turbulence using volume-averaging (VA, black) and time-averaging (TA, red) to compute turbulence statistics on 128^3 grid, at $\tau_f = 4.5, 0.45$ and 0.045. 80

Figure 23: Normalized energy spectra for forcing simulation of homogeneous isotropic turbulence using volume-averaging (VA, black) and time-averaging (TA, red) to compute turbulence statistics on 128^3 grid at $\tau_f = 4.5, 0.45$ and 0.045.....81

Figure 24: Contours of instantaneous velocity magnitude for forcing simulation of homogeneous isotropic turbulence, comparing results of (a) spatially filtered with (b) non-spatially filtered simulations, on 128^3 grid, ($\tau_T / \tau_s = 0.45$ and $C_f = 100$). 83

Figure 25: Time evolution of turbulent kinetic energy, k/k^* for forcing simulation of homogeneous isotropic turbulence, comparing results of spatially filtered (*SF*) with non-spatially filtered (*Non_SF*) simulations, on 128^3 grid ($\tau_T/\tau_s = 0.45$ and $C_f = 100$).....84

Figure 26: Normalized energy spectra for forcing simulation of homogeneous isotropic turbulence, comparing results of spatially filtered (*SF*) with non-spatially filtered (*Non_SF*) simulations, on 128^3 grid, using volume-averaging results at $\tau_T/\tau_s = 0.45$ and $C_f = 100$. 85

Figure 27: Contours of instantaneous velocity magnitude for forcing simulation of homogeneous isotropic turbulence, with different time-scale targets (τ_T), imposing different turbulent length scales (l_s), on 128^3 grid, using volume-averaging results with $C_f = 10$, at (a) $\tau_T/\tau_s = 0.056$, (b) $\tau_T/\tau_s = 0.112$, (c) $\tau_T/\tau_s = 0.225$, (d) $\tau_T/\tau_s = 0.45$, and (e) $\tau_T/\tau_s = 0.45$, $C_f = 100$. 86

Figure 28: Time evolution of turbulent kinetic energy, k/k^* for forcing simulation of homogeneous isotropic turbulence, with different time-scale targets (τ_T), imposing different turbulent length scales (l_s), on 128^3 grid, using volume-averaging results with $C_f = 10$, and 100, at $\tau_T/\tau_s = 0.056, 0.112, 0.225$ and 0.45. 87

Figure 29: Normalized energy spectra for forcing simulation of homogeneous isotropic turbulence, with different time-scale targets (τ_T), imposing different turbulent length scales (l_s) , on 128^3 grid, using volume-averaging results with (a) $C_f = 10$, at $\tau_T/\tau_s = 0.056, 0.112, 0.225$ and 0.45 and (b) $C_f = 100$, and $C_f = 10$ at $\tau_T/\tau_s = 0.45$.....88

Figure 30: Contours of instantaneous velocity magnitude for forcing simulation of homogeneous anisotropic turbulence with volume averaging, on 128^3 grid, for zero shear stress (ZSS)

results (left) with τ_f/τ_s = 4.5 and 0.45 and imposed finite shear stress (FSS) results (right) with τ_f/τ_s = 4.5 and 0.45. 93

Figure 31: Time evolution of turbulent kinetic energy, k/k^* for forcing simulation homogeneous anisotropic turbulence with volume averaging, on 128^3 grid, (a) zero shear stress (ZSS) results, at τ_f/τ_s = 0.45 and 0.045, (b) ZSS and FSS results, at τ_f/τ_s = 0.45, and (c) ZSS and FSS results, at τ_f/τ_s = 4.5. 94

Figure 32: Normalized energy spectra for forcing simulation of homogeneous anisotropic turbulence with volume averaging, on 128^3 grid, (a) zero shear stress (ZSS) at τ_f/τ_s = 0.45 and 0.045, (b) ZSS and finite shear stress (FSS) results, at τ_f/τ_s = 0.45, and (c) ZSS and FSS results, at τ_f/τ_s = 4.5. 95

CHAPTER V

Figure 33: FST-CF Computational domain. 117

Figure 34: Illustration of initial and boundary conditions, STF forcing and development regions 119

Figure 35: 2D-view computational (a) coarse grid, and (b) refined grid. 120

Figure 36: Contours of streamwise instantaneous velocity for forcing simulation of freestream turbulence with $\tau_f/\tau_\infty = 0.045$ using MILES, and DHRL models: (a) 3D view; (b) 2D yz-plane view at different streamwise locations. 124

Figure 37: Contours of streamwise normal Reynolds stress ($\overline{u_1'u_1'}$) for forcing simulation of freestream turbulence with $\tau_f/\tau_\infty = 0.045$, using MILES and DHRL models. 125

Figure 38: Spatial evolution of normalized resolved normal stress $\overline{(u_1'u_1'}/\overline{(u_1'u_1'}^*)$ for forcing simulation of freestream turbulence with $\tau_f/\tau_\infty = 0.045$ using SST, MILES, and DHRL models to compute turbulence statistics. 127

Figure 39: Contours of resolved turbulent kinetic energy (k) for forcing simulation of freestream turbulence with $\tau_f/\tau_\infty = 0.045$ using SST, MILES, and DHRL models to compute turbulence statistics. 128

Figure 40: Spatial evolution of normalized turbulent kinetic energy (k/k^*) for forcing simulation of freestream turbulence with $\tau_f/\tau_\infty = 0.045$ using SST, MILES, and DHRL models. 129

Figure 41: Time evolution of normalized turbulent kinetic energy (k/k^*) for forcing simulation of freestream turbulence with $\tau_f/\tau_\infty = 0.045$ during the first 0.5 second of the simulation time. 130

Figure 42: Energy density spectra for forcing simulation of freestream turbulence with $\tau_f/\tau_\infty = 0.045$, using MILES at different streamwise locations corresponding to the middle of the forcing region (a), the downstream edge of the forcing region (b) and the downstream decay region (c). 131

Figure 43: Contours of streamwise instantaneous (u_1) and mean velocity ($\bar{u}_1$) for forcing simulation of freestream turbulence with $\tau_f/\tau_\infty = 0.045$ using MILES to compute turbulence statistics on (a) coarse, and (b) refined grids. 133

Figure 44: Energy density spectra for forcing simulation of freestream turbulence with $\tau_f/\tau_\infty = 0.045$, using MILES on both coarse and refined grids at different streamwise locations corresponding to the middle of the forcing region (a), the downstream edge of the forcing region (b) and the downstream decay region (c). 134

Figure 45: Contours of instantaneous (u_1) and mean velocity ($\bar{u}_1$) for forcing simulation of freestream turbulence using MILES at (a) $\tau_f/\tau_\infty = 4.5$, (b) $\tau_f/\tau_\infty = 0.45$, and (c) $\tau_f/\tau_\infty = 0.045$. 136

Figure 46: Spatial evolution of normalized turbulent kinetic energy (k/k^*) for forcing simulation of freestream turbulence using MILES at forcing time scales of $\tau_f/\tau_\infty = 4.5$, 0.45, and 0.045. 137

Figure 47: Energy density spectra for forcing simulations of freestream turbulence with three different values of the forcing coefficient using MILES at downstream locations corresponding to the middle of the forcing region (a), the downstream edge of the forcing region (b), and the downstream decay region (c). 139

Figure 48: Contours of instantaneous velocity for forcing simulation of freestream turbulence with forcing time scale $\tau_f/\tau_\infty = 0.045$ and two different LES SGS methods: (a) spatially filtered, and (b) non-spatially filtered. 142

Figure 49: Energy density spectra for forcing simulation of freestream turbulence with spatially (SF) and non-spatially (NS) filtered velocity using MILES and Smagorinsky models at: (a) $x/\delta = 1$, (b) $x/\delta = 2$, and (c) $x/\delta = 6.4$. 144

Figure 50: Spatial evolution of normalized turbulent kinetic energy $\left(\frac{k}{k^*}\right)$ for forcing simulation of freestream turbulence with spatially (SF) and non-spatially (NS) filtered velocity using MILES and Smagorinsky models. 145

Figure 51: Contours of instantaneous streamwise velocity for forcing simulation of freestream turbulence using MILES, $C_f = 100$, and three different filter time scales: (a) $\tau_T/\tau_\infty = 1.12$, (b) $\tau_T/\tau_\infty = 2.25$, and (c) $\tau_T/\tau_\infty = 4.5$. 146

Figure 52: Spatial evolution of normalized turbulent kinetic energy (k/k^*) for forcing simulation of freestream turbulence using MILES, $C_f = 100$, and three different filter time scales. 147

Figure 53: Energy density spectra for forcing simulation of freestream turbulence using MILES, $C_f = 100$, and three different filter time scales**.** 147

CHAPTER VI

Figure 54: Computational domain for the temporally-developing turbulent mixing layer (TTML) [8]. 168

Figure 55: Front view of the computational grids used for TTML simulations: (a) coarse, and (b) refined. 168

Figure 56: Contours of instantaneous velocity magnitude with maximum value (Vmax) indicated, and streamwise mean velocity $(\bar{u}_1)$ for forcing simulation of TTML for $C_f = 1, \tau_s =$ 1140, 1480, 1700, 2040, 2400 on refined grid. 173

Figure 57: Contours of streamwise instantaneous velocity (u_1) for forcing simulation of temporally-developing turbulent mixing layer at $C_f = 1$, $\tau_s =$ 1480, 1700, 2040, 2400. 174

Figure 58: Mean streamwise velocity for forcing simulation of temporally-developing turbulent mixing layer at $C_f = 1, \tau_s = 1140$, 1480, 1700, 2040, 2400, 2520 and target state on refined grid. 175

Figure 59: Contours of (a) streamwise $\overline{u_1' u_1'}$, (b) vertical $\overline{u_2' u_2'}$, and (c) spanwise $\overline{u_3' u_3'}$ normal stress, and (d) Reynolds shear stress $\overline{u_1' u_2'}$ for forcing simulation of temporally-developing turbulent mixing layer at $C_f = 1, \tau_s = 2040$ on refined grid. 176

Figure 60: (a) Streamwise (b) vertical and (c) spanwise root mean square (RMS) velocity, and (d) Reynolds shear stress for forcing simulation of temporally-developing turbulent mixing layer at $C_f = 1, \tau_s = 1140$, 1480, 1700, 2040, 2400, 2520 and target state on refined grid. 177

Figure 61: One dimensional energy spectra for forcing simulation of temporally-devolving turbulent mixing layer at $C_f = 1, \tau_s = 1140$, 1480, 1700, 2040, 2400, and 2520 on refined grid.....178

Figure 62: Contours of instantaneous velocity magnitude for forcing simulation of temporally-developing turbulent mixing layer at $C_f = 1$, and $\tau_s =$ 2040 on coarse and refined grids. 179

Figure 63: Mean streamwise velocity for forcing simulation of temporally-developing turbulent mixing layer at $C_f = 1$, and $\tau_s =$ 2040 on coarse and refined grid. 180

Figure 64: Contours of streamwise normal stress, $\overline{u_1' u_1'}$ for forcing simulation of temporally-developing turbulent mixing layer at $C_f = 1$, and $\tau_s = 2040$ on coarse and refined grids.....181

Figure 65: (a) Streamwise (b) vertical and (c) spanwise root mean square (RMS) velocity, and (d) RMS velocity of Reynolds shear stress for forcing simulation of temporally-developing turbulent mixing layer at $C_f = 1$ and $\tau_s = 2040$ on coarse and refined grids. 182

Figure 66: One dimensional energy spectra $(\overline{u_1' u_1'})$ for forcing simulation of temporally-developing turbulent mixing layer at $C_f = 10$, and $\tau_s = 2040$ on coarse and refined grids. 183

Figure 67: Contours of instantaneous velocity magnitude with maximum value (Vmax) indicated, for forcing simulation of temporally-developing turbulent mixing layer at $C_f = 0.1, 1, 10$, and $\tau_s = 2040$ on coarse and refined grids. 184

Figure 68: Mean streamwise velocity for forcing simulation for forcing simulation of temporally-developing turbulent mixing layer at $C_f = 0.1, 1, 10$, and $\tau_s = 2040$ on coarse and refined grids. 184

Figure 69: Contours of streamwise normal stress, $\overline{u_1' u_1'}$ for forcing simulation of temporally-developing turbulent mixing layer at $C_f = 0.1, 1, 10$, and $\tau_s = 2040$ on coarse and refined grids. 185

Figure 70: Streamwise root mean square (RMS) velocity for forcing simulation of temporally-developing turbulent mixing layer at $C_f = 0.1, 1, 10$, and $\tau_s = 2040$ on coarse and refined grids. 187

Figure 71: One dimensional energy spectra for forcing simulation of temporally-developing turbulent mixing layer at $C_f = 0.1, 1, 10$, and $\tau_s = 2040$. 188

Figure 72: Contours of instantaneous velocity magnitude with maximum value (Vmax) indicated for forcing simulation of temporally-developing turbulent mixing layer at $\tau_s = 2040$, and $C_f = 1$ using MILES and Smagorinsky (SMAG) model on refined grid 189

Figure 73: Mean streamwise velocity for forcing simulation of temporally-developing turbulent mixing layer at $\tau_s = 2040$, and $C_f = 1$ using MILES and Smagorinsky (SMAG) model on refined grid. 189

Figure 74: Streamwise RMS velocity for forcing simulation of temporally-developing turbulent mixing layer at $\tau_s = 2040$, and $C_f = 1$ using MILES and Smagorinsky (SMAG) model on refined grid. 190

LIST OF TABLES

Table 1: Domain size and mesh resolution cell lengths ($\Delta x, \Delta y$ and Δz) 29

Table 2: Relative error in predicted Nusselt number for streamwise temperature gradient test case. 44

Table 3: Relative error of streamwise and spanwise turbulent heat flux peak-value analysis on refined grid.....48

Table 4: Percentage ratio of resolved-to-target turbulent kinetic energy for different averaging techniques and forcing time scales at $t = 3\tau_s$. 82

Table 5: Summary of turbulence statistics for Homogeneous Isotropic STF cases. 90

Table 6: Summary of turbulence statistics for Homogeneous Anisotropic STF cases. 96

Table 7: Summary of Freestream turbulence (FST) statistics for STF cases at x/δ =2. 122

Table 8: Summary of energy spectrum statistics for STF cases at x/δ =*1,* 2 and 6.4. 148

Table 9: Summary of target peak turbulence statistics for temporally-developing turbulent mixing layer. 171

NOMENCLATURE

Θ ..... Excess temperature

T ..... Temperature

q_w ..... Instantaneous local wall heat flux

$\langle q_w \rangle$ ..... Mean wall heat flux

u, v, w ..... Streamwise, wall-normal, and spanwise velocity

θ_f ..... Friction temperature

u_τ ..... Friction velocity

θ_w ..... Excess wall temperature

ν_t ..... Eddy viscosity

c_v ..... Specific heat at constant volume

c_p ..... Specific heat at constant pressure

δ ..... Channel half-height

ν ..... Kinematic viscosity

T_w ..... Wall temperature

τ_w ..... Wall shear stress

Re_τ ..... Reynolds number based u_τ and δ

t ..... Time

x, y, z ..... Streamwise, wall-normal and spanwise directions

$(\emptyset)^+$ ..... Non-dimensionalization of variables with u_τ, δ, ν or $\langle q_w \rangle$ or θ_f

$(\emptyset)'$ ..... Fluctuating variable

$\overline{(\emptyset)}$ ..... Ensemble averaged variable

$\langle u \rangle$ ..... Mean time-averaged streamwise velocity

$\langle w \rangle$ ..... Mean time-averaged spanwise velocity

U_m ..... Bulk velocity

T_m ..... Bulk temperature

ρ ..... Density

Pr_t ..... Turbulent Prandtl number

Pr ..... Prandtl number

$\bar{k}_T$ ..... Turbulent thermal conductivity

α ..... Thermal diffusivity

k ..... Turbulent kinetic energy

κ ..... Thermal conductivity

CFD ..... Computational Fluid Dynamics

DNS ..... Direct Numerical Simulations

LES ..... Large Eddy Simulations

RANS ..... Reynolds-Averaged Navier-Stokes

HRL ..... Hybrid RANS-LES

DHRL ..... Dynamic Hybrid RANS-LES

DES ..... Detached Eddy Simulation

DDES ..... Delayed DES

IDDES ..... Improved Delayed DES

STG ..... Synthetic Turbulence Generation

STF ..... Statistically Targeted Forcing

CHAPTER I

INTRODUCTION

Turbulence is evident in fluid flows as diverse as chaotic flow out of a faucet to natural tornadoes in our environment where three-dimensional vorticity, momentum and heat transport are apparent. It is a property of fluid flow which is evident at high Reynolds numbers, effective on a large range of scales, and is characterized by apparently erratic motion, intermittency, 3-D vortices and filaments, irreversibility, chaos, and unpredictability [1–5]. Turbulence is common in nature and is readily found, for example, in the ocean [6], the atmosphere [7], geosciences [8], and also in climate models [9]. Qualitatively, it exhibits a three-dimensional chaotic nature that results in much larger energy dissipation, heat transfer rates, and random mixing, when compared to laminar flows. Accurate prediction of turbulent flows using the tools of mathematical analysis is therefore critically important to our understanding of both natural and man-made systems.

Claude-Louis Navier and George Gabriel Stokes derived fundamental equations, commonly referred to as the Navier-Stokes (NS) equations, which govern the behavior of fluids [10]. This set of differential equations can be used to describe the balance of forces in a fluid, and therefore makes it theoretically possible to predict the future behavior of a fluid from a given initial state. The Navier-Stokes equations have been validated on several occasions over the last two centuries and been found to accurately represent the physical reality of fluid flow systems. Unfortunately, at present, the NS equations cannot be solved analytically for most defined fluid flow problems. To date, the only way to solve the NS equations for most applications is by applying numerical methods. Turbulent flow problems are numerically solved by discretizing the Navier-Stokes equations and employing high performance computing (HPC) tools to provide approximate

solutions to real-life problems. The analysis of fluid flows using numerical computation using this approach is called Computational Fluid Dynamics (CFD). In practical engineering applications, simulation of any real-world turbulence that can successfully impact analysis and design must yield effective understanding and/or prediction of turbulent flow statistics. Because the computational cost required to accurately solve the Navier-Stokes equations directly using numerical methods alone is often beyond the limits of available computational resources, turbulence modeling becomes unavoidable for simulations of many real natural and engineered systems.

Turbulence modeling is, generally speaking, the application or use in CFD of a mathematical model other than the exact Navier-Stokes equations to yield a statistical description of turbulence. Often the equations in this model are formally similar to Navier-Stokes, with the key difference being the level of scale that can be resolved by the equation. One characteristic feature of turbulent flows is the evidence of a range of scales, where the large scale size is typically determined by the geometry of the domain or flow feature of interest, and the small scale size is determined by the fluid viscosity. Models can be described based on what portion of this range of scales is resolved by solution of the governing equation, and what portion is accounted for using statistical or phenomenological model terms.

In 1877, Joseph Valentin Boussinesq developed one of the earliest mathematical models of turbulence when he proposed the "Boussinesq eddy viscosity hypothesis" by relating turbulence stresses to the mean velocity gradients in order to close the system of model equations. In 1925, Ludwig Prandtl refined the Boussinesq model when he proposed that eddy viscosity can be approximated as a function of a "mixing length" in the turbulent boundary layer and the local mean

velocity gradient. Since then, research on methods for turbulence modeling have led to the development of a wide range of available modeling tools.

In modern CFD applications, turbulence modeling approaches are broadly classified into three different types: Reynolds Averaged Navier-Stokes (RANS), Large Eddy Simulation (LES), and Direct Numerical Simulation (DNS). RANS solves only the ensemble- or time-averaged form of the NS equations and models all scales of fluctuating turbulent motion. However, for highly complex flow problems the assumptions in traditional unsteady RANS modeling approaches are substantially limited, often introducing error in the computed solution, most especially in separated flows [11]. At the other end of the spectrum, DNS explicitly solves the Navier-Stokes equations for all scales of motion, and does not require additional modeling beyond the Navier-Stokes equations themselves (indeed it is debated whether DNS should be referred to as a type of turbulence modeling). As discussed above, however, this makes it prohibitively expensive for most flows of engineering interest due to excessive computational cost. An alternative approach is available in Large Eddy Simulation (LES), for which a filtering operation is applied to the Navier-Stokes equations. LES models only the smallest scales using a statistical description while resolving the larger, primary energy containing scales of turbulence directly. Hence, in general, it theoretically produces more accurate results than RANS for a wide range of flow configurations but is significantly less costly than DNS [12]. The theoretical accuracy of the method is directly proportional to the range of resolved scales, as is the computational expense. In the commonly viewed modeling hierarchy, LES lies between RANS and DNS in terms of both theoretical accuracy and computational cost.

Recently, an emerging class of models known as hybrid RANS-LES (HRL) models has been developed in an effort to provide a tradeoff between effectively balancing cost and accuracy. The

HRL modeling approach is theoretically more accurate than RANS and more affordable than LES, which potentially creates a competitive advantage in performance and cost compared to RANS or LES alone [13]. HRL methods can be broadly classified into 2 categories: zonal and nonzonal. For the zonal approach, a RANS model is employed in user-specified regions of the computational domain, and an LES model is employed in the remaining regions. The major challenge is the selection of interface conditions to provide seamless transition between the two regions [14,15]. The non-zonal approach, as the name suggests, is one for which the user is not required to specify the RANS and LES regions prior to the simulation, however the Reynolds stress and subgrid stress tensors differ both physically and mathematically and bridging the two effectively is still a significant research challenge [15]. The computational expense of LES and the inaccuracies of RANS for more complex flows motivated the development of hybrid RANS/LES methods. In wall bounded flows, much of the expense of LES arises due to a requirement for small cell spacing in the boundary layer. Hybrid models are relatively new in the field of turbulence modeling and have garnered the interest of many researchers. Some of the most well-known non-zonal HRL models are the Detached Eddy Simulation (DES), Delayed Detached Eddy Simulation (DDES), and Improved Delayed Detached Eddy Simulation (IDDES). Although these non-zonal HRL models have been successfully validated and utilized in the aerospace industry for complex flow simulations, most HRL models have strict grid generation requirements and can suffer from non-physical RANS-to-LES transition resulting in modeled stress depletion (MSD).

This research study focuses in large part on providing improved methods within the HRL and LES modeling framework that improve predictions of turbulent flow and heat transfer statistics, to facilitate more accurate and cost effective CFD solutions for complex scientific and engineering problems. The research presented in this study attempts to highlight some of the key

deficiencies with traditional RANS and hybrid RANS-LES models while analyzing the performance of the Dynamic Hybrid RANS-LES (DHRL) model for turbulent flow predictions.

A separate but related aspect from the formulation of the mathematical models themselves are the boundary and initial conditions for the model equations (including the Navier-Stokes equations for DNS). For Scale-Resolving Simulations (SRS), which include DNS, LES, and Hybrid RANS-LES, accurate simulation requires application of spatially varying initial conditions and temporally and spatially varying boundary conditions. In some cases, these conditions can be determined from their own separate SRS simulations. For many practical engineering simulations, however, it is computationally prohibitive to obtain time-dependent turbulence boundary and/or initial (B/I) conditions directly from turbulent flow simulations, and alternatives such as synthetic turbulence generation (STG) methods must be used. The goal of B/I condition methods such as synthetic turbulence generation (STG) is to replace turbulent content obtained from fully resolved simulations with a reasonable approximation of turbulence for a substantially lower computational cost. This research study explores synthetic turbulence generation (STG) methods as alternative to turbulence modeling since synthetic turbulence is not produced by the computationally expensive process of solving of the NS equations, but by statistical algorithms, hence computation time can be saved and complex problems can be solved using less resources. Hence, synthetic turbulent generation formulations that can effectively prescribe an appropriate level of turbulent energy and reproduce time-dependent turbulence boundary and/or initial (B/I) conditions of a turbulent flow are important tools for the study of turbulent flows. For CFD industrial applications, they allow researchers and designers to reduce the computational effort of numerical simulations of fluid flows, and thereby improve the quality of simulations for complex flow problems.

Several B/I condition methods have been proposed. One well known method for prescribing turbulence boundary conditions is recycling/rescaling. For recycled turbulent content, streamwise periodic boundary conditions are imposed on the domain or a portion of the domain such that the turbulent flow leaving the outlet is reintroduced at the inlet. This method was used, for example, by Spalart and Watmuff [16]. Several other studies have extended the recycling/rescaling approach to simulate complex wall bounded flows [17-20]. Schlüter et al. [21] used the recycling/rescaling method to impose fluctuating velocities at the outlet of an LES region of a simulation to impose the statistics obtained from a RANS solution in the downstream region. Kraichnan [22] proposed one of the first STG methods for isotropic turbulence, by utilizing a spectral approach to artificially produce an isotropic turbulent velocity field from random Fourier modes. This approach of generating isotropic velocity fields with a specified energy spectrum has been used for example to generate initial conditions for DNS of isotropic turbulence [23,24].

This study presents two novel contributions for the enhancement of scale-resolving turbulent CFD flow simulation, a synthetic turbulent generation method and a modified variant of the dynamic hybrid RANS-LES (DHRL) model. Both are evaluated using relevant canonical test cases. These novel techniques have the potential to provide significant improvement in the predictive capabilities for turbulent flow and heat transfer using scale-resolving simulations in general and the DHRL model specifically.

CHAPTER II

OBJECTIVES AND RESEARCH OUTLINE

The overall objective of this research study is the development of novel turbulence modeling methods for use in Scale-Resolving Simulations of turbulent flow, to include improvements to Hybrid RANS-LES modeling as well as development of a novel method for synthetic generation of turbulence boundary and initial conditions. The overall research effort was undertaken in the form of four separate but integrated research problems. In this section an outline is presented summarizing the four specific integrated scientific research papers (published and/or submitted) that resulted, and that comprise chapters 3, 4, 5, and 6 of this dissertation.

2.1 Hybrid RANS-LES Simulation of Turbulent Heat Transfer in a Channel Flow (Chapter III)

Computational fluid dynamics (CFD) results are presented for turbulent flow and heat transfer in a plane channel. This study investigates an idealized fully-developed planar channel flow case for which the mean velocity gradient is non-zero only in the wall-normal direction, and the mean temperature gradient is imposed to be uniform and non-zero in the streamwise or spanwise direction. The objective is to evaluate the accuracy of turbulent heat flux predictions using hybrid RANS-LES models in wall bounded flows, and to evaluate a proposed improvement to the dynamic hybrid RANS-LES (DHRL) turbulence model. Results are obtained at Prandtl number of 0.71 and Reynolds number of 180 based on wall friction velocity and channel half-height, and are compared to available DNS data and to a well validated RANS model (k-ω SST). The specific hybrid RANS-LES models investigated include delayed detached eddy simulation

(DDES), improved delayed detached eddy simulation (IDDES), and dynamic hybrid RANS-LES (DHRL). The DHRL model includes both the standard formulation that has been previously documented in the literature as well as a modified version specifically developed to improve predictive capability for flows in which the mean velocity and mean temperature gradients are not closely aligned. The modification consists of using separate RANS-to-LES blending parameters in the momentum and energy equations. Results are interrogated to evaluate the performance of the three different model types and specifically to evaluate the performance of the new modified DHRL variant compared with the baseline version.

2.2 Homogeneous Synthetic Turbulence Generation (Chapter IV)

Computational fluid dynamics (CFD) results are presented for synthetic turbulence generation using a novel statistically targeted forcing (STF) method. The new method seeks to introduce a fluctuating velocity field with a distribution of first and second moments that match a user-specified target mean velocity and Reynolds stress tensor, by incorporating deterministic time-dependent forcing terms into the momentum equation for the resolved flow. The STF method is formulated to extend the applicability of previously documented methods and provide flexibility in regions where synthetic turbulence needs to be generated or sustained, for use in engineering level large-eddy and hybrid large-eddy/Reynolds-averaged Navier-Stokes CFD simulations. The objective of this study is to evaluate the performance of the proposed STF method in LES simulations of isotropic and anisotropic homogeneous turbulent flow test cases. Results are interrogated and compared to target statistical velocity and turbulent stress distributions and evaluated in terms of energy spectra. Analysis of the influence of STF model parameters, mesh resolution, and LES subgrid stress model on the results is investigated. Results show that the new

method can successfully reproduce desired statistical distributions in a homogeneous turbulent flow.

2.3 Freestream Synthetic Turbulence Generation (Chapter V)

Computational fluid dynamics (CFD) results for synthetic turbulence generation (STG) of freestream turbulence by a proposed statistically targeted forcing (STF) method in a prototypical channel domain are presented. The STF method was previously documented for homogeneous isotropic and anisotropic turbulence (Chapter III) and formulated to introduce a fluctuating velocity field with a distribution of first and second moments that match a user-specified target mean velocity and Reynolds stress tensor, by incorporating deterministic time-dependent forcing terms into the momentum equation for the resolved flow. Previous studies have documented synthetic generation of freestream turbulence as a boundary and/or initial (B/I) condition far upstream of a computational domain, but limited investigation exists in synthetically generating and/or maintaining turbulence within a spatially developing flow-domain. This study extends applicability of the STF method to generation of freestream turbulence in scale-resolving simulations, where flow is spatially developing. The method provides flexibility in regions where synthetic turbulence needs to be generated or damped, for use in engineering level scale-resolving simulations such as Reynolds-averaged Navier-Stokes (RANS), large-eddy simulation (LES), and hybrid RANS-LES.

2.4 Synthetic Generation of Initial Conditions for Temporally-Developing Turbulent Mixing Layer (Chapter VI)

Computational fluid dynamics (CFD) results are presented for synthetic turbulence generation of initial conditions for the canonical test case of a temporally-developing turbulent mixing layer (TTML) flow. This numerical study further investigates the performance of the newly proposed Statistically Targeted Forcing (STF) method, and its capability to act as a restoring force to match the target mean velocity and turbulent stress distribution of the initial state of a temporally-developing flow where highly unsteady destabilizing mechanisms and influence are evident. Several previous investigations exist documenting vortex dynamics of the turbulent mixing layer, but limited investigations exist on synthetic turbulence generation forcing methods to prescribe initial conditions. The objective of this study is to evaluate the performance of the newly proposed STF method to capture the vortex dynamics and effectively match target mean velocity and resolved turbulent stress predictions using large-eddy simulation. Results are interrogated and compared to statistical velocity and turbulent stress distributions obtained from DNS simulations available in the literature. Results show that the STF method can successfully reproduce desired statistical distributions in a turbulent mixing layer flow.

CHAPTER III

A NEW ENERGY BLENDING FORMULATION : HYBRID RANS-LES SIMULATION OF TURBULENT HEAT TRANSFER IN A CHANNEL FLOW WITH IMPOSED SPANWISE AND STREAMWISE MEAN TEMPERATURE GRADIENT

Work from this chapter has been published in the ASME Journal of Fluids Engineering (JFE).

3.1. INTRODUCTION

Heat transfer in turbulent wall bounded flows is important in many engineering applications including nuclear reactors, heat exchangers, and gas turbines. Typically heat transfer in the wall-normal direction is of primary importance since it directly dictates convective heat transfer rate, but wall parallel heat transfer may also significantly impact overall system performance. For analysis and design purposes, computational fluid dynamics (CFD) prediction of spanwise or streamwise turbulent heat transfer in turbulent boundary layer flow remains a challenging problem. This is in part due to the fact that Reynolds-averaged Navier-Stokes (RANS) eddy-viscosity models are predicated on the assumption that mean temperature and velocity gradients are well aligned and that momentum and heat transfer occur almost exclusively in the same (wall-normal) direction. Improved understanding of the flow physics of turbulent heat transfer, and improvement in effective prediction methods for modeling of turbulent heat flux for wall-bounded turbulent

flows, is therefore of value to the engineering community and a potentially fruitful area of CFD research.

Several experimental studies have been performed on turbulent channel flow and have determined that spanwise or circumferential turbulent heat fluxes are often much greater than their wall-normal counterparts in the proximity of the walls [25-27]. However, insufficient accuracy of the data often limits the investigation of the physics of turbulent flow and heat transfer, as well as the effective validation of the predictive performance of turbulence models.

Direct numerical simulations (DNS) of turbulent heat transfer have been performed for periodic turbulent channel flow and have shed light on the physics of flow relating to wall-normal, streamwise, and spanwise turbulent heat transfer [28-35]. Kim and Moin [28] first simulated a channel flow with isothermal walls ($\mathrm{Re}_\tau = 180; \mathrm{Pr} = 0.1, 0.71$ and 2.0) and reported in their DNS study that the high correlation (0.95) between streamwise velocity and temperature fluctuations suggests the possibility of accurately modeling turbulent heat flux using an eddy-viscosity type model [28]. Kasagi et al. [34] and Lyons et al. [35] also reported that streamwise velocity and temperature fluctuations were well correlated. Lu and Hetsroni [30] in their DNS study documented detailed streamwise turbulent heat flux statistics with imposed periodic boundary conditions in streamwise and spanwise directions. A mean temperature gradient was imposed in the streamwise direction at a Reynolds number of 184 based on friction velocity and half channel-height. In contrast to previous DNS studies, there was no restriction to temperature fluctuation near the walls due to non-physical thermal boundary conditions. Kawamura et al. [29] documented the effect of Prandtl and Reynolds number on turbulent heat transfer. In their DNS study it was established that streamwise turbulent heat flux does not vary strongly with Prandtl number in the range 0.2 to 0.71 [29]. For these DNS studies, most documented data were at Prandtl

number of 0.71 and Reynolds number of 180 for both streamwise and wall-normal turbulent heat fluxes. DNS studies that documented spanwise turbulent heat flux statistics were performed by Kawamoto et al. [32] and Matsubara et al. [31] at the same Prandtl and Reynolds number as previous studies investigating wall-normal and streamwise heat flux (0.71 and 180, respectively).

Despite the availability of DNS studies, there is a distinct lack of CFD simulations in the open literature for which RANS and/or hybrid RANS-LES models are evaluated with regard to predicting streamwise and spanwise turbulent heat transfer in wall-bounded flow. It is generally understood that the computational cost of DNS and even large-eddy simulation (LES) is prohibitively high for industrial or engineering level application of CFD, especially at high Reynolds numbers. Therefore, it is appropriate to evaluate and validate more cost-effective turbulence modeling options for the prediction of turbulent heat transfer. The canonical periodic turbulent channel flow test case examined in this study is a simple geometry that can be effectively utilized for that purpose.

While computationally the least expensive turbulence modeling approach, RANS resolves only the mean flow variables while modeling the effect of all scales of fluctuating turbulent motion on the mean flow. This introduces error in the computed solution, most especially in separated flows [11]. In contrast, LES models only the smallest scales while resolving the larger, primary energy containing scales of turbulence. Hence, in general, it theoretically produces more accurate results than RANS for a wide range of flow configurations but is still often considered prohibitively expensive for many industrial applications [12].

The tradeoff of effectively balancing cost versus accuracy has facilitated interest in the development of hybrid RANS-LES (HRL) models. The HRL modeling approach is theoretically more accurate than RANS and more affordable than LES, which potentially creates a competitive

advantage in performance and cost compared to RANS or LES alone [37]. HRL methods can be broadly classified as zonal or non-zonal. For the zonal approach, a RANS model is employed in user specified regions of the computational domain, and an LES model is employed in the remaining regions. The major challenge is the selection of interface conditions to provide seamless transition between the two regions [14,15]. The non-zonal approach, as the name suggests, is one for which the user is not required to specify the RANS and LES regions explicitly, however the Reynolds stress and subgrid stress tensors differ mathematically and bridging the two effectively is still a significant research challenge [15].

This study investigates the performance of the dynamic hybrid RANS-LES model (DHRL) using both the standard formulation previously documented in the literature [13,37,48-49] and a modified formulation with potentially improved blending parameters in the momentum and energy equations. The objective is to evaluate the performance of the DHRL model in comparison to an eddy-viscosity based RANS model and two conventional HRL models, delayed detached eddy simulation (DDES) and improved delayed detached eddy simulation (IDDES), for predicting streamwise and spanwise turbulent heat transfer in a wall-bounded flow. A mean temperature gradient is imposed in the streamwise or spanwise direction, while the mean velocity gradient is non-zero only in the wall-normal direction. The mis-alignment of the mean velocity and temperature gradients introduces significant error into traditional eddy-viscosity RANS models, but is potentially mitigated using a hybrid RANS-LES approach. The overall objective of this paper is to investigate and validate a relatively accurate and cost-effective HRL modeling approach with improved predictive capability for wall-parallel heat transfer in wall-bounded turbulent flow.

3.2. SIMULATION DETAILS

The canonical test case considered here is fully developed turbulent plane channel flow that is statistically homogeneous in the streamwise and spanwise directions. The domain extends $2\pi\delta \times 2\delta \times \pi\delta$ in the streamwise (x), wall-normal (y), and spanwise (z) directions, respectively, where δ is the half-channel height. Boundary conditions are periodic in both streamwise and spanwise directions and a source term analogous to a mean pressure gradient is imposed in the streamwise direction to drive the mean flow. The Reynolds number for all simulations is:

$$Re_\tau = \frac{u_\tau \delta}{\nu} = 180 \tag{1}$$

where u_τ is the friction velocity and ν the kinematic viscosity. The fluid Prandtl number is $Pr = 0.71$.

The test case represents a fully-developed wall-bounded turbulent flow with non-zero mean velocity gradient in the wall-normal direction only, and provides one of the simplest geometries to allow for investigation of the complex flow interaction between a passive scalar field and turbulent velocity field, with temperature being the scalar field in this case. A source term is also included to represent an imposed mean temperature gradient in either the streamwise or spanwise direction, depending on which case is under consideration. Further details of the geometry are discussed in the following subsections. In addition, the mathematical formulation of heat flux relating to specific models considered in this study, representing the two different classes of turbulent modeling approach—RANS and hybrid RANS-LES—are discussed briefly. Details of computational grid, boundary conditions, numerical schemes and flow solver are also presented.

3.2.1. Governing Equations

The relevant equations are the conservation of mass, momentum, and energy for a single-phase, single-species, incompressible fluid with negligible body forces or viscous dissipation. General modeled forms of the equations are obtained by applying an undefined filtering operation, denoted by the hat overbar symbol (^), which is assumed to represent Reynolds averaging for RANS or implicit filtering for LES. The resulting governing equations are:

$$\frac{\partial \hat{u}_j}{\partial x_j} = 0 \tag{2}$$

$$\frac{\partial \hat{u}_i}{\partial t} + \frac{\partial}{\partial x_j}\left(\hat{u}_i \hat{u}_j\right) = -\frac{\partial \hat{p}}{\partial x_i} + \nu \frac{\partial^2 \hat{u}_i}{\partial x_j \partial x_j} + \frac{\partial \tau_{ij}}{\partial x_j} + f_i \tag{3}$$

$$\frac{\partial \hat{T}}{\partial t} + \frac{\partial}{\partial x_j}\left(\hat{u}_j \hat{T}\right) = \kappa \frac{\partial^2 \hat{T}}{\partial x_j \partial x_j} + \frac{\partial q_j}{\partial x_j} + g \tag{4}$$

$$\tau_{ij} = -\left(\widehat{u_i u_j} - \hat{u}_i \hat{u}_j\right) \tag{5}$$

$$q_j = -\left(\widehat{u_j T} - \hat{u}_j \hat{T}\right) \tag{6}$$

In the above, ν is kinematic viscosity and κ is thermal diffusivity. The source terms f_i and g are used to impose appropriate momentum and energy balance, respectively, in the streamwise-periodic domain, and are discussed in more detail in subsection 2.6.

Equations (2-6) are formally valid for both LES and RANS modeling approaches. In practice, the specific modeled form of the equations that is solved during CFD simulation is obtained by substitution of model terms for the (kinematic) turbulent stress tensor, τ_{ij}, and turbulent heat flux vector, q_j. For LES, these terms are obtained using an explicit or implicit subgrid stress model. For RANS, they are obtained using an appropriate Reynolds stress model, for example the eddy-viscosity based SST *k*–ω model.

3.2.2. Shear-Stress Transport (SST) Formulation

A well-known example of the RANS modeling approach is the Shear-Stress Transport (SST *k*-ω) model [40]. It has been widely and successfully used for practical RANS CFD simulation of many complex turbulent flows. Assuming that the filtering operation in Eqs. (5,6) denoted by the hat overbar (^) represents Reynolds-averaging, the turbulent stress tensor and turbulent heat flux vector are modeled using the Boussinesq hypothesis as:

$$\tau_{ij} = \nu_t \left(\frac{\partial \hat{u}_i}{\partial x_j} + \frac{\partial \hat{u}_j}{\partial x_i} \right) - \frac{2}{3} k \delta_{ij} \tag{7}$$

$$q_j = \frac{\nu_t}{Pr_t} \frac{\partial \hat{T}}{\partial x_j} \tag{8}$$

$$\nu_t = \frac{a_1 k}{max(a_1 \omega, F_{sst} S)} \tag{9}$$

where F_{sst} is a blending function, a_1 is a constant, k is turbulent kinetic energy and S represents an invariant measure of the strain-rate magnitude. F_{sst} obtains a value of unity in a boundary layer flow, and a value of zero for free shear layers far from a wall.

Two transport equations, one for the turbulent kinetic energy (k) and the other for the specific turbulence dissipation rate (ω), are incorporated into the SST k-ω modeling framework as follows:

$$\frac{Dk}{Dt} = \tau_{ij}\frac{\partial \hat{u}_i}{\partial x_j} - \beta^*\omega k + \frac{\partial}{\partial x_j}\left[(\nu + \sigma_k \nu_t)\frac{\partial k}{\partial x_j}\right] \quad (10)$$

$$\frac{D\omega}{Dt} = \frac{\gamma}{\nu_t}\tau_{ij}\frac{\partial \hat{u}_i}{\partial x_j} - \beta\omega^2 + \frac{\partial}{\partial x_j}\left[(\nu + \sigma_\omega \nu_t)\frac{\partial \omega}{\partial x_j}\right] + 2(1 - F_1)\sigma_{\omega 2}\frac{1}{\omega}\frac{\partial k}{\partial x_j}\frac{\partial \omega}{\partial x_j} \quad (11)$$

The blending function F_1 plays a similar role as F_{sst}, serving as an indicator function for near-wall and far field regions of the flow. Near the wall, $F_1 = 1$, and a k-ω model form is recovered. Far from the wall, F_1 tends to 0. For further details on the model, readers are referred to Ref. [40]. For the simulations here, the turbulent heat flux was computed using a constant turbulent Prandtl number, $Pr_t = 0.85$.

3.2.3. Monotonically Integrated LES (MILES) Model Formulation

The dynamic hybrid RANS-LES (DHRL) models in this study use monotonically integrated LES [41] (MILES) as the blended LES component. In conventional LES, an explicit subgrid stress (SGS) model is used for closure of Eq. (3) to provide a mechanism by which transfer of

kinetic energy can occur from the resolved to the subgrid (modeled) scales, which manifests primarily as dissipation from the resolved flowfield. In contrast, for the MILES model, τ_{ij} is modeled as equal to zero, and solution of Eq. (3) is accomplished using high-resolution upwind algorithms for the convective terms. This effectively provides an implicit SGS model, in which the numerical dissipation of the convective discretization scheme serves to represent the effect of subfilter scales on the resolved variable fields. Therefore, neither explicit SGS modeling nor successive explicit filtering is required [41]. Numerical dissipation plays a similar role in the energy equation (Eq. 4) to represent subgrid turbulent heat flux.

3.2.4. Detached Eddy Simulation (DES) Model

One example of a non-zonal type of hybrid RANS-LES modeling approach is the Spalart-Allmaras (SA) based detached eddy simulation (DES) model developed by Spalart et al. [12]. Successive model variants include delayed DES (DDES) [38] and improved delayed DES (IDDES) [39]. The latter is one of the more popular methods used for hybrid RANS-LES simulation of high Reynolds number flows with separated shear layers. This model uses the distance closest to a bounding wall as the definition for the length scale, which plays a major role in determining the level of production and destruction of turbulent viscosity. In this approach, the model switches from a RANS mode in the boundary layer to LES mode in the core flow, depending on a criterion based on the turbulence length scale. The eddy viscosity in this model is a function of the Spalart-Allmaras viscosity-like variable, $\tilde{\nu}$, which is computed from a transport equation similar to that for turbulent kinetic energy in the SST k-ω model. The reader is referred

to Refs. [12,38-39] for details on the DES, DDES and IDDES models. For the present study, both the DDES and IDDES model variants will be considered.

3.2.5. Dynamic Hybrid RANS-LES (DHRL) Formulation

The DHRL modeling methodology was originally presented in Refs. [13,36]. DHRL is most appropriately considered as a framework for blending arbitrary RANS and LES model variants into a hybrid RANS-LES model, rather than a specific model in itself. The following sections briefly present the previously documented baseline RANS-LES blending methodology for the DHRL model and discuss the proposed modified blending method.

3.2.5.1. Baseline DHRL Formulation

The DHRL modeling methodology seeks to avoid ambiguity in blending the effects of ensemble-averaged velocity fields (Reynolds stress) and spatially-filtered velocity fields (subgrid stress). This section briefly summarizes only the key aspects. Mean velocity is defined as:

$$\bar{u}_i = \langle \hat{u}_i \rangle \tag{12}$$

The angle brackets in Eq. (12) denote Reynolds averaging. In practice, for stationary flow such as that considered in this study, the Reynolds average is computed during the simulation using a

running time-averaging operation. The baseline blending method for RANS and SGS stresses in DHRL is:

$$\tau_{ij} = \alpha\tau_{ij}^{SGS} + (1-\alpha)\tau_{ij}^{RANS} \tag{13}$$

$$\alpha = \frac{\underbrace{-\left(\overline{u_i u_j} - \overline{u}_i\overline{u}_j\right)\overline{S_{ij}}}_{\substack{Resolved\,TKE\\ Production}}}{\underbrace{\tau_{ij}^{RANS}\overline{S_{ij}}}_{\substack{RANS\,TKE\\ Production}} - \underbrace{\overline{\tau_{ij}^{SGS}}\,\overline{S_{ij}}}_{\substack{SGS\,TKE\\ Production}}} \tag{14}$$

The terms τ_{ij}^{SGS} and τ_{ij}^{RANS} are the subgrid stress predicted by any candidate LES model and the turbulent stress predicted by any candidate RANS model, respectively. The numerator in Eq. (14) represents the production of turbulent kinetic energy (TKE) due to the resolved turbulent scales in the flow. The term in the denominator is the difference of $\tau_{ij}^{RANS}\overline{S_{ij}}$, which is the production of *k* predicted by the RANS model, and $\overline{\tau_{ij}^{SGS}}\,\overline{S_{ij}}$, which is the mean component of the subgrid scale turbulent kinetic energy production (see [13] for further details). Equation (14) indicates that the model operates in a pure LES mode only if the resolved scale production is equal to or greater than the predicted RANS production, otherwise the model behaves in a transitional mode where an additional RANS stress compensates for reduced LES content. In regions with zero LES content, i.e. numerically steady flow, the model operates in a pure RANS mode. For the current model implementation, the RANS part of DHRL is found using the eddy viscosity computed by the k-ω SST model as shown in Eq. (9). As stated above, in the current study MILES is used for the LES model component, hence τ_{ij}^{SGS} is zero and the modeled turbulent stress is simply computed as:

$$\tau_{ij} = (1-\alpha)\tau_{ij}^{RANS} \tag{15}$$

$$\alpha = \frac{-\left(\overline{u_i u_j} - \overline{u}_i \overline{u}_j\right)\overline{S_{ij}}}{\tau_{ij}^{RANS}\overline{S_{ij}}} \tag{16}$$

For flows with heat transfer, the turbulent heat flux vector is similarly expressed as a weighted average of the SGS and RANS model predicted values:

$$q_j = \alpha {q_j}^{SGS} + (1-\alpha){q_j}^{RANS} \tag{17}$$

and when using MILES as the LES component:

$$q_j = (1-\alpha){q_j}^{RANS} \tag{18}$$

Importantly, the RANS turbulent stress and heat flux terms are computed using the mean velocity and temperature fields, i.e. for eddy-viscosity models:

$$\tau_{ij}^{RANS} = \nu_t\left(\frac{\partial \overline{u}_i}{\partial x_j} + \frac{\partial \overline{u}_j}{\partial x_i}\right) - \frac{2}{3}k\delta_{ij} \tag{19}$$

$${q_j}^{RANS} = \frac{\nu_t}{Pr_t}\frac{\partial \overline{T}}{\partial x_j} \tag{20}$$

Similarly, the governing equations for the RANS model (e.g. Eqs. 9-11 in the current DHRL implementation) are solved using the mean, rather than the resolved, velocity field.

Although the baseline DHRL model has been found to successfully improve prediction for a wide range of flows relative to conventional HRL closures, potential weaknesses remain. For example, the blending function, α, is determined based on the statistics of the velocity field only but is used to blend RANS and LES contributions in the modeled form of the turbulent heat flux. This can lead to error for flows in which the mean velocity and temperature gradients are not closely aligned. An extreme example would be isotropic turbulence with an imposed mean temperature gradient, in which case the blending function in Eq. (16) would be undefined. A more practical case is flow in which the mean velocity gradient is non-zero in only one direction (e.g. wall-normal) while the temperature gradient is non-zero in more than one coordinate direction or in a different direction. The former is true for a channel flow case with an imposed streamwise temperature gradient, and the latter is true for an imposed spanwise temperature gradient. In that case it is possible that the blending function will inadequately reproduce an appropriate modeled heat flux. To address this weakness, it is proposed to adopt separate blending parameters for the momentum and energy equations.

3.2.5.2. Modified DHRL Formulation

A separate blending function computed from the statistics of the velocity and scalar (temperature) field instead of the velocity field alone can be used to compute the turbulent heat flux in the modeled energy equation. The turbulent heat flux is decomposed as in Eq. (17), using an equation specific blending variable, α_T:

$$q_j = \alpha_T q_j{}^{SGS} + (1 - \alpha_T) q_j{}^{RANS} \tag{21}$$

The blending function specific to the energy equation is then computed analogous to Eq. (14) as:

$$\alpha_T = \frac{-(\overline{u_j T} - \bar{u}_j \bar{T}) \frac{\partial \bar{T}}{\partial x_j}}{q_j{}^{RANS} \frac{\partial \bar{T}}{\partial x_j} - q_j{}^{SGS} \frac{\partial \bar{T}}{\partial x_j}} \tag{22}$$

The numerator in Eq. (22) represents the production of temperature variance due to interactions of the resolved velocity and temperature fluctuations with the mean temperature gradient. The first term in the denominator represents that production as predicted within a RANS framework, and the second term in the denominator represents the mean production of temperature fluctuations due to the subgrid stress model. For DHRL simulations using MILES as the LES component (as in the present work), the SGS component of the heat flux is assumed zero and the above are equivalently expressed:

$$q_j = (1 - \alpha_T) q_j{}^{RANS} \tag{23}$$

$$\alpha_T = \frac{-(\overline{u_j T} - \bar{u}_j \bar{T}) \frac{\partial \bar{T}}{\partial x_j}}{q_j{}^{RANS} \frac{\partial \bar{T}}{\partial x_j}} \tag{24}$$

It is apparent that Eq. (24) computes a blending function in a similar manner as Eq. (16), but critically, the blending depends on the ratio of resolved-to-modeled mean transport of thermal

energy (turbulent heat flux) in the direction of the mean temperature gradient, rather than resolved-to-modeled transport of mean momentum (turbulent stress) in the direction of mean strain rate. It is therefore believed to be more physically appropriate for blending the RANS and LES heat flux model forms in the energy equation for the DHRL model. Evaluation of this modified version of DHRL is one of the key goals of this study.

3.2.6. Boundary and Forcing Conditions

Dirichlet boundary conditions are used for both velocity and temperature on the channel walls. For velocity, no-slip conditions are applied on the upper and lower wall surfaces. Wall temperature, T_w, is not uniform but varies linearly in the streamwise or spanwise direction. To impose periodicity for the energy equation, the temperature field is expressed in terms of excess temperature, θ:

$$\theta(x, y, z, t) = \hat{T}(x, y, z, t) - T_w(x, z) \tag{25}$$

and the wall temperature boundary condition on upper and lower walls is then simply:

$$\theta_w = 0. \tag{26}$$

For all cases the forcing term in the momentum equation (Eq. 3) is specified to enforce the correct value of Re_τ:

$$f_1 = \frac{u_\tau^2}{\delta} \tag{27}$$

The mean temperature gradient in the streamwise or spanwise direction is imposed using the source term in the energy equation. In general, for an imposed mean temperature gradient $\frac{\partial T_m}{\partial x_i}$, the energy equation is expressed as:

$$\frac{\partial \theta}{\partial t} + u_j \frac{\partial \theta}{\partial x_j} = \kappa \frac{\partial^2 \theta}{\partial x_j \partial x_j} + \frac{\partial q_j}{\partial x_j} - \frac{\partial T_m}{\partial x_j} \hat{u}_j \tag{28}$$

For a flow that is hydrodynamically and thermally fully developed:

$$\frac{\partial T_m}{\partial x_1} = \frac{\langle q_w \rangle}{\rho c_p U_m \delta} \tag{29}$$

Here U_m is the bulk (mixing-cup) streamwise velocity, q_w is wall heat flux, ρ and c_p are density and specific heat, respectively, and the angle brackets denote an ensemble or infinite-time average. For imposed streamwise mean temperature gradient, mean heat flux is therefore computed from bulk velocity as:

$$\langle q_w \rangle = \rho c_p U_m \delta \frac{\partial T_m}{\partial x_1} \tag{30}$$

and the bulk velocity can be obtained from the solution as

$$U_m = \frac{1}{\delta}\int_0^{\delta} \bar{u}_1 \; dy \tag{31}$$

For imposed streamwise mean temperature gradient, dimensionless temperature results are expressed as:

$$\theta^+ = \theta/\theta_f \tag{32}$$

$$\theta_f = \frac{\langle q_w \rangle}{\rho c_p u_\tau} = \frac{\partial T_m}{\partial x_1}\frac{U_m}{u_\tau}\delta \tag{33}$$

Note that this formulation for the energy equation, which is identical to that used in reference DNS studies [5,10], enforces a linear wall temperature variation rather than a uniform heat flux, and wall temperatures do not vary with time. The instantaneous local heat flux, q_w, therefore varies in both space and time, but the mean heat flux $\langle q_w \rangle$ is spatially uniform.

Following Refs. [31,32], for cases with imposed spanwise mean temperature gradient, the mean wall heat flux is zero, and dimensionless temperature results are defined based on the imposed spanwise molecular heat flux, $q_0 = \tilde{k}\frac{\partial T_m}{\partial x_3}$, where $\tilde{k}$ is the molecular thermal conductivity. The reference temperature θ_f is then determined by replacing $\langle q_w \rangle$ in Eq. (33) with spanwise molecular heat flux, q_o:

$$\theta_f = \frac{\partial T_m}{\partial x_3}\frac{\kappa}{u_\tau} \tag{34}$$

where, as in Eq. (28), κ denotes thermal diffusivity.

3.2.7. Computational Grid

Ansys meshing software was used to generate two structured single-block computational grids. A coarse grid of 64^3 cells was first generated and a refined mesh of 128^3 cells was created by refining each cell of the coarse mesh in all three coordinate directions. The two meshes were used to investigate the effect of mesh size on the different modeling methods. The first cell y^+ value was less than 1 for both. Fig. 1 provides a planer view illustration of the computational grids including topology and resolution levels for the coarse and refined cases. Table 1 shows configuration domain size, minimum and maximum cell lengths for each mesh resolution in terms of δ, where δ is the half-channel height.

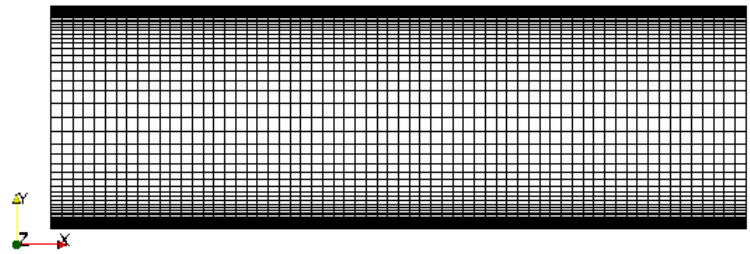

(a) Coarse grid

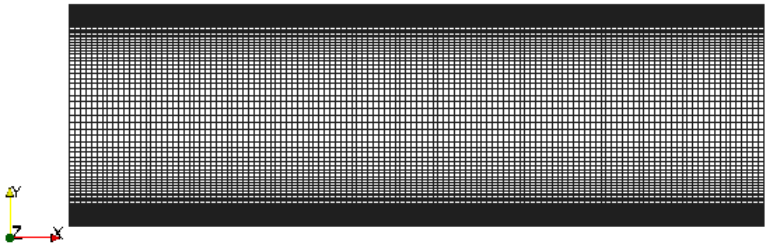

(b) Refined grid

Fig 1. Illustration of computational mesh: (a) coarse grid; (b) refined grid.

Table 1. Domain size and mesh resolution cell lengths ($\Delta x, \Delta y$ and Δz)

	Min. Δy	***Max.*** Δy	Δx	Δz	**Domain size**
Coarse grid	0.0021δ	0.127δ	0.1δ	0.05δ	$L_x \times L_y \times L_z$
Refined grid	0.0005δ	0.0643δ	0.05δ	0.025δ	$6.4\delta \times 2\delta \times 3.2\delta$

3.2.8. Computational Fluid Dynamics Solver

All simulations in this study were performed using the open source CFD code FlowPsi, a finite-volume density-based solver constructed in C++ using the Loci framework. The code utilizes second-order backward difference temporal discretization, second-order implicit flux reconstructions, and least-square gradient computations. This code has been previously investigated and tested for a backward-facing step case and the results were found to be in good agreement with Ansys-FLUENT and Loci-CHEM solvers [36,43]. For the current simulations, incompressible flow was simulated by imposing low Mach number (Ma ≈ 0.1 based on bulk velocity) and small temperature variation. Results confirm that the maximum variation in density throughout the domain was less than 1.8%.

In its baseline version, convective flux terms are discretized by the Harten-Lax-van Leer-Contact (HLLC) Riemann-based scheme introduced by Toro [44]. In this study, the SST k-ω model simulations use the HLLC scheme since only mean flow is resolved and the effect of numerical dissipation error on results is expected to be minimal. For the hybrid RANS-LES cases, a low dissipation optimization-based gradient reconstruction (OGRE) scheme is used for convective discretization in order to resolve small scale fluctuating flow features. The reader is referred to Ref. [45] for further details, in which it is reported that the OGRE scheme provides superior resolution of high wavenumber velocity and pressure modes in unsteady turbulent flow simulations compared to traditional upwind-biased 2nd order schemes.

3.3. RESULTS AND DISCUSSION

3.3.1. Mean and Fluctuating Velocity

The dimensionless mean streamwise velocity profiles ($U = \bar{u}_1$) predicted by each of the models on the coarse and refined grids are shown in Fig. 2. Note that for all results the legend for the modified variant of the DHRL model is represented by DHRL_MOD, while that for baseline variant is DHRL_BAS. Velocity statistics are not affected by the heat transfer condition since temperature in the current simulations acts as a passive scalar. Figure 2 indicates that the log-layer computed by both DDES and IDDES models shows a small mismatch with the DNS data, characteristic of many hybrid RANS-LES models. The disagreement with DDES is smaller than with IDDES, however, the latter shows 1% improvement in result with increased mesh refinement. All models show reasonable but not exact agreement on both coarse and refined grids. The two model variants for DHRL show no differences with regard to the predicted velocity field, as expected. To illustrate the qualitative flow features, Fig. 3 shows the contours of instantaneous and mean velocity for each of the models investigated. It is apparent that all of the hybrid RANS-LES models show resolved turbulent fluctuations qualitatively, as expected, while the SST *k*-w RANS model yields only the mean flow solution.

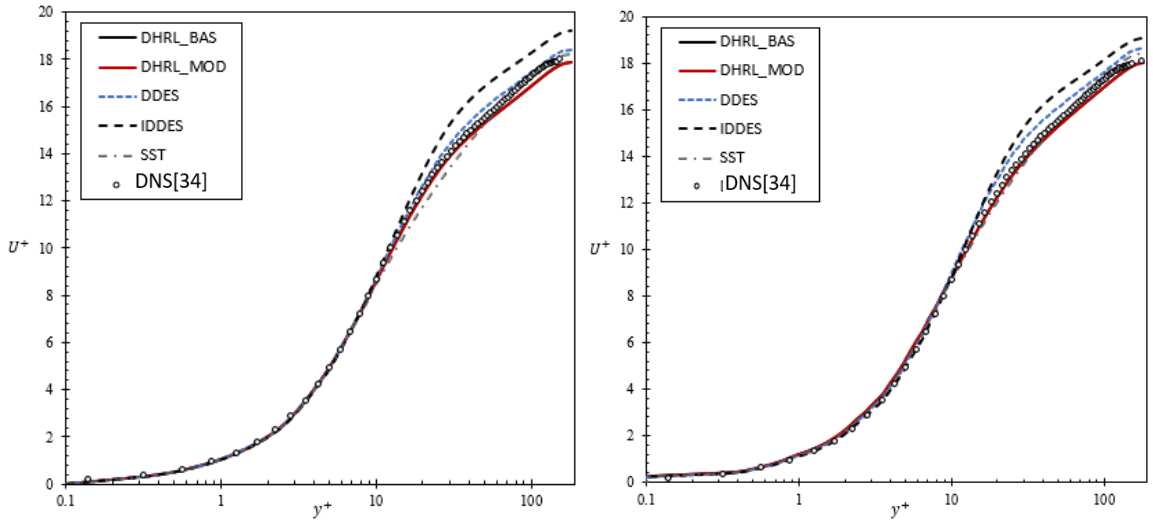

(a) Coarse grid **(b) Refined grid**

Fig 2. Mean velocity profiles on (a) coarse grid, and (b) refined grid for SST, DHRL, DDES, and IDDES models.

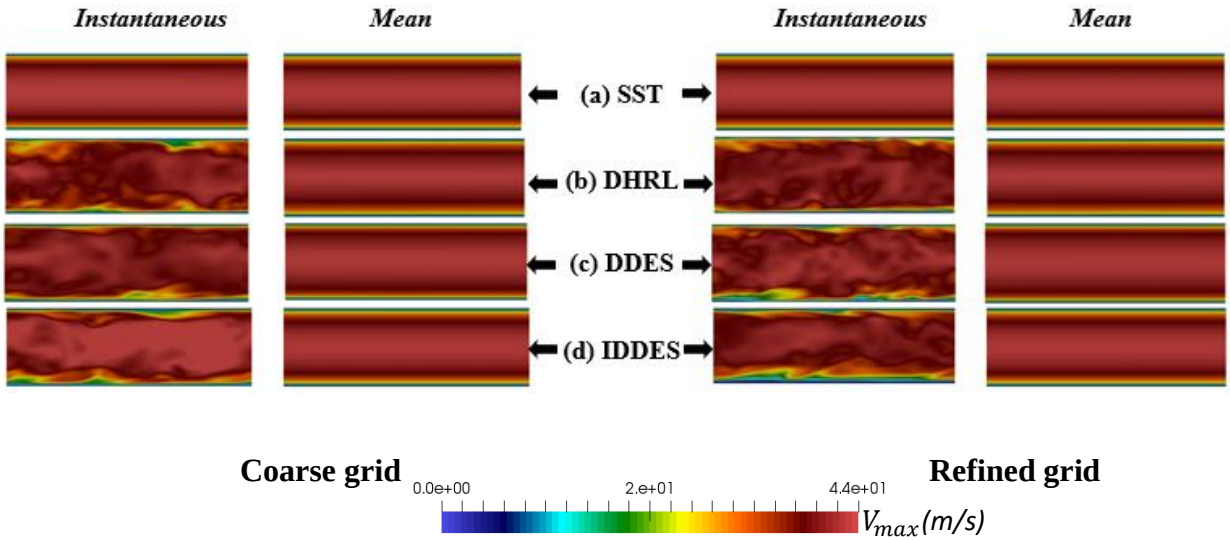

Fig 3. Contours of instantaneous and mean velocity on coarse grid (left), and refined grid (right) for (a) SST, (b) DHRL (c) DDES, and (d) IDDES models

Figure 4 shows profiles of the non-dimensional resolved RMS fluctuating velocity components $u^+_{rms}, v^+_{rms,}$ and w^+_{rms} for the HRL models in comparison with DNS data [29,34]. The RMS velocities are defined as:

$$u_{rms} = \sqrt{\overline{u'_1 u'_1}}\,, v_{rms} = \sqrt{\overline{u'_2 u'_2}}\,, w_{rms} = \sqrt{\overline{u'_3 u'_3}} \tag{35}$$

$$u'_i = \hat{u}_i - \bar{u}_i \tag{36}$$

All models successfully predict the quantitative near-wall behavior, including the peak in streamwise (u_{rms}) fluctuations and the damping of wall-normal (v_{rms}) fluctuations. Only the IDDES model shows a significant quantitative disagreement with DNS for the streamwise fluctuating velocity, overpredicting the peak value by 11.5% and 13.3% on the coarse and fine grids, respectively. Likewise, similar to the mean velocity results above, all models are relatively insensitive to mesh refinement level, showing similar results on coarse and fine grids. For the refined grid, the DHRL model shows an underprediction of u_{rms} at y^+ = 16 of 1.45%, while DDES underpredicts the peak by 5.08%. Furthermore, DDES and IDDES show a consistent overprediction in the range of $18 < y^+ < 140$ on both coarse and refined grids. As shown in Fig. 2, the resolution of the fluctuating velocities is apparently sufficient to accurately reproduce the correct mean velocity profile for the DHRL model and with only a small log-layer mismatch for both DDES and IDDES models.

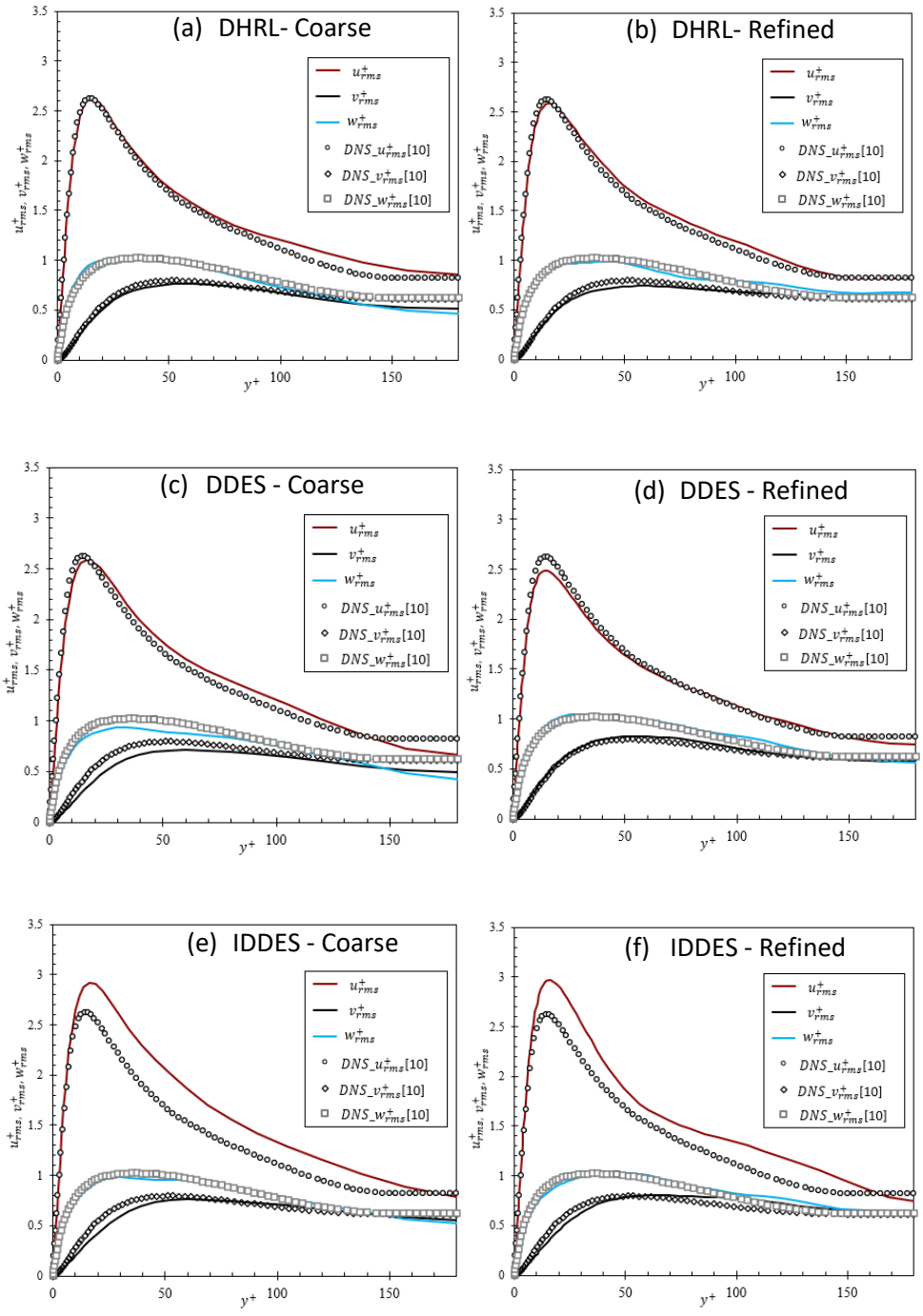

Fig 4. Predicted root mean square (RMS) of fluctuating velocity components in the streamwise (u'), wall-normal (v'), and spanwise (w') directions on coarse and refined grids for the hybrid RANS-LES models used in this study.

Figure 5 shows that the turbulent kinetic energy (TKE) profiles predicted by the DHRL, DDES, and IDDES models are also in quantitative agreement with DNS. Figures 5 (a) and (b) clearly show that results from coarse and refined grids are similar and in good agreement with one another. Quantitatively, at around $y+ = 16$, the DHRL model slightly underpredicts the peak TKE by 2% on the coarse grid, and overpredicts the peak TKE by 5% on the refined grid, and this small difference highlights the relative insensitivity to mesh resolution. DHRL model results are in best agreement with the DNS peak TKE value overall. The SST modeled peak TKE value deviates significantly from DNS; this underprediction of the near-wall peak TKE is a well-known characteristic of that model. Consistent with previous results, DDES is in better agreement with DNS compared to IDDES in the prediction of peak TKE value. On the coarse grid, DDES slightly underpredicts the peak TKE by 2.9%, while IDDES overpredicts the peak value by 10.5%, and these values are relatively consistent on refined grid. Overall, on both grids, DHRL and DDES models show the best qualitative and quantitative agreement with DNS data, while IDDES overpredicts the peak TKE value, and SST modeled peak TKE significantly deviates from DNS.

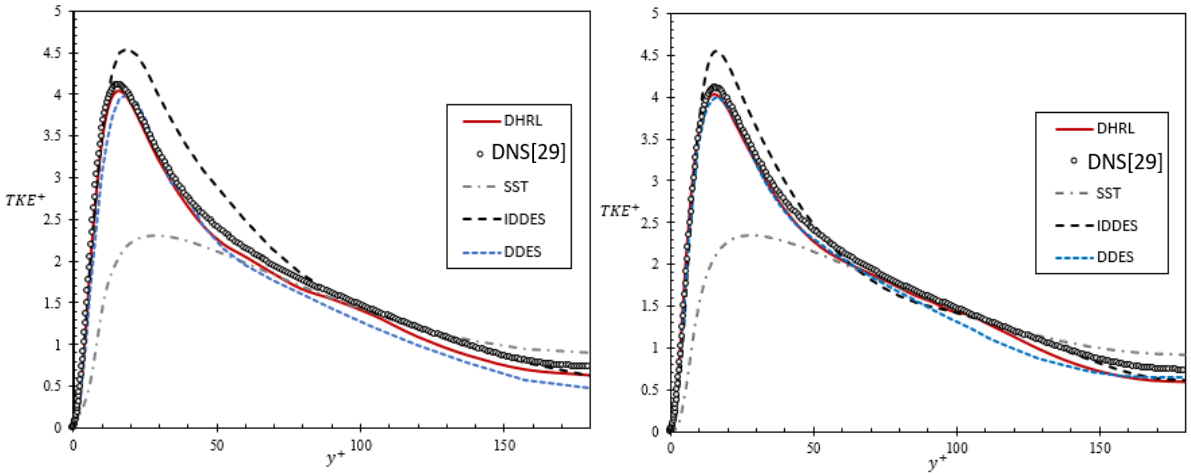

(a) Coarse grid **(b) Refined grid**

Figure 5. Turbulent Kinetic Energy (TKE) profiles of (a)coarse grid, and (b)refined grid across the channel width for SST and hybrid RANS-LES models

Figure 6 illustrates the effect of mesh refinement on predicted mean velocity for each of the models considered. The SST model resolves only the mean flow, therefore it is theoretically possible to obtain a grid independent solution as the mesh refinement level is increased. Figure 6 (a) indicates quantitatively that the solution is nearly grid independent. For the hybrid models, the effect of mesh resolution is less straightforward. In this case, the theoretical exact solution is not the mean (Reynolds-averaged) field, but rather the (implicitly) spatially-filtered variable field. Therefore, as the mesh is refined, the solution itself changes as higher wavenumber portions of the spectrum are resolved, and it is not possible to rigorously define grid independence in the numerical sense. For practical purposes, however, results from different grids can be compared to determine mesh sensitivity, even for LES or hybrid RANS-LES simulations. As seen in Fig. 6,

all of the models show relatively low sensitivity to mesh refinement. This is a fundamental feature of the hybrid RANS-LES models, for which additional RANS stress is included in the transport terms if the LES content of the solution is not sufficient to accurately reproduce the mean flow.

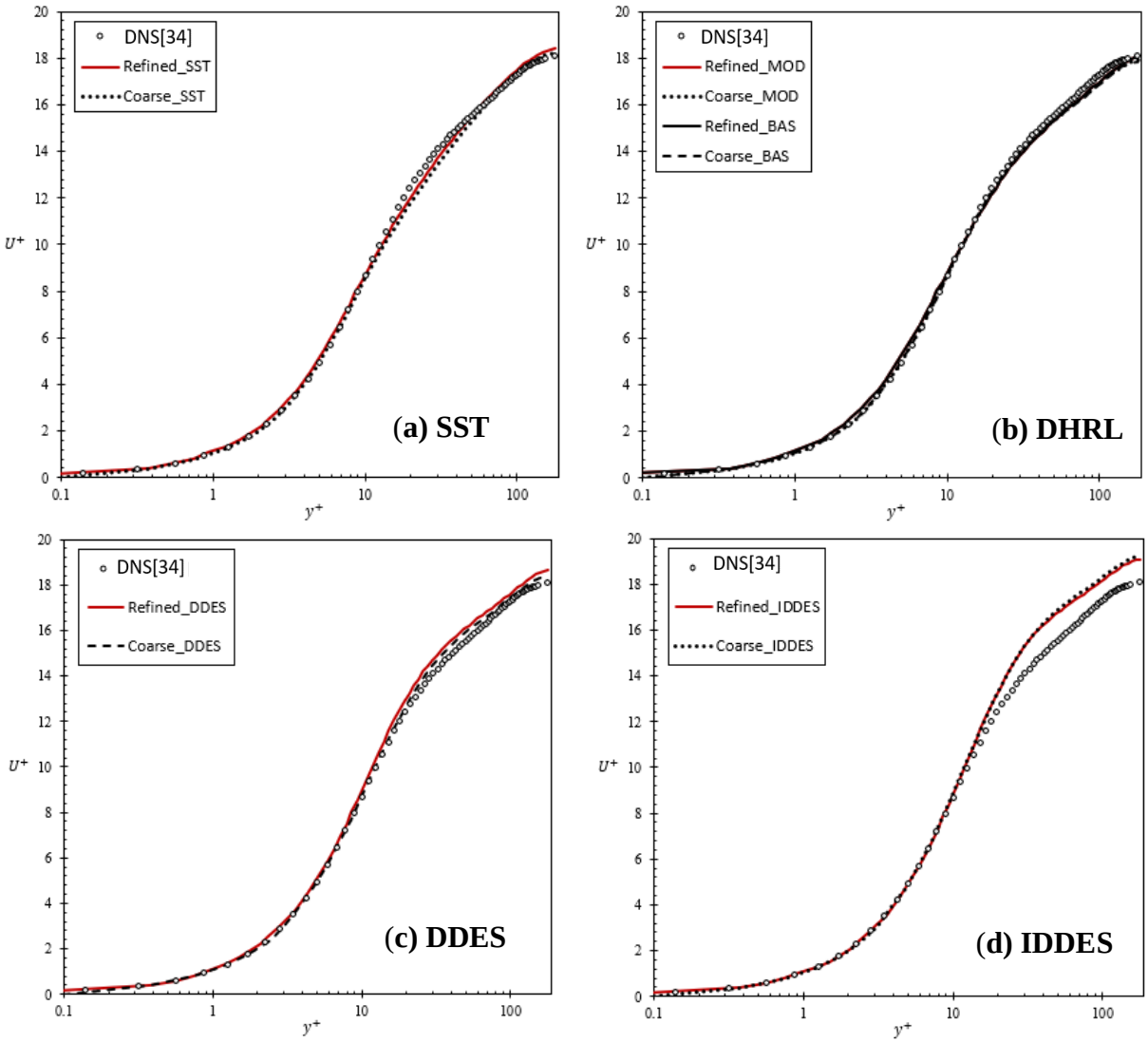

Figure 6. Mean velocity profiles on coarse and refined grids, highlighting mesh sensitivity for (a) SST, (b) DHRL, (c) DDES, and (d) IDDES models

3.3.2. Streamwise Mean Temperature Gradient Test Case

Figure 10 shows the mean temperature profile for the case with imposed streamwise mean temperature gradient. Figure 7 shows the mean temperature profiles obtained for the case with imposed streamwise mean temperature gradient, for each of the models in this study. All five models show quantitative agreement with DNS data [29], and the results closely follow the mean velocity results shown in Fig. 2. It is apparent that the modified variant of the DHRL model (DHRL_MOD) shows the best quantitative agreement with DNS on both coarse and refined grids. In contrast, the IDDES model overpredicts the mean temperature in the log-layer and mid-channel regions on both grids, while DDES, the baseline variant of the DHRL model, and SST show different trends of slight underprediction of mean temperature. Overall, the models are all in quantitative agreement on both coarse and refined grids with DNS data.

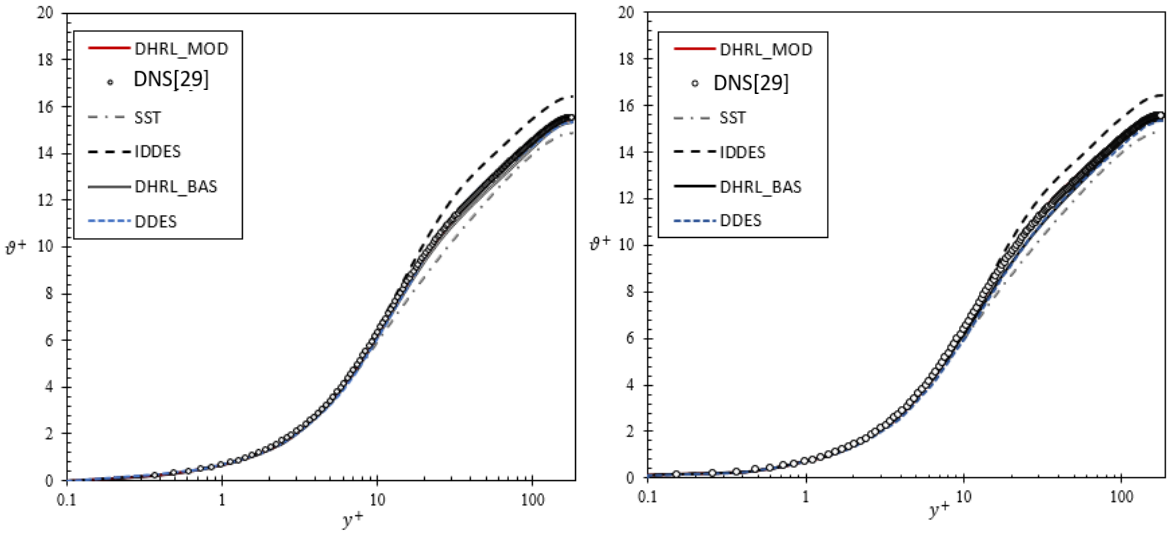

(a) Coarse **(b) Refined**

Figure 7. Mean temperature profiles for SST and hybrid RANS-LES models on (a) coarse grid, and (b) refined grid

Figure 8 provides a qualitative illustration of the instantaneous and mean temperature distribution in the domain. The contours are very similar to the velocity contours presented in Fig. 3. The three hybrid RANS-LES models clearly resolve the unsteady fluctuating temperature field, and the level of resolution is qualitatively similar for all of them.

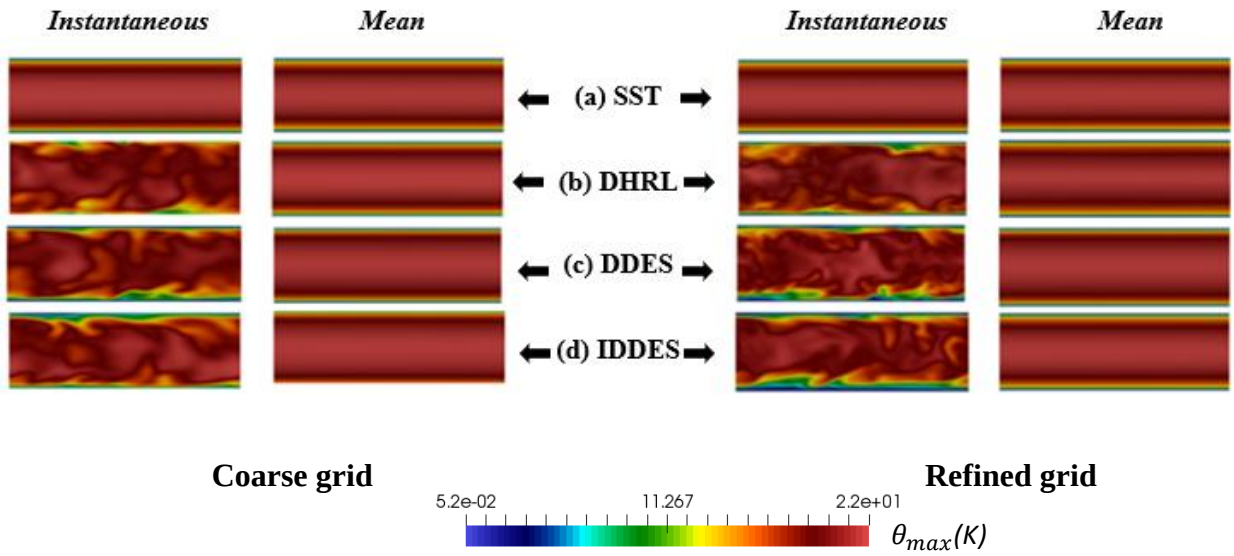

Figure 8. Contours of Instantaneous and mean excess temperature (θ) on coarse grid (left), and refined grid (right) for (a) SST, (b) DHRL, (c) DDES, and (d)IDDES models

Figure 9 shows the fluctuating temperature profile (RMS) for DHRL, DDES, and IDDES models for the imposed streamwise mean temperature gradient test case on coarse and refined grids. The SST model result is not reported due to negligible resolved temperature fluctuations with that model. The root-mean-square temperature fluctuations are compared with the DNS results of Kasagi et al. [34], which is also documented to be in very good agreement with the DNS data at Re_τ = 180 of Kawamura et al. [29]. Interestingly, the fluctuating temperature field shows

little difference for the two variants of the DHRL model and both are in good agreement with the DNS results for most of the channel domain on coarse and refined grids. The predictions of the peak RMS fluctuating temperature value by both model variants at $y+ = 19$ are all slightly below DNS. The DHRL baseline variant (DHRL_BAS) underpredicts the peak value by 5.1%, and the modified variant (DHRL_MOD) underpredicts it by 1.9%. The IDDES model shows a significant overprediction throughout the entire channel domain, and overpredicts the peak RMS fluctuating temperature value by 9.5%, while DDES model underpredicts it by 4.5%. On the refined grid, all models are consistent qualitatively with their predictions on coarse grids, however, differences in results for the modified and baseline variants of DHRL are 0.36%, and 0.64% respectively, while IDDES and DDES differ by 0.04% and 0.31% respectively. The differences in the model results are due to mesh sensitivity of each, but overall differences in results are relatively small and do not produce significant error in the predicted mean velocity as shown in Fig. 2 (b). Most importantly for the present study, the results indicate that the modified variant of DHRL model does in fact show some improvement for the prediction of the fluctuating temperature field over the baseline version on both grids, particularly in the vicinity of the near-wall peak.

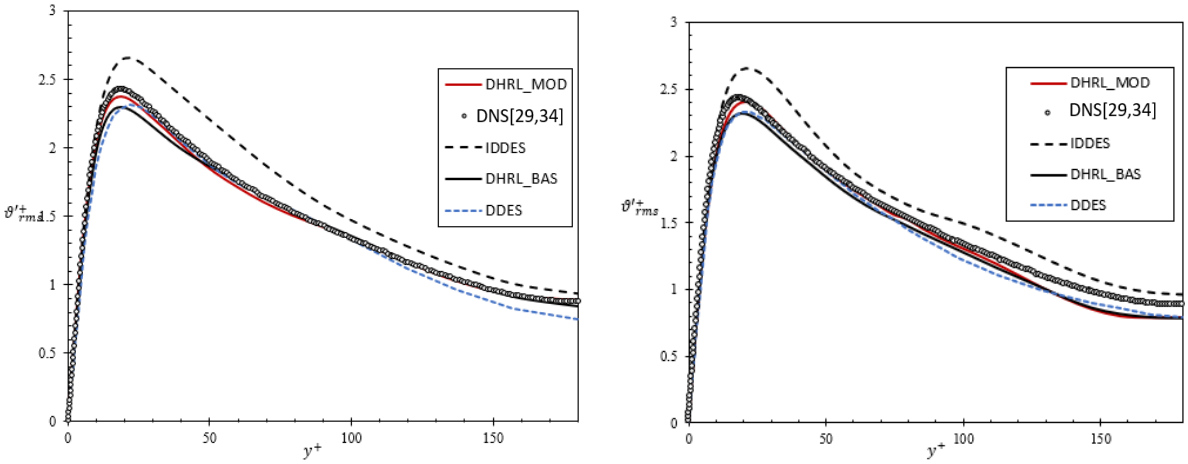

(a) Coarse **(b) Refined**

Figure 9. Root mean square (RMS**) fluctuating temperature profiles on (a)coarse grid, and (b)refined grid with imposed streamwise mean temperature gradient for DHRL, DDES, and IDDES models compared with DNS data of Kawamura et al. [29] and Kasagi et al. [34]**

Figure 10 shows predicted streamwise turbulent heat flux profiles for all models on both coarse and refined grids. The heat flux profiles on the coarse grid shown in Fig.11(a) are consistent and in good agreement with those on the refined grid in Fig. 11(b). In the streamwise direction, the turbulent flow is homogeneous in terms of mean velocity, but the mean temperature gradient is finite and produces a streamwise turbulent heat flux. The SST model prediction differs both quantitatively and qualitatively from the DNS result. This is due to the fact that it relies on a simple isotropic gradient-based diffusion model with a constant turbulent Prandtl number. Since the streamwise mean temperature gradient is uniform throughout the channel, the streamwise heat flux is simply proportional to the turbulent (eddy) viscosity produced by the model, which increases monotonically from the wall to the channel centerline. Consistent with RMS temperature fluctuation, the IDDES model shows an overprediction of turbulent heat flux

throughout the channel when compared with the DNS result. The two DHRL model variants show the best agreement with DNS, though both show an underprediction of the peak value at about $y+ = 16$, which is consistent with the RMS temperature fluctuation shown in Fig. 10. In particular, the modified DHRL model shows qualitative and relatively good quantitative agreement with DNS in the near wall region, including the location and value of the peak turbulent heat flux. Specifically, on coarse and refined grids, the baseline variant of DHRL (DHRL_BAS) underpredicts peak value by about 13%, the modified variant (DHRL_MOD) underpredicts peak value by about 6%. The IDDES model overpredicts the peak streamwise turbulent heat flux by 19% at $y+ = 18$, while the DDES model underpredicts it on both grids by about 9%. Similar to the results shown in Fig. 10, the modified variant of DHRL does show an improvement versus the baseline version in terms of turbulent heat flux, as expected.

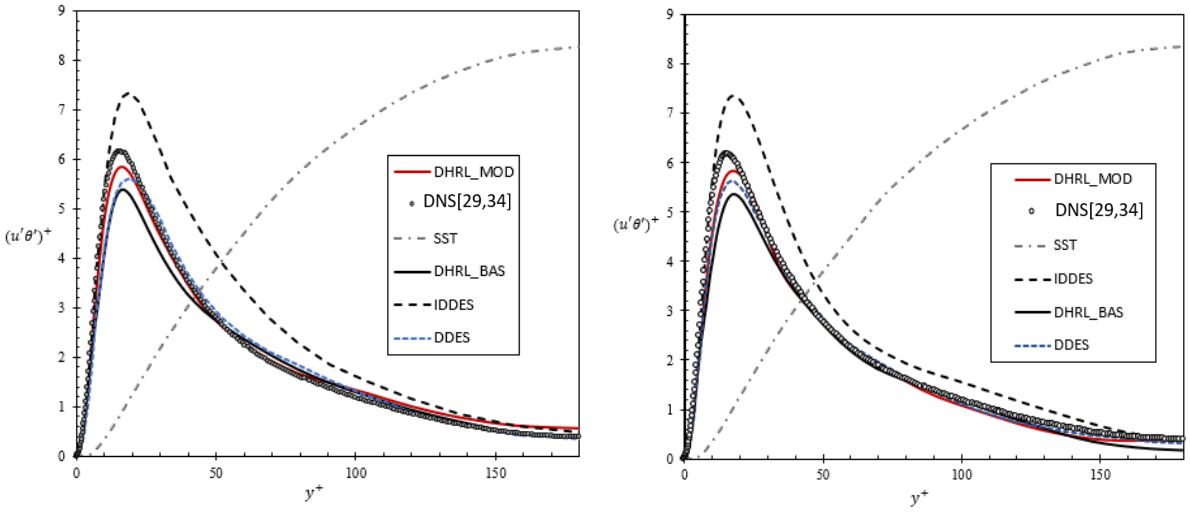

(a) Coarse **(b) Refined**

Figure 10. Streamwise turbulent heat flux profile on (a)coarse grid, and (b)refined grid for SST, DHRL, DDES, and IDDES models

For the streamwise temperature gradient simulations, the non-dimensional heat transfer coefficient is expressed as the Nusselt number (Nu) which is defined as:

$$Nu_{total} = {q_w 2\delta}\Big/{\tilde{k}(T_w - T_m)} = {q_w 2\delta}\Big/{\tilde{k}\theta_m} \tag{37}$$

where δ is the half-channel height, $\tilde{k}$ is the fluid thermal conductivity, and θ_m is the bulk effective temperature. Figure 11 shows that all of the models under predict Nusselt number and highlights non-trivial variation in Nu value between them. Table 2 lists the relative error for each of the models. Both indicate that the SST model is the most accurate, which reflects the fact that RANS eddy-viscosity models are effectively calibrated to accurately reproduce wall fluxes in equilibrium wall bounded flow. The DHRL models agree more closely with DNS than the two DDES variants. Most relevant to the current study, the modified variant of DHRL shows improvement over the baseline version, reducing the relative error by almost half.

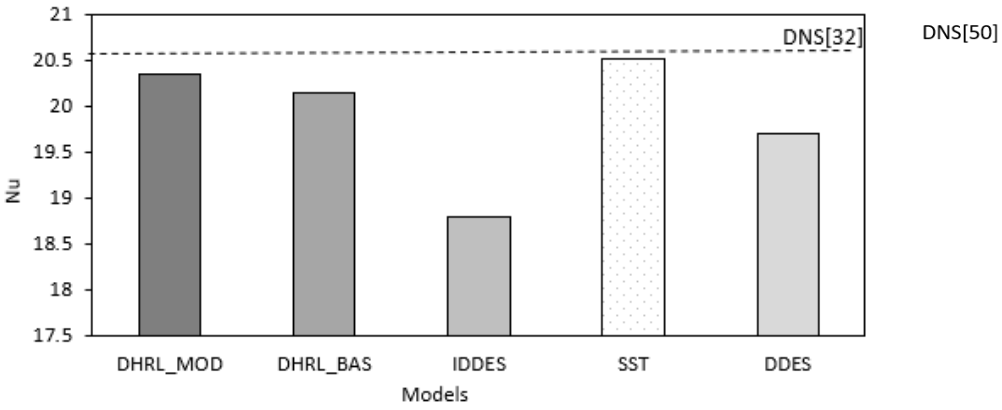

Fig. 11 Predicted Nusselt number compared to DNS data [50]

Table 2. Relative error in predicted Nusselt number for streamwise temperature gradient test case

	DHRL_MOD	DHRL_BAS	DDES	IDDES	SST
Nu Error	-1.2%	-2.2%	-4.4%	-8.8%	-0.4%

3.3.3. Spanwise Mean Temperature Gradient Test Case

For the case with imposed spanwise temperature gradient, both streamwise and wall-normal mean temperature gradient are zero, and mean heat flux occurs only in the spanwise direction. This case is therefore an even more severe test of the ability to accurately resolve turbulent heat transfer using the HRL model. The mean temperature is identically equal to that imposed by the mean spanwise gradient, though the fluctuating temperature and turbulent heat flux varies according to the details of the simulation and turbulence model used.

Figure 12 shows the fluctuating temperature profile for both variants of DHRL and DDES on coarse and refined grids. Results are not shown for the SST model since the fluctuating temperature in the RANS model is negligible. In contrast to the streamwise temperature gradient test case above, θ'_{rms} increases monotoniclly from the wall to the channel centerline with no near-wall peak. This is due to the lack of a steep near-wall mean temperature gradient since heat transfer in the wall-normal direction is zero. The figure shows that all models are in qualitative agreement and loosely follow the DNS profile. Specifically, they are in excellent quantitative agreement with the DNS result within the viscous sublayer region ($y+ < 5$), but starting from the buffer layer ($5 < y+ < 30$) to the center of the channel ($y+ = 180$), the quantitative fluctuating

temperature predictions by the five models vary substantially. However, comparing the coarse and refined grid results as shown in Figs. 12 (a) and (b), the variation is clearly reduced as mesh resolution is increased and the refined grid results tend to be in better overall agreement with DNS data.

Figure 13 shows the spanwise turbulent heat flux profile for all models on coarse and refined grids. Similar to the results for the imposed streamwise mean temperature gradient, the SST model predicts turbulent heat flux with substantial error since the result is based on a simple eddy viscosity model and Reynolds' analogy, which is not appropriate for the conditions in this test case. The figure shows that all the model profiles are in qualitative agreement with DNS, and specifically, in excellent quantitative agreement with DNS result for $y+ < 10$. On the coarse grid, for $y+ > 10$, both variants of the DHRL model and IDDES underpredict spanwise turbulent heat flux, while the DDES model overpredicts it. However, on the refined grid, due to the mesh refinement and sensitivity of each model in the resolution of high wave number modes, for $y+ > 70$ all models underpredict spanwise turbulent heat flux. It is interesting to note that the DDES overprediction of the peak value may be attributed to that model slightly overpredicting RMS of w' by 1.65% as shown in Fig. 4 and overpredicting RMS of fluctuating temperature as shown in Fig. 12. On the refined grid, as shown in Fig. 13 (b), all models underpredict the peak value of spanwise turbulent heat flux. At $y+ = 70$, the modified variant of DHRL underpredicts it by 3.8% compared to 6.3% for baseline DHRL, 0.49% for DDES, and 8.16% for IDDES. The spanwise heat flux decreases towards the centerline due to the decrease in RMS amplitude of both the fluctuating spanwise velocity and the fluctuating temperature. All of the models show this decrease qualitatively, but all are subject to relatively large error relative to the DNS results. The maximum relative error in results comparing both grids is about 12% in the baseline DHRL

model. This is nearly an order of magnitude higher than the maximum relative error for the streamwise temperature gradient test case, which underscores that the spanwise temperature gradient case is a more challenging case to validate the models in the prediction of spanwise turbulent heat flux. This is not surprising, since for the imposed streamwise temperature gradient case there is still significant mean temperature variation in the wall-normal direction (Fig. 7) and the dynamics of the fluctuating temperature field are more similar to the case of simple wall heating. For the case shown in Figs. 12 and 13, the dynamics of the fluctuating temperature field are primarily driven by the imposed spanwise temperature gradient, but even though this is a more challenging test case, the hybrid models all show significant improvement in accuracy compared to the SST model. Furthermore, while neither the baseline nor modified version of DHRL show excellent quantitative accuracy, it is apparent that the modified version yields improve performance, consistent with the case of streamwise mean temperature gradient.

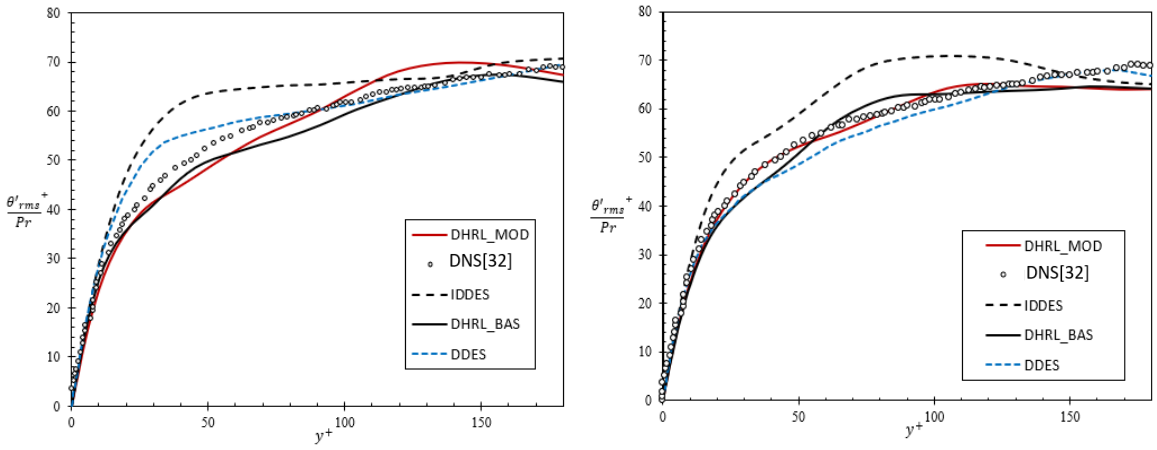

(a) Coarse **(b) Refined**

Fig. 12 Fluctuating temperature profiles on (a)coarse grid, and (b)refined grid with imposed spanwise mean temperature gradient for DHRL, DDES, and IDDES models

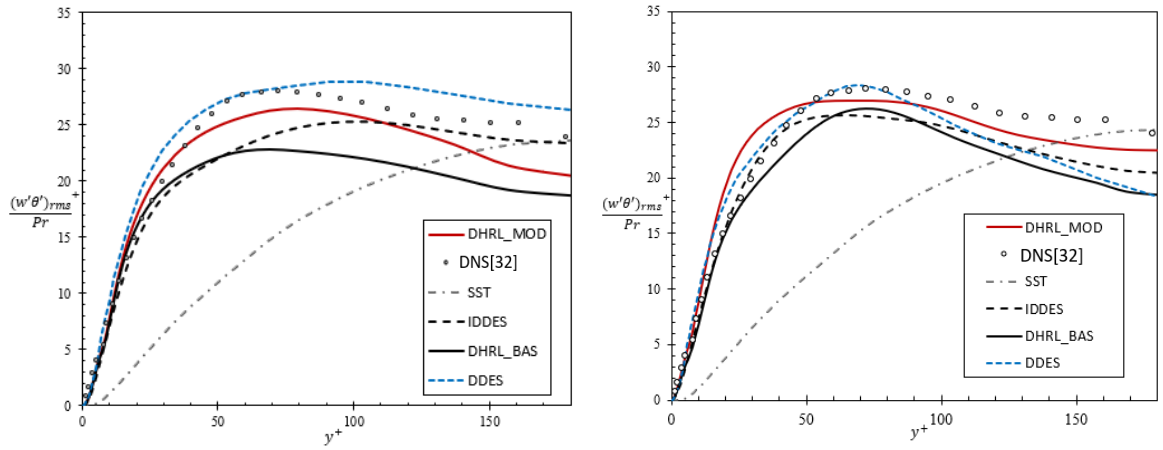

(a) Coarse **(b) Refined**

Fig. 13 Spanwise turbulent heat flux profile on (a)coarse grid, and (b)refined grid for SST, DHRL, DDES, and IDDES models

3.3.4. Summary of Model Performance and Cost

Table 3 summarizes the quantitative model accuracy in terms of the predicted location and value of peak turbulent heat flux for both of the test cases considered, for all models, on the refined grid. As discussed above, while the SST model shows excellent prediction of the wall-normal heat flux, as indicated by Nu, the eddy-viscosity approach cannot accurately reproduce streamwise and spanwise heat transfer characteristics even in a qualitative sense. This should not be interpreted as a weakness of that model, but rather as an illustration of the advantages that can be provided by a hybrid RANS-LES approach. For the hybrid models, the location of peak heat flux was well predicted by all of the models, and the values were predicted within 20% in all cases, indicating both qualitative and quantitative improvement over the RANS model regardless of which hybrid model was used. The new modified variant of DHRL shows improved

performance for both cases over the baseline variant and overall, the best performance among all of the models, with error in peak heat flux less than 5.5% for both cases.

Table 3. Relative error of streamwise and spanwise turbulent heat flux peak-value analysis on refined grid

	Streamwise Temperature Gradient			Streamwise Temperature Gradient		
	Turbulent Heat Flux DNS Peak value - $(u'\theta')+$			Turbulent Heat Flux DNS Peak value - (w'ϑ')+/Pr		
	$y+$ = 16	6.16	100%	$y+$ = 70	27.987	100%
Models	Location ($y+$)	Value	Percent Error (%)	Location ($y+$)	Value	Percent Error (%)
DHRL_MOD	16	5.835	-5.28	70	26.928	-17.19
DHRL_BAS	16	5.368	-12.86	70	26.234	-28.46
MILES	16	5.684	-7.73	70	25.219	-44.94
DDES	17	5.62	-8.77	68	28.389	+6.53
IDDES	17	7.356	+19.42	65	25.702	-37.09
SST	180	8.352	+35.58	180	24.361	-58.86

In order to quantify the computational cost for each of the models, test simulations were performed on one 20 core computational node of the HPC cluster Schooner at the OU Supercomputing Center for Education and Research (OSCER). Reference simulations were performed using a pure MILES approach, i.e. no turbulence model was used. In terms of net CPU time per iteration relative to MILES, the DDES and IDDES models showed an approximately 10% increase, and the DHRL model (both variants) showed an approximately 15% increase. While computational performance is dependent on specific computing architecture, parallelization, compiler, etc., the results here are consistent with CPU time comparisons for previous simulations using hybrid RANS-LES models in the Loci-CHEM code.

3.4. SUMMARY AND CONCLUSION

RANS and hybrid RANS-LES simulations were performed for fully-developed turbulent channel flow at $\mathrm{Re}_\tau = 180$ and $\mathrm{Pr} = 0.71$, with imposed mean temperature gradient in the streamwise or spanwise direction. Quantitative comparison of turbulence statistics, such as the mean and fluctuating velocity, mean and fluctuating temperature, and streamwise and spanwise turbulent heat flux, were compared to DNS results from the open literature to evaluate the performance of several different turbulence models on coarse and refined grids. The models investigated included the k-ω SST RANS model, the DDES and IDDES hybrid RANS-LES model, and two variants of the dynamic hybrid RANS-LES model. A new version of DHRL is proposed in which a separate RANS-to-LES blending function for turbulent heat flux is computed based on the statistics of the fluctuating temperature field. Simulations were performed with the FlowPsi finite-volume CFD solver and utilized low-dissipation numerics to facilitate resolution of the temporally and spatially varying variable fields in turbulent flow.

For the mesh sizes and simulation conditions considered here, coarse and refined grid results are in relatively good agreement with DNS, although refined grids result tend to show better agreement, as expected. The two variants of the DHRL model and the DDES model consistently showed the best agreement with DNS data. In particular, for the case of imposed streamwise mean temperature gradient, the modified variant of DHRL and DDES produced results that agreed quite well with DNS both qualitatively and quantitatively, with less than 9% underprediction of peak heat flux. For the case with imposed spanwise turbulent heat flux, the modified variant of DHRL and the DDES models showed better quantitative and qualitative agreement compared to the baseline version of DHRL and IDDES, respectively. In comparison to streamwise turbulent heat

flux, lower accuracy for all models was observed for the spanwise turbulent heat flux test case. This is likely due to the fact that for this case, the wall-normal mean temperature gradient is zero, and the dynamics of the fluctuating temperature field are quite different than for the case of imposed mean streamwise temperature gradient, which includes wall heating or cooling.

All models except SST predicted the overall trends of the DNS in terms of RMS of fluctuating temperature and turbulent heat flux. Improved sensitivity of the modified variant of DHRL compared to the baseline variant is evident in the prediction of RMS fluctuating temperature profiles for both streamwise and spanwise cases, and this is likely due to the improved model sensitivity to temperature fluctuations used in the blending coefficient for turbulent heat flux. Overall, the modified variant of DHRL, relative to IDDES, DDES and baseline DHRL, showed improved performance in predicting turbulent heat flux both in streamwise and spanwise directions.

For both test cases, the SST RANS model was capable of predicting the mean flow accurately, which is not surprising for this relatively simple wall bounded flow, however it proved unable to even qualitatively reproduce streamwise or spanwise turbulent heat flux due to the incorporation of a simple eddy viscosity diffusion model based on Reynolds' analogy. In this regard the accuracy advantages of a hybrid RANS-LES model compared to a pure RANS model are quite evident. More specifically, the new modified DHRL variant showed improved performance compared with the baseline version, the determination of which was one of the key the objectives of this study. Future work will compare the performance of the two model variants for more complex flows, but based on the results presented here it is recommended that in general

the dynamic hybrid RANS-LES framework be implemented using separate RANS-to-LES blending parameters for the momentum and energy equations.

CHAPTER IV

A NEW STATISTICALLY TARGETED FORCING (STF) FORMULATION: EVALUATION OF A STATISTICALLY TARGETED FORCING METHOD FOR SYNTHETIC TURBULENCE GENERATION IN SCALE-RESOLVING SIMULATIONS

Work from this chapter has been submitted to the ASME Journal of Fluids Engineering (JFE).

4.1 INTRODUCTION

Computational fluid dynamics (CFD) methods for effectively reproducing time-dependent turbulence boundary and/or initial (B/I) conditions have significant potential value for improving simulation of many engineering systems. Because advances in computational resources have made turbulent scale-resolving simulations such as large-eddy simulation (LES) feasible for some industrially relevant flows, accurate and efficient methods for prescribing these complex conditions are increasingly needed.

Research on generation of turbulence B/I conditions has been active over the past two decades, ranging from library-based methods to recycling/rescaling to synthetic turbulence generation (STG) with controlled forcing. These methods become increasingly important when the application of steady state B/I conditions causes development of resolved turbulence fluctuating velocities in the simulation that is either delayed, inaccurate, or nonexistent. It is often not feasible to include the source of turbulent B/I conditions within a simulation. A simple example is simulation of the interaction of an aerodynamic vehicle with a turbulent freestream flow. The source of the freestream turbulence is in fact due to the interaction of the atmospheric boundary layer (ABL) with the ground, but available resources would typically preclude

simulating the ABL flow in addition to the local vehicle aerodynamics. The goal of B/I condition methods such as synthetic turbulence generation (STG) is to replace turbulent content obtained from fully resolved simulations with a reasonable approximation of turbulence for a substantially lower computational cost. In addition, with STG methods turbulent content can be selectively located in specific regions of the computational domain or on the boundaries, providing flexibility such that turbulence B/I conditions are only used in regions where they are needed.

One well known method for prescribing turbulence boundary conditions is recycling/rescaling. For recycled turbulent content, streamwise periodic boundary conditions are imposed on the domain or a portion of the domain such that the turbulent flow leaving the outlet is reintroduced at the inlet. Rescaling of the velocity field can be performed to ensure that the turbulent statistics remain appropriately spatially developing. This method was used, for example, by Spalart et al. [16] to perform large-eddy simulation of a turbulent boundary layer. Lund et al. [17] used the recycling/rescaling method to perform an auxiliary simulation of a turbulent boundary layer, and then extracted planes of time-dependent velocity data to be mapped to the inlet of a simulation with a more complex geometry. Several other studies have extended the recycling/rescaling approach to simulate complex wall bounded flows [18-19]. Schlüter et al. [21] used the recycling/rescaling method to impose fluctuating velocities at the outlet to an LES region of a simulation to impose the statistics obtained from a RANS solution in the downstream region.

A general class of methods that represent an alternative to recycling/rescaling is synthetic turbulence generation (STG). For applications of practical engineering interest on complex geometries, STG methods have the potential to reproduce turbulent fluctuations at desired locations and with desired statistical distributions, without the need to run an auxiliary simulation.

STG methods can be used to specify inflow boundary conditions or as initial conditions for a simulation.

Kraichnan [22] proposed one of the first STG methods for isotropic turbulence, by utilizing a spectral approach to artificially produce an isotropic turbulent velocity field from random Fourier modes. This approach of generating isotropic velocity fields with a specified energy spectrum has been used for example to generate initial conditions for DNS of isotropic turbulence [23,24]. Lee et al. [51] similarly proposed a Fourier transform-based STG method to generate inflow boundary conditions, however one limitation of this method is that it is not applicable to wall-bounded flows due to statistical inhomogeneity in the wall-normal direction.

Using a similar approach for isotropic turbulence, Lundgren [52] defined a forcing term in the momentum equations that is proportional to the fluctuating velocity component. This isotropic linear forcing (ILF) term imitates the natural production mechanism in the turbulent kinetic energy equation. This ILF forcing can be restricted to low wave number modes when using spectral numerical methods. Rosales et al. [53] extended the method in [52] by formulating the forcing term in physical space.

A different algorithmic approach proposed by Jarrin et al. [54,55] is the synthetic eddy method (SEM), which is used to generate realistic synthetic eddies at the inflow of an LES simulation. Results have shown that the synthetic eddy field can evolve to physically realistic turbulent flow after a relatively short distance downstream of the inlet. Some limitations exist in the SEM method such as depletion of the smaller scales of turbulence. This has motivated modification of the SEM to include momentum source terms that energize the velocity fluctuations for some distance downstream.

Keating et al. [56] explain how inappropriate modeling of the scale and structure of synthetic turbulence can lead to a rapid dissipation of velocity fluctuations and an increase in the time/distance required for the flow to recover into a fully turbulent state. Therefore, most recent STG methods attempt to introduce some degree of spatial and temporal coherence through artificial control forcing techniques. Spille-Kohoff and Kaltenbach [57] proposed an inflow STG method based on an added forcing source term in the wall-normal momentum equation. This forcing term enhances the velocity fluctuations in that direction, to match a desired target profile of Reynolds shear stress. This technique enhances the wall-normal fluctuations at discrete locations, with amplitude proportional to the difference between the calculated Reynolds shear stress and a provided target profile. This is an example of an STG method with a controlled forcing feedback loop to achieve a target statistical distribution. They documented that the method reduces the error in the Reynolds shear stress to acceptable values within five channel half heights, although the coefficient of friction and the turbulent kinetic energy required longer downstream distances to reach their fully developed values.

More recently, B. de Laage de Meux et al. [58] proposed a method to impose target statistics of the flow in terms of mean velocity and resolved turbulent stress, using a method denoted anisotropic linear forcing (ALF). The time-dependent forcing function is proportional to the instantaneous velocity via a tensor transformation. The method was found to provide accurate results for isotropic, anisotropic and spatially developing turbulence test cases for LES and hybrid RANS-LES simulations.

The objective of this study is to investigate a newly proposed statistically targeted forcing (STF) method for synthetic turbulence generation. The STF method is a variant of STG with controlled forcing within the simulation domain, implemented via added source terms in the

momentum and energy equations. The method can be viewed to act as a restoring force toward a target statistical state within either a time-averaging or volume-averaging framework. Simulation results are presented for homogeneous isotropic and anisotropic turbulent flow, and results are evaluated in terms of one-point statistics and spectral characteristics.

4.2. STATISTICALLY TARGETED FORCING METHOD

4.2.1. General Description of the Method

Conceptually, the statistically targeted forcing (STF) method proposed here seeks to induce a synthetic turbulence field through the addition of a time-dependent, non-stochastic forcing term in the momentum equation. The forcing term is constructed to drive the instantaneous, local velocity towards a time-dependent target velocity that satisfies the user-specified first- and second-order one-point statistics for the turbulence, i.e., the mean velocity vector and Reynolds stress tensor. To introduce the method, we consider the general form of the continuity, momentum, and energy equations for single-phase, single-species, compressible flow:

$$\frac{\partial \rho}{\partial t} + \frac{\partial}{\partial x_j}\left(\rho u_j\right) = 0 \tag{1}$$

$$\frac{\partial}{\partial t}\left(\rho u_i\right) + \frac{\partial}{\partial x_j}\left(\rho u_i u_j\right) = -\frac{\partial p}{\partial x_i} + \frac{\partial}{\partial x_j}\left(\sigma_{ij}\right) \tag{2}$$

$$\frac{\partial}{\partial t}\left(\rho E\right) + \frac{\partial}{\partial x_j}\left(\rho u_j H\right) = \frac{\partial}{\partial x_j}\left(q_j + u_i \sigma_{ij}\right) \tag{3}$$

In the above, the flow variables ρ, u, p, E, and H may represent local instantaneous (DNS) or filtered (LES) quantities. Likewise, the viscous stress tensor σ_{ij} and heat flux vector q_j include both molecular and, for LES, subfilter contributions. The STF method is implemented by adding a forcing term, f_i, to the momentum and energy equations:

$$\frac{\partial}{\partial t}(\rho u_i) + \frac{\partial}{\partial x_j}\left(\rho u_i u_j\right) = -\frac{\partial p}{\partial x_i} + \frac{\partial}{\partial x_j}(\sigma_{ij}) + f_i \tag{4}$$

$$\frac{\partial}{\partial t}(\rho E) + \frac{\partial}{\partial x_j}\left(\rho u_j H\right) = \frac{\partial}{\partial x_j}\left(q_j + u_i \sigma_{ij}\right) + u_j f_j \tag{5}$$

The source term is constructed such that during each time step of a simulation, the resolved velocity vector is forced toward a target velocity vector that would yield a desired target statistical distribution for the time-varying velocity field. The general form of the forcing term is:

$$f_i = \frac{\rho}{\tau_f}(u_i^* - u_i) \tag{6}$$

Here u_i^* is the target local, instantaneous velocity and τ_f is a characteristic time scale for the forcing term. Inputs to the model include prescription of a local target mean velocity, $\bar{u}_i^*$, and turbulent stress tensor:

$$\overline{u_i' u_j'}^* = \left(\overline{u_i u_j} - \bar{u}_i \bar{u}_j\right)^* \tag{7}$$

where the overbar denotes either Reynolds or Favre (mass-weighted) averaging.

The key aspect of the method is the calculation of the target velocity vector u_i^*. It is first noted that the transformation proposed by Lund et al. [17] can be used to map an ensemble of isotropic velocity fluctuations v' to an ensemble of fluctuations that satisfy a target statistical distribution $T_{ij} = \overline{u_i' u_j'}^*$ as follows:

$$u_i'^* = B_{ij} v_j' \tag{8}$$

$$B_{ij} = \begin{bmatrix} \sqrt{T_{11}} & 0 & 0 \\ T_{21}/B_{11} & \sqrt{T_{22} - B_{21}^2} & 0 \\ T_{31}/B_{11} & (T_{32} - B_{21}B_{31})/B_{22} & \sqrt{T_{33} - B_{31}^2 - B_{32}^2} \end{bmatrix} \tag{9}$$

Similarly, an ensemble of resolved fluctuations satisfying a particular statistical distribution $R_{ij} = \overline{u_i' u_j'}$ can be mapped to an isotropic distribution v' using the inverse of the Lund coefficient matrix:

$$v_i' = A_{ij}^{-1} u_j' \tag{10}$$

$$A_{ij}^{-1} = \begin{bmatrix} 1/A_{11} & 0 & 0 \\ -A_{21}/(A_{11}A_{22}) & 1/A_{22} & 0 \\ (A_{21}A_{32} - A_{31}A_{22})/(A_{11}A_{22}A_{33}) & -A_{32}/(A_{22}A_{33}) & 1/A_{33} \end{bmatrix} \tag{11}$$

$$A_{ij} = \begin{bmatrix} \sqrt{R_{11}} & 0 & 0 \\ R_{21}/A_{11} & \sqrt{R_{22} - A_{21}^2} & 0 \\ R_{31}/A_{11} & (R_{32} - A_{21}A_{31})/A_{22} & \sqrt{R_{33} - A_{31}^2 - A_{32}^2} \end{bmatrix} \tag{12}$$

It is therefore possible to define a mapping from a distribution of resolved velocity fluctuations u_i' with known statistical second moment tensor (turbulent stress) R_{ij} to a distribution $u_i'^*$ with target turbulent stress T_{ij} as:

$$u_i'^* = C_{ij} u_j' \tag{13}$$

$$C_{ij} = B_{ik} A_{kj}^{-1} \tag{14}$$

The instantaneous target velocity used in the forcing function includes the target fluctuating velocity as well as the target mean velocity:

$$u_i^* = \bar{u}_i^* + C_{ij} u_j' \tag{15}$$

where the fluctuating velocity is defined relative to the mean:

$$u_i' = u_i - \bar{u}_i \tag{16}$$

In practice the method is implemented as follows. First a target statistical velocity distribution is specified prior to the simulation in terms of $\bar{u}_i^*$ and $\overline{u_i' u_j'}^*$. As the simulation proceeds, the resolved statistics $\bar{u}_i$ and $\overline{u_i' u_j'}$ are obtained using an appropriate averaging technique. At each time step, the transformation tensor C_{ij} is computed at each point in the domain

based on $\overline{u_i' u_j'}^*$ and $\overline{u_i' u_j'}$. During each iteration, the fluctuating velocity u_i' is computed, and the target instantaneous velocity u_i^* is found using Eq. (15). The forcing term f_i is then computed using Eq. (6) and included as an additional source term in the momentum and energy equations.

4.2.2. Ensemble Averaging

In theory, any appropriate approximation to the Reynolds-averaging operation can be used in the CFD simulations. In the current study, two different methods are implemented and tested for simulation of statistically stationary, homogeneous turbulence. The first is volume averaging, for which the Reynolds-averaged value of any arbitrary variable φ is defined as:

$$\bar{\varphi}(t) = \frac{1}{V} \int \varphi(x_i, t)\, dV \tag{17}$$

and the integral is performed over the entire simulation domain with volume V. The second is time averaging, defined as:

$$\bar{\varphi}(x_i, t) = \frac{1}{t} \int_0^t \varphi(x_i, \tau)\, d\tau \tag{18}$$

where t is the physical simulation time. In practice this is achieved using a discrete running time average, for which the averaged value at each point in the domain can be determined by:

$$\bar{\varphi}(x_i, t) = \frac{n-1}{n} \bar{\varphi}(x_i, t - \Delta t) + \frac{1}{n} \varphi(x_i, t) \tag{19}$$

Here Δt is the time-step size and n is the current number of time steps in the simulation. In the limit $n \to \infty$, the averaged value becomes constant for statistically stationary flow.

4.2.3. Spatial Filtering

Spatial filtering is implemented in the STF method to allow the user to have some measure of control of the turbulent length scale. All simulations adopting spatial filtering in this study were performed using a second-order differential elliptic filter [63]. In this method, for an isotropic filter, the filtered resolved velocity ($\hat{u}_i$) is obtained by solution of Eq. (20), where Δ is the filter width or size:

$$\frac{\partial}{\partial x_j}\left(\Delta^2 \frac{\partial \hat{u}_i}{\partial x_j}\right) = \hat{u}_i - u_i \tag{20}$$

Spatial filtering is implemented in the STF method by first re-defining fluctuating velocity (u_i') in Eq. (16) as filtered fluctuating velocity (u_i''):

$$u_i'' = (u_i - \hat{u}_i) - \left(\bar{u}_i - \bar{\hat{u}}_\iota\right) \tag{21}$$

The instantaneous target velocity used in the forcing function includes the target filtered fluctuating velocity ($C_{ij}u_j''$) as well as the target mean velocity ($\bar{u}_i^*$):

$$u_i^* = \bar{u}_i^* + (\hat{u}_i - \bar{u}_i) + C_{ij}u_j'' \tag{22}$$

At every iteration, the filtered transformation tensor C_{ij} is computed at each point in the domain based on a modified target turbulent stress, T_{ij}, and resolved turbulent stress, R_{ij}, where M_{ij} is a term that represents the contribution to the turbulent stress by the interaction between the filtered and instantaneous velocity:

$$T_{ij} = \overline{u_i' u_j'}^{*} - M_{ij} \tag{23}$$

$$R_{ij} = \overline{\hat{u}_i' \hat{u}_j'} - M_{ij} \tag{24}$$

$$M_{ij} = \frac{1}{2}\left[\left(\overline{\hat{u}_i u_j} + \overline{u_i \hat{u}_j}\right) - \left(\bar{\hat{u}}_i \bar{u}_j + \bar{u}_i \bar{\hat{u}}_j\right)\right] \tag{25}$$

While Eq. (20) represents an isotropic spatial filtering operation, the STF method adopts a generalized anisotropic filter defined by:

$$\frac{\partial}{\partial x_j}\left(\tau_T^2 \, \overline{u_j' u_k'}^{*} \frac{\partial \hat{u}_i}{\partial x_k}\right) = \hat{u}_i - u_i \tag{26}$$

Anisotropic filtering is a relatively simple way to incorporate the fact that turbulence can have different length scales in different directions. The method assumes that regardless of their length scale, large eddies (i.e. velocity fluctuations) will share the same time scale. The tensorial filter width is defined to depend on a characteristic turbulent time scale, τ_T, and the target turbulent stress tensor, $\overline{u_j' u_k'}^{*}$. For homogeneous anisotropic turbulence, spatial variations and turbulent fluctuations are not statistically uniform in all directions and the filtered resolved velocity ($\hat{u}_i$) is

obtained by solution of Eq. (26). For isotropic turbulence, the anisotropic filtering operation is formally similar to the isotropic filter defined in Eq. (20). For this case, spatial variations and turbulent fluctuations are statistically uniform in all directions, hence the anisotropic filter is equivalent to a scalar isotropic filter for which the filter size is defined as:

$$\Delta^2 = \frac{1}{3}\tau_T^2 \left(\overline{u_l' u_l'}^*\right) \tag{27}$$

4.2.4. Prescription of the Forcing Time Scale

The forcing time scale τ_f is arbitrary. In principle, a smaller value will increase the magnitude of the forcing term and drive the velocity more rapidly towards its target value, but too small a value may result in instability or may constrain the flow from developing naturally once resolved turbulence has been introduced. A user can select a relevant time scale based on the known flow physics of the problem under investigation, numerical and stability considerations, and/or trial and error. It would be advantageous, however, to incorporate a universal time scale that takes into account both the physical and numerical aspects of the simulation and simplifies the user input requirements. It is proposed, therefore, that an appropriate time scale is of the form:

$$\tau_f \sim \tau_T \tag{28}$$

where τ_T is the characteristic large-eddy turbulent time scale used in the spatial filter defined by Eq. (26). Depending on the type of simulation performed, the turbulent time scale can be approximated by a characteristic imposed length scale, or from the source of the target statistical

distribution. For example, if a precursor Reynolds-averaged Navier-Stokes simulation is used to specify the target mean velocity and Reynolds stress tensor, the dissipation time scale k/ε can be used to specify τ_T.

For the simulations presented in this paper that use spatial filtering, the form of the forcing term is:

$$f_i = \rho \frac{C_f}{\tau_T}(u_i^* - u_i) \tag{29}$$

Turbulent time scale, τ_T, is specified by the user, and the effect that different values have on the simulation is investigated. The coefficient C_f dictates the overall strength of the forcing term. For cases with spatial filtering, τ_T and C_f must be independently selected. For cases without spatial filtering, it is only the ratio C_f/τ_T that impacts the simulation by controlling the strength of the forcing term by dictating the effective forcing time scale τ_f.

4.3. SIMULATION DETAILS

The majority of the simulations presented here use the Smagorinsky eddy-viscosity based subgrid stress model [61], for which the deviatoric part of the subgrid stress tensor is expressed as:

$$\tau_{ij}^{SGS} = 2\nu_T S_{ij} \tag{30}$$

The eddy viscosity is formulated as:

$$\nu_T = (C_s \Delta)^2 \sqrt{2 S_{ij} S_{ij}} \tag{31}$$

where Δ is the characteristic mesh size, equal to the cube root of cell volume in the current simulations, and the coefficient $C_s = 0.1$.

One test simulation was run using an implicit LES approach similar to MILES [62], for which the subgrid dissipation was assumed to be modeled by the numerical dissipation inherent in the blended upwind portion of the SSF inviscid flux formulation. As shown in the results section, this led to a build-up of energy at high wavenumbers, and as a consequence all of the other simulations used the Smagorinsky model. We note that the implicit LES results could perhaps be improved by increasing the upwind contribution to the inviscid flux.

4.4. TEST CASES

The present study consists of two test cases, isotropic and anisotropic homogeneous turbulence. The STF method is used to produce and sustain time-dependent, stationary flow in the domain. The resulting flowfield is interrogated to evaluate the accuracy of the method for producing realistic turbulent flow conditions with the prescribed first- and second-order one-point statistics. For the anisotropic turbulence test case, unequal normal stress components and a non-zero shear stress component was imposed as the target statistical flowfield. Key issues investigated include:

- Effect of mesh resolution
- Capability of the method to accurately reproduce mean velocity and Reynolds stresses in isotropic and anisotropic turbulent flow domains
- Effect of averaging techniques and critical parameters such as turbulence time scale, τ_T, and forcing coefficient, C_f
- Spectral characteristics of the turbulence generated by the forcing method

The domain for the homogeneous isotropic and anisotropic test cases ("turbulence in a box") is a cube with side length L, with all boundaries periodic. Flow was initialized for all cases to zero velocity and gage pressure. Target Reynolds stress distributions were selected such that the Mach number based on maximum instantaneous velocity was approximately 0.1, which approximates incompressible flow conditions. For the isotropic turbulence cases, the Reynolds number based on the Taylor microscale, λ, and kinematic viscosity, ν, varied from 471 for the finest grid to 1154 for the coarsest grid. Four structured, uniform, Cartesian meshes were used for the simulations, corresponding to 32^3, 64^3, 128^3, and 192^3 cells, and they are illustrated in Fig. 14.

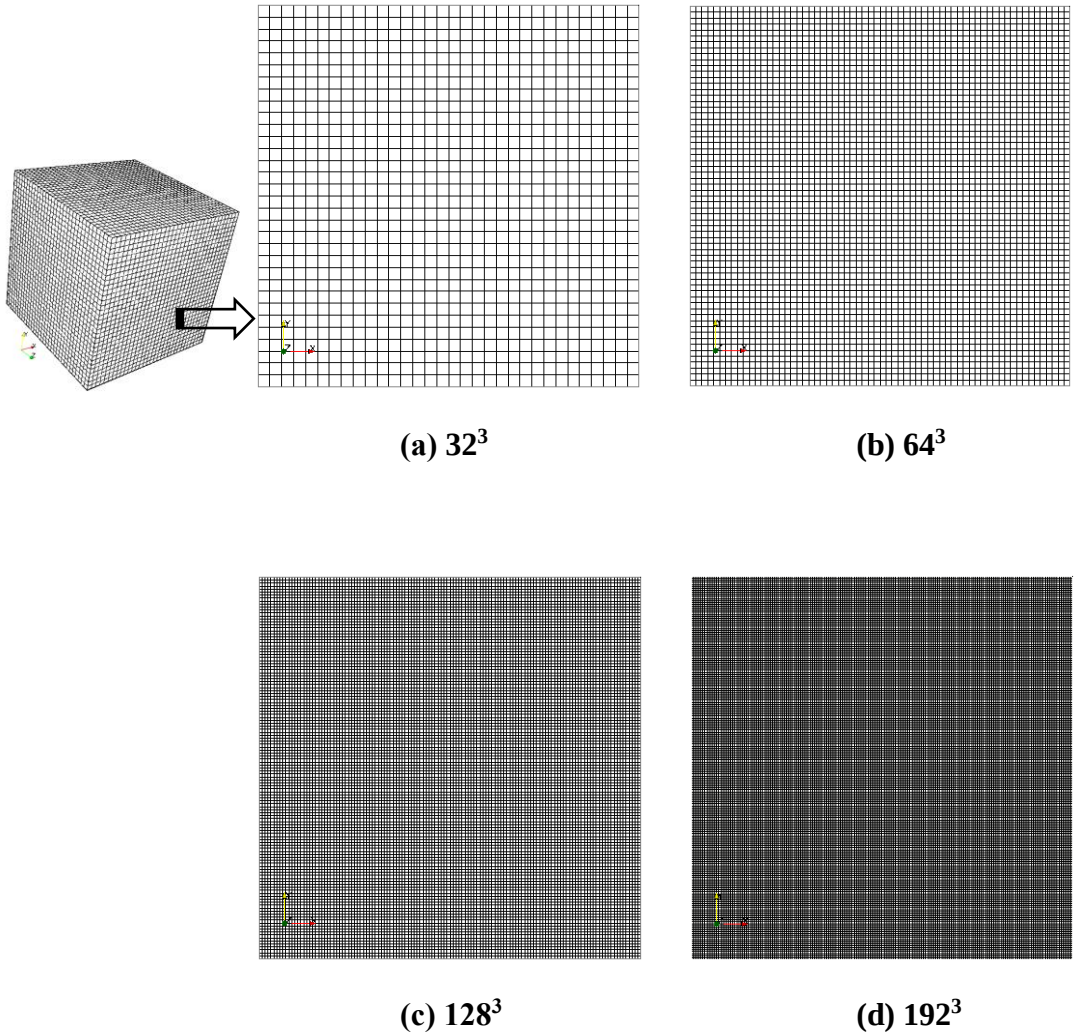

(a) 32^3 **(b) 64^3**

(c) 128^3 **(d) 192^3**

Fig. 14. Planar view of the computational grids for homogeneous turbulence cases showing four mesh resolution levels (a) 32^3, (b) 64^3, (c) 128^3, and (d) 192^3.

4.5. RESULTS AND DISCUSSION

4.5.1. Homogeneous Isotropic Turbulence

Homogeneous turbulence simulations were first performed for an isotropic target field corresponding to:

$$\bar{u}_1^* = \bar{u}_2^* = \bar{u}_3^* = 0 \tag{32}$$

$$\overline{u_1' u_1'}^* = \overline{u_2' u_2'}^* = \overline{u_3' u_3'}^* = v'^2 \tag{33a}$$

$$\overline{u_1' u_2'}^* = \overline{u_1' u_3'}^* = \overline{u_2' u_3'}^* = 0 \tag{33b}$$

The target turbulent kinetic energy is therefore $k^* = \frac{3}{2} v'^2$. The characteristic velocity scale for the target flowfield is v', and a characteristic simulation time scale is defined as:

$$\tau_s = L/v' \tag{34}$$

Initial simulations employing the STF model were run using volume averaging for turbulence statistics, and no spatial filtering. Four different values of the forcing time scale were investigated, corresponding to τ_f/τ_s = 0.45, 0.045, 0.0045, and 0.00033. Forcing was applied during the time interval $0 < t < 3\tau_s$. Simulations were run for an additional interval after forcing was removed

in order to observe the behavior of the velocity field during turbulence decay after being initialized by the STF method.

4.5.1.1. Baseline Results

Initial simulations employing the STF model were run using volume averaging for turbulence statistics, and no spatial filtering. Four different values of the forcing time scale were investigated, corresponding to τ_f/τ_s = 0.45, 0.045, 0.0045, and 0.00033. Forcing was applied during the time interval $0 < t < 3\tau_s$. Simulations were run for an additional interval after forcing was removed in order to observe the behavior of the velocity field during turbulence decay after being initialized by the STF method.

Figure 15 shows contours of velocity magnitude on the periodic bounding surfaces of the domain, corresponding to a simulation time of $t = 2\tau_s$, at which point the fluctuating velocity field had reached an apparently stationary state. The results are shown for a forcing time scale τ_f/τ_s = 0.045. The velocity field exhibits qualitative features of turbulent flow, including a visible range of spatial scales that resemble turbulent eddies. As the mesh resolution is increased from 32^3 to 192^3, the size of the smallest resolved eddies is reduced. The effect of mesh resolution on the overall qualitative flow structure, however, appears to be minimal.

Figure 16 shows contours of velocity magnitude for the 128^3 mesh for simulations using three different values of the forcing time scale. Results are shown on one bounding surface of the domain, at a simulation time of $t = 2\tau_s$. It is apparent that the qualitative flow structure is similar for all three cases. The maximum resolved velocity increases as the forcing time scale is reduced. This is expected since a smaller time scale yields an overall larger forcing term, in effect driving

the local velocity more strongly towards the target velocity vector computed by Eq. (15) at each time step.

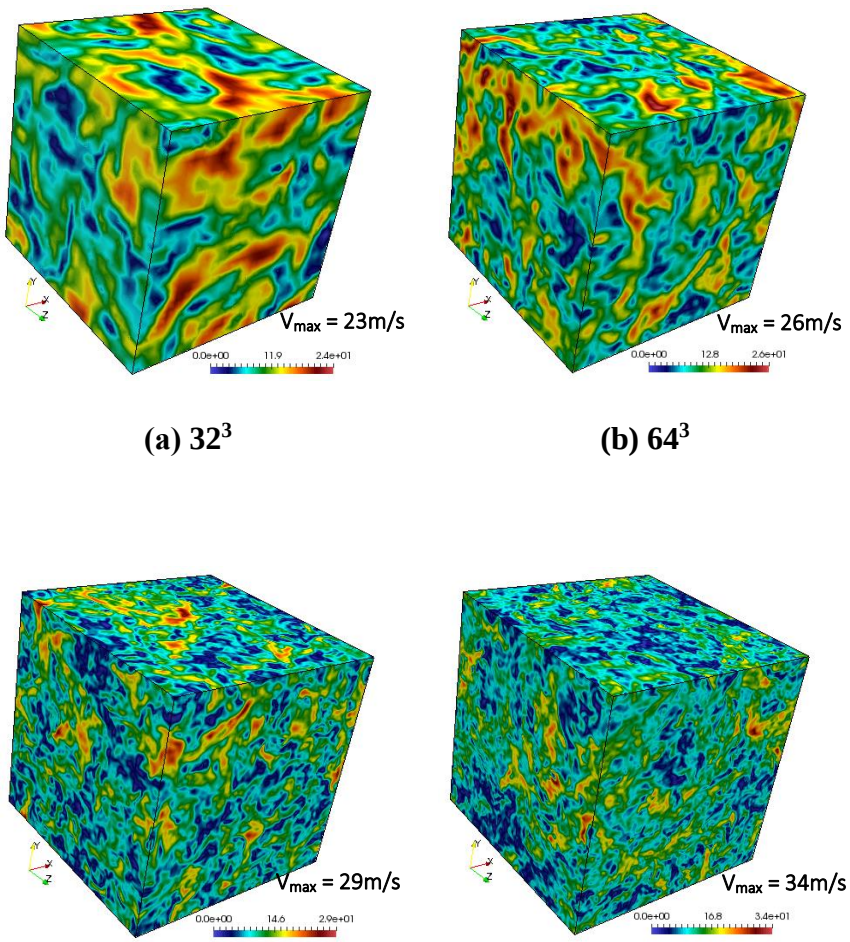

(a) 32^3 **(b) 64^3**

(c) 128^3 **(d) 192^3**

Fig. 15. Contours of instantaneous velocity magnitude for forcing simulation of homogeneous isotropic turbulence with forcing time scale $\tau_f = 0.045$, taken at a simulation time $t = 2\tau_s$. Four mesh resolution levels are shown: (a) 32^3, (b) 64^3, (c) 128^3, and (d) 192^3.

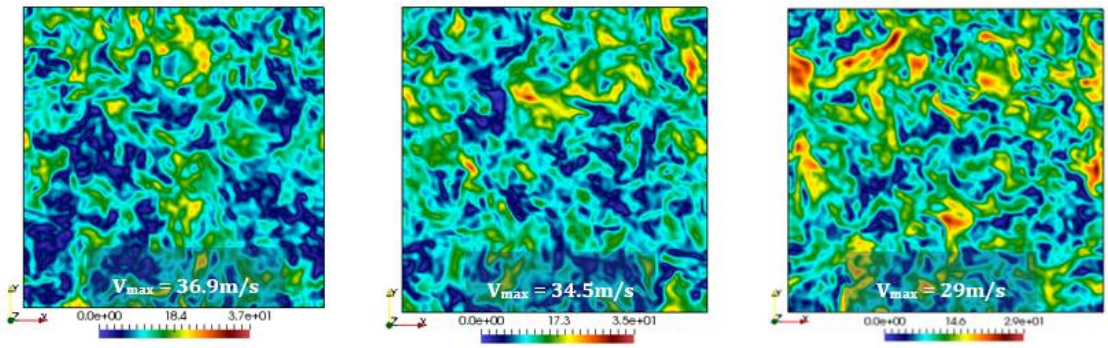

(a) $\tau_f = 0.0045$ **(b) $\tau_f = 0.045$** **(c) $\tau_f = 0.45$**

Fig. 16. Planar view contours of instantaneous velocity magnitude for forcing simulation of homogeneous isotropic turbulence on 128^3 mesh, taken at a simulation time $t = 2\tau_s$. Results are shown for three different values of the forcing time scale.

Figure 17 shows the time history of the ratio of resolved turbulent kinetic energy, $k = \frac{1}{2}\overline{u_i' u_j'}$, to the target value, k^*. Figure 17 (a) compares different mesh resolution levels and Fig. 17 (b) compares different values of the forcing time scale on the 128^3 mesh. The turbulence level can be seen to increase relatively rapidly, and on all grids the ratio levels off at an apparently stationary state near the target value in under one characteristic simulation time, and the time required to reach the stationary state is reduced as the forcing time scale is reduced. The energy level remains nearly constant throughout the time when forcing is applied, and once forcing is removed a power law decay is apparent. The resolved turbulence level during stationary forcing increases towards the target value as the forcing time scale is reduced and the magnitude of the forcing term increases, as expected, and the resolved turbulence level during stationary forcing appears to be insensitive to the mesh resolution level. As seen in Figure 17 (b), the decay rate once forcing is

removed changes as the mesh resolution is increased but appears to be nearly grid independent as the mesh size is increased from 128^3 to 192^3. The decay rate is relatively insensitive to the forcing time scale, which is expected since the forcing term has no direct effect on the flow dynamics after $t = 3\tau_s$.

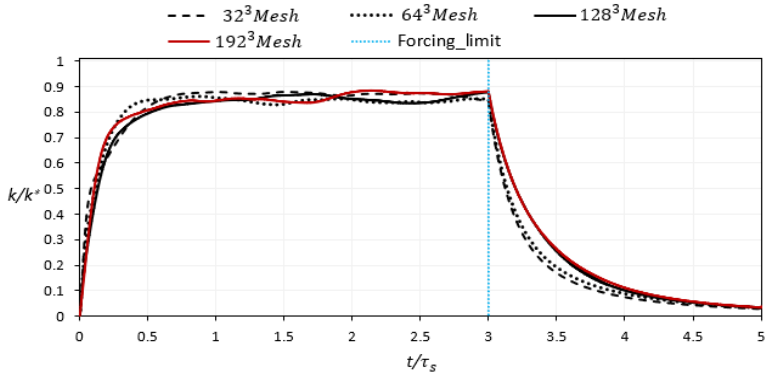

(a) **On four meshes at $\tau_f = 0.45$**

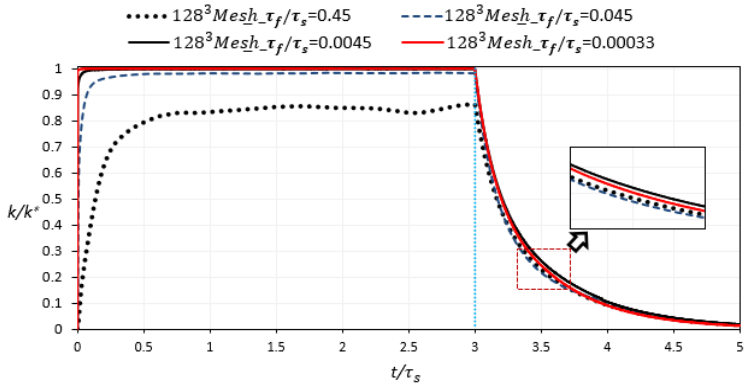

(b) On 128^3 mesh at $\tau_f/\tau_s = 0.45, 0.045, 0.0045,$ and 0.00033

Fig. 17. Time evolution of turbulent kinetic energy (k/k^*) for forcing simulation of homogeneous isotropic turbulence with volume averaging and no spatial filtering: (a) effect of mesh resolution, (b) effect of forcing time scale.

Figure 18. highlights the resolved turbulence level reached in the simulations during the forcing time interval, expressed as the ratio k/k^*, for different mesh resolution levels and forcing time scales. As shown previously, as the level of resolved turbulence is strongly dependent on the forcing time scale. On the 128^3 mesh, the turbulence level ratio increases from 0.85 to 0.999 as the time scale, τ_f, is reduced from 0.45 to 0.00033. The level of resolved turbulence is weakly dependent on the mesh resolution level. For example, for a forcing time scale of $\tau_f = 0.45$, the ratio increases from 0.84 to 0.87 as the mesh is refined from 32^3 to 192^3 cells.

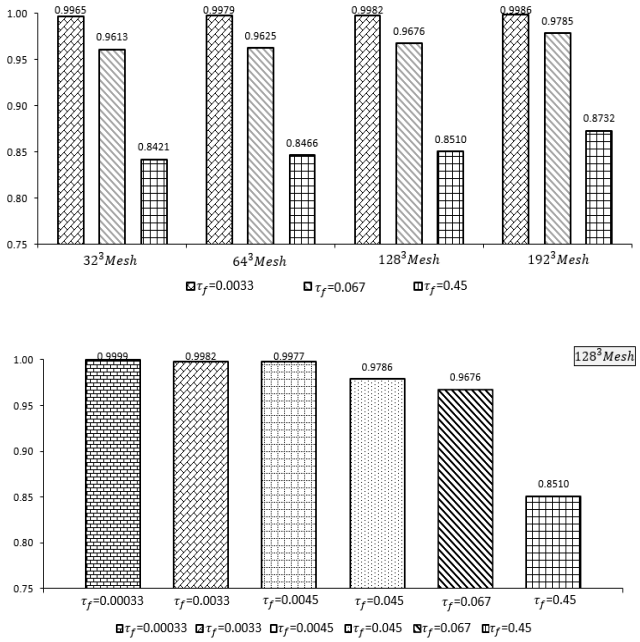

(a) **(b)**

Fig. 18. Ratio of resolved-to-target turbulent kinetic energy, k/k^* for (a) different mesh sizes and (b) on 128^3 mesh at different values of the forcing time scale parameter τ_f.

To understand the spectral characteristics of the turbulence generated by the synthetic forcing method, the fast Fourier transform was applied to the velocity field and integrated over spherical shells in wavenumber (κ) space to obtain the energy density as a function of wavenumber. The results are shown in Fig. 19. Also shown for reference is the Kolmogorov -5/3 scaling for the inertial subrange. In Fig. 19 (b), the energy containing range is indicated as $\kappa \leq EI$, the dissipation range is indicated as $\kappa \geq DI$, and the inertial range is indicated as $EI \leq \kappa \leq DI$. The spectra obtained from all four grids look similar at the lowest wavenumbers while significant difference is apparent at the highest wavenumbers ($\kappa \geq DI$). The two most refined grids (128^3 and 192^3) appear to show an inertial range for which the behavior qualitatively matches the -5/3 law, while the 32^3 and 64^3 grids do not reproduce this behavior. This may explain the decay behavior seen in Fig. 17 (a). Once the synthetic generated turbulence field is sufficiently refined to include an inertial range and proper energy cascade dynamics, the decay rate once forcing is removed is relatively insensitive to further refinement. On all meshes the energy is damped rapidly for wavenumbers larger than 1/N, where N is the number of cells in each of the three coordinate directions.

For the 128^3 grid in Fig. 21(b), energy spectra obtained using different forcing time scales ($\tau_f = 0.45, 0.045, 0.0045$ and 0.00033 are all in good quantitative agreement, with only slight differences evident in the low wavenumbers ($\kappa \leq EI$). Note that the plots are scaled by the maximum value of energy density. Since the total resolved energy increases as forcing time scale is reduced, the unscaled plots would show a vertical shift for different values of τ_f. Overall, the figure shows spectral characteristics indicative of three-dimensional turbulent flow for all values of forcing time scale and for meshes that are sufficiently refined to yield an inertial scaling range.

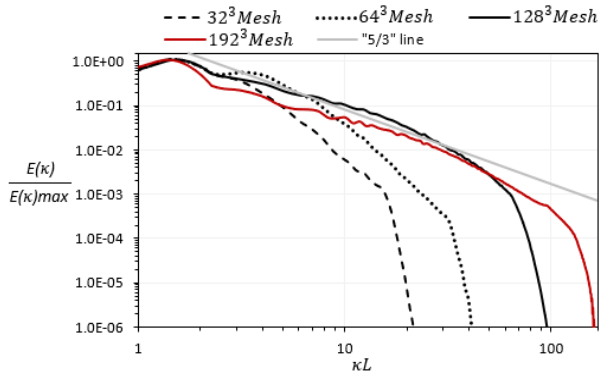

128^3 mesh

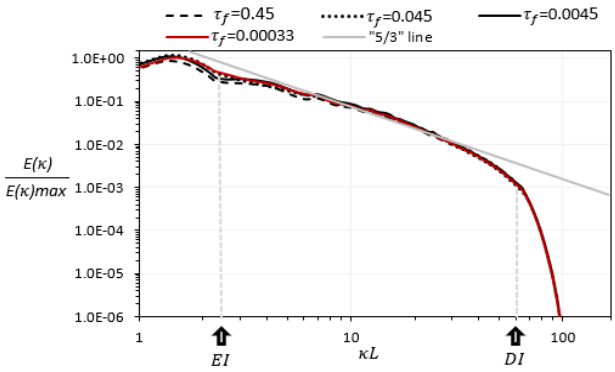

(a) $\tau_f = 0.045$ **(b) $\tau_f = 0.45, 0.045, 0.0045$ and 0.00033**

Fig. 19. Normalized energy density spectrum for forcing simulation of homogeneous isotropic turbulence with volume averaging on (a) different meshes at $C_f = 10, \tau_f = 0.45$, (b) 128^3 mesh, $\tau_f = 0.45, 0.045, 0.0045$ and 0.00033. Similar profiles to that of Fig. 18.

To confirm that the STF method works independently of the specific LES model used, one set of simulations was run using no explicit subgrid stress term, for which the numerical dissipation inherent in the blended upwind inviscid flux term was used to dissipate energy in the small resolved scales. This approach is an informal implementation of the MILES modeling

methodology. Results are shown in Fig. 21 for simulations on the 128^3 grid, using three different values of the forcing time scale. For all three cases, the overall level of turbulent kinetic energy was comparable to the cases using the Smagorinsky SGS model. Again, it is evident that the level of resolved turbulence increases as the forcing time scale is reduced, similar to results with the Smagorinsky model shown in Fig. 20. The spectral behavior was also similar for the low wavenumber portion, displaying a clearly identifiable region with -5/3 inertial scaling. In the higher wavenumber region near the filter cutoff, there is evidence of energy pile up indicating that there is insufficient dissipation to effectively represent the forward scatter of energy to the subfilter velocity scales. It is likely that increasing the upwind contribution to the inviscid flux term would improve the result. The differences between results in Figs. 20 and 21 arise due to the SGS model (or lack thereof) rather than the STF method itself, and the results indicate that the STF method is agnostic to the details of LES model, as expected.

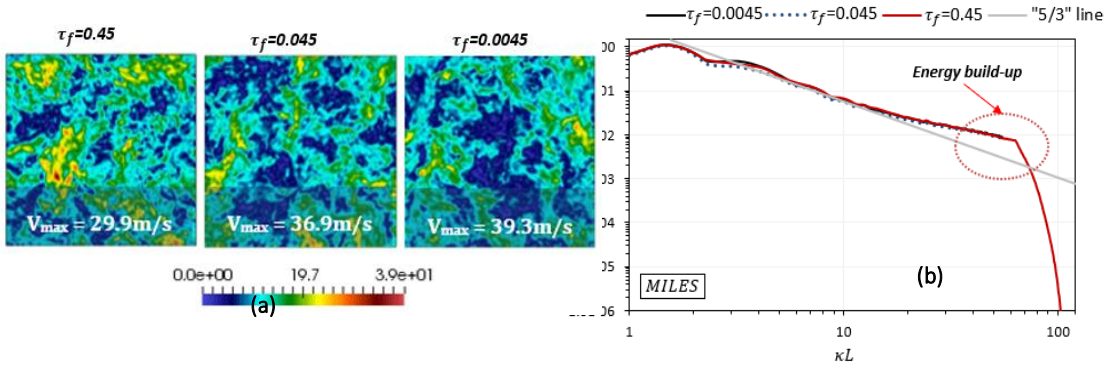

Fig. 20. (a) Contours of instantaneous velocity magnitude and (b) normalized energy spectra for implicit LES simulation with no subgrid stress model, on the 128^3 grid, using three different values of τ_f.

4.5.1.2. Effect of Averaging Technique

Figure 21 compares contours of instantaneous velocity magnitude for equivalent simulations using volume-averaging (VA) versus time-averaging (TA) to compute turbulence statistics on the 128^3 grid at $\tau_f = 4.5$, 0.45, and 0.045. The results show no obvious qualitative differences with regard to the flow structure, and regardless of averaging method used, the maximum velocity magnitude increases as the forcing time scale is decreased. Figure 22 shows the time evolution of turbulent kinetic energy for different values of forcing time scale. Regardless of averaging method, as the value of τ_f is decreased, the resolved turbulence level more quickly approaches the target value, as shown previously. However, cases using volume averaging show a nearly monotonic increase to the final value, while the cases with time averaging show oscillatory behavior, with the magnitude of oscillation increasing as τ_f is decreased. This is effectively a lag in the statistics that are used to compute the forcing term. It is expected that the results will converge to a nearly constant value given a sufficiently long run time, but as shown in the figures the time required to reach this is longer than a single characteristic simulation time, τ_s. Figure 23 compares the energy spectra obtained for three different forcing time scales, using volume and time averaging. The overall shape of the spectra is similar regardless of which averaging method is used. Table 4 compares the quasi-stationary turbulent kinetic energy level achieved for each case. The key point is that consistent with results shown previously, a lower value for the forcing time scale consistently produces more accurate results, regardless of which averaging method is used.

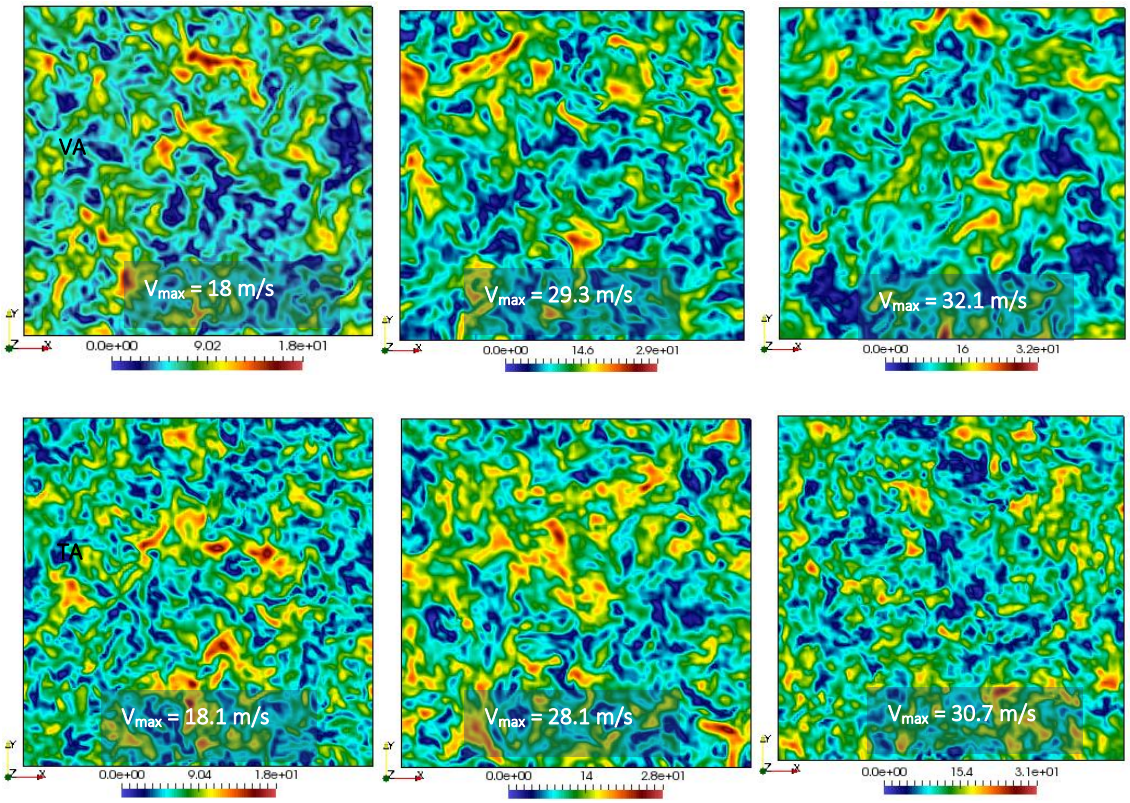

(a) $\tau_f = 4.5$ **(b)** $\tau_f = 0.45$ **(c)** $\tau_f = 0.045$

Fig. 21. Contours of instantaneous velocity magnitude for forcing simulation of homogeneous isotropic turbulence using volume-averaging (VA, above) and time-averaging (TA, below) to compute turbulence statistics on 128^3 grid at $\tau_f = 4.5, 0.45$ and 0.045.

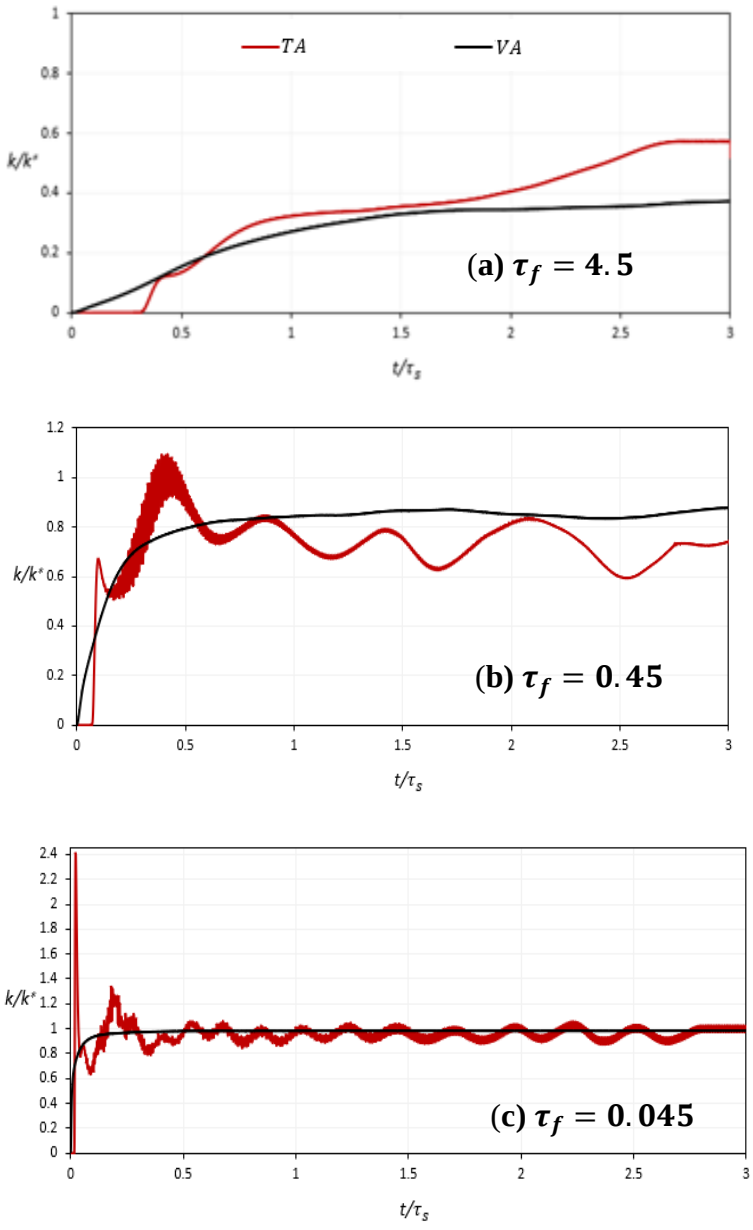

Fig. 22. Time evolution of turbulent kinetic energy, k/k^* for forcing simulation of homogeneous isotropic turbulence using volume-averaging (VA, black) and time-averaging (TA, red) to compute turbulence statistics on 128^3 grid, at $\tau_f = 4.5, 0.45$ and 0.045.

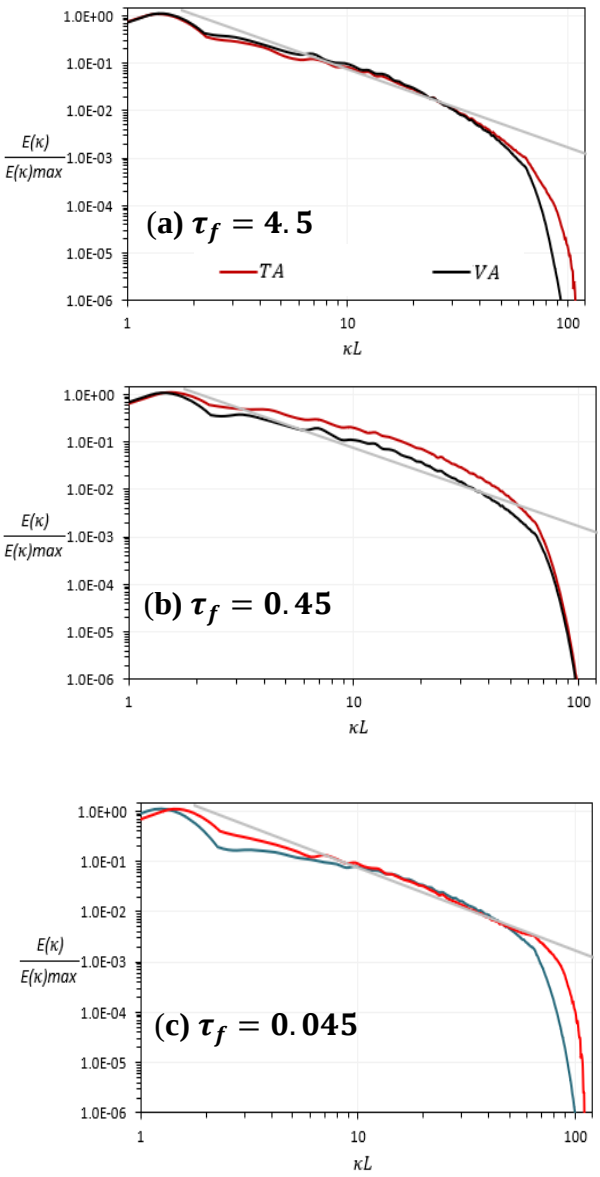

Fig. 23. Normalized energy spectra for forcing simulation of homogeneous isotropic turbulence using volume-averaging (VA, black) and time-averaging (TA, red) to compute turbulence statistics on 128^3 grid, at $\tau_f = 4.5, 0.45$ and 0.045.

Table 4. Percentage ratio of resolved-to-target turbulent kinetic energy for different averaging techniques and forcing time scales at $t = 3\tau_s$

	$\tau_f = 4.5$	$\tau_f = 0.45$	$\tau_f = 0.045$
Time-averaging (TA)	57%	74%	102%
Volume-averaging (VA)	37%	88%	99%

4.5.1.3. Effect of Spatial Filtering

For all of the results shown in the previous sections, no spatial filtering was used in the forcing term and the characteristic large-eddy length scale was effectively imposed by the size of the domain. This is apparent in the previous energy spectra plots, which show peak energy density at a wavenumber slightly less than $2/L$. As discussed in Section 2.3, a spatial filter is applied by specifying a characteristic turbulent time scale and the target Reynolds stress tensor. For the isotropic turbulence simulations, the characteristic (isotropic) spatial filter size, as indicated in Eq. (27), is $\Delta = v'\tau_T$. Several simulations were performed on the 128^3 grid to demonstrate the effect of spatial filtering.

Figure 24 shows contours of instantaneous velocity magnitude comparing a spatially filtered case with the non-spatially filtered case on 128^3 grid, with $\tau_T/\tau_s = 0.45$, and $C_f = 100$. This corresponds to a forcing time scale of $\tau_f = 0.0045$, and for the spatially filtered case corresponds to a filter size $\frac{\Delta}{L} = 0.45$. Volume averaging was used to compute velocity statistics. The figure shows that the maximum instantaneous velocity magnitude is approximately equal for both cases,

but the turbulent length scales are visibly smaller for the spatially filtered case. The corresponding plots of evolution of turbulent kinetic energy are shown in Figure 25. It is apparent that the spatially filtered case reaches a stationary state faster than the non-filtered case, and that the overall level of resolved turbulence is lower. This is due to the fact that the effective turbulence production introduced by the forcing term is balanced in the simulation by the SGS (and to a lesser extent numerical) dissipation, and dissipation is greater when the resolved turbulent structures are smaller. It is also interesting to note that, once forcing is removed, the spatially-filtered case shows more rapid decay of turbulent energy due to the fact that the initialized flowfield obtained from the STF has a smaller integral length scale.

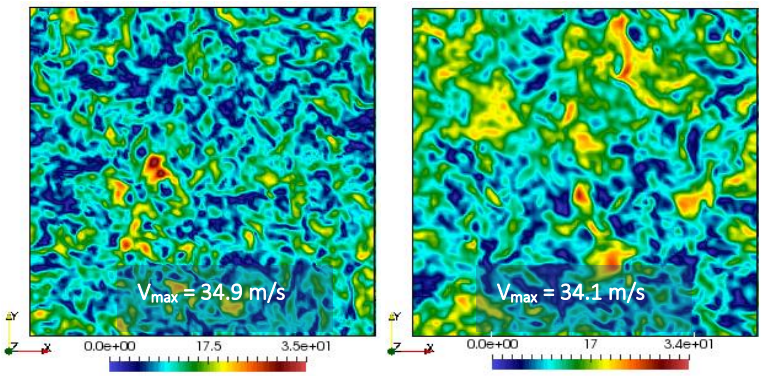

(a) **(b)**

Fig. 24. Contours of instantaneous velocity magnitude for forcing simulation of homogeneous isotropic turbulence, comparing results of (a) spatially filtered with (b) non-spatially filtered simulations, on 128^3 grid, ($\tau_T/\tau_s = 0.45$ and $C_f = 100$).

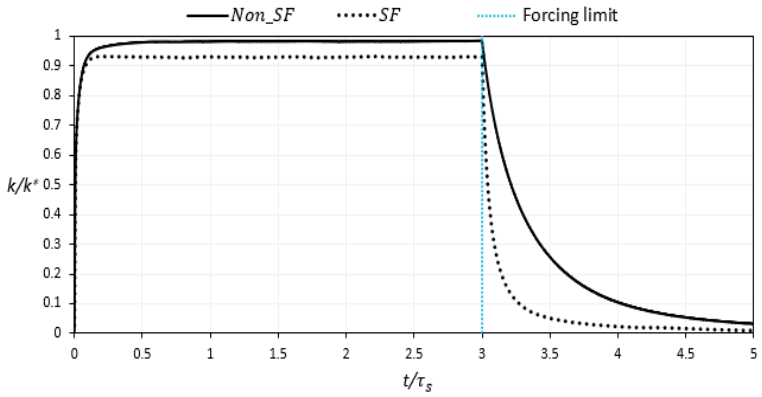

Fig. 25. Time evolution of turbulent kinetic energy, k/k^* for forcing simulation of homogeneous isotropic turbulence, comparing results of spatially filtered (*SF*) with non-spatially filtered (*Non_SF*) simulations, on 128^3 grid ($\tau_T/\tau_s = 0.45$ and $C_f = 100$).

Figure 26 shows the normalized energy spectra for the simulations with and without spatial filtering, for $\tau_T/\tau_s = 0.45$ and $\tau_f = 0.0045$. The effect of spatial filtering is evident, with the maximum energy density occurring at $\kappa \approx 4/L$, which corresponds to $\kappa \approx 1.8/\Delta$. The remainder of the spectrum, including the inertial and dissipation ranges, is qualitatively similar for the two cases.

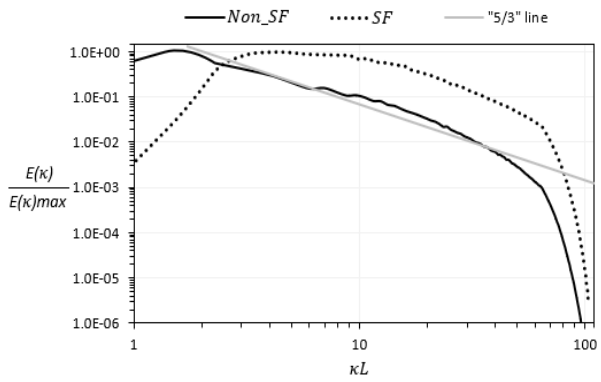

Fig. 26. Normalized energy spectra for forcing simulation of homogeneous isotropic turbulence, comparing results of spatially filtered (*SF*) with non-spatially filtered (*Non_SF*) simulations, on 128^3 grid, using volume-averaging results at $\tau_T/\tau_s = 0.45$ and $C_f = 100$.

To further highlight the effect of spatial filtering, simulations were run using four different values of the characteristic large-eddy timescale (τ_T), and a constant value of the forcing coefficient $C_f = 10$. Figure 27 shows instantaneous velocity magnitude contours for the four different cases. It is apparent that the scale of the visible resolved turbulent flow structures decreases as the filter timescale is reduced, as expected. The temporal evolution of the resolved turbulent energy for the four cases is shown in Fig. 28. It should be noted that, since C_f is held constant, as τ_T is reduced the effective forcing timescale τ_f is correspondingly reduced and the magnitude of the forcing term increases. As a consequence, as τ_T is decreased the simulations more rapidly reach a quasi-stationary state. Interestingly, the level of turbulence reached is apparently insensitive to the imposed time (and length) scale, and the values reached are all approximately equal for a given value of the forcing coefficient C_f. For comparison purposes, the

simulation with $\frac{\tau_T}{\tau_s} = 0.45$ and $C_f = 100$ is also shown. For that case the resulting turbulence level is much closer to the target value. Additionally, once forcing is removed after a simulation time $t/\tau_s = 3$, the turbulent energy decay rate increases (i.e. turbulence decays faster) as τ_T is reduced.

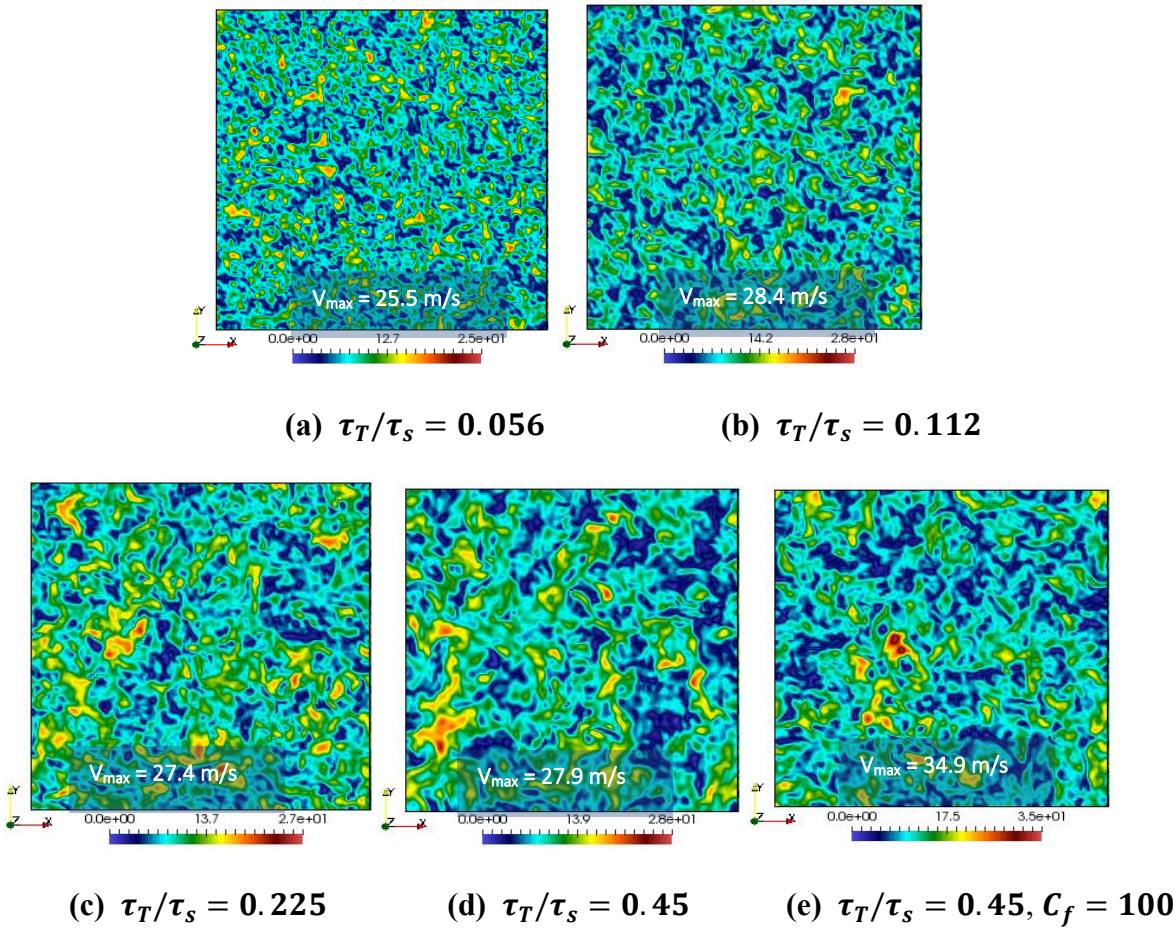

(a) $\tau_T/\tau_s = 0.056$ **(b) $\tau_T/\tau_s = 0.112$**

(c) $\tau_T/\tau_s = 0.225$ **(d) $\tau_T/\tau_s = 0.45$** **(e) $\tau_T/\tau_s = 0.45, C_f = 100$**

Fig. 27. Contours of instantaneous velocity magnitude for forcing simulation of homogeneous isotropic turbulence, with different time-scale targets (τ_T), imposing different turbulent length scales (l_s), on 128^3 grid, using volume-averaging results with $C_f = 10$, and 100.

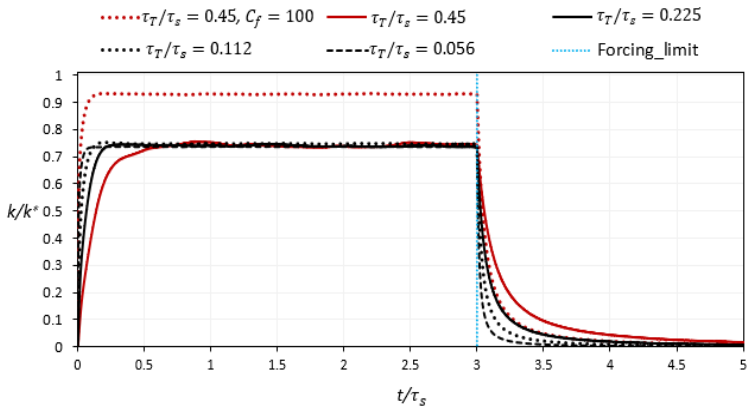

Fig. 28. Time evolution of turbulent kinetic energy, k/k^* for forcing simulation of homogeneous isotropic turbulence, with different time-scale targets (τ_T), imposing different turbulent length scales (l_s), on 128^3 grid, using volume-averaging results with $C_f = 10$, and 100, at $\tau_T/\tau_s = 0.056, 0.112, 0.225$ and 0.45.

Figure 29 (a) shows normalized energy spectra for the cases with varying characteristic large-eddy time scale (τ_T), and a constant value of the forcing coefficient $C_f = 10$. The effect of spatial filtering is apparent, as the peak energy density moves toward higher wavenumbers as τ_T is decreased. The shift in peak wavenumber scales inversely with the effective spatial filter size, Δ, suggesting that filtering is an effective means of controlling the large eddy length scale in the synthetically generated turbulent velocity field. For all cases except that with the smallest value of τ_T, there is an evident inertial range that approximately follows Kolmogorov -5/3 scaling.

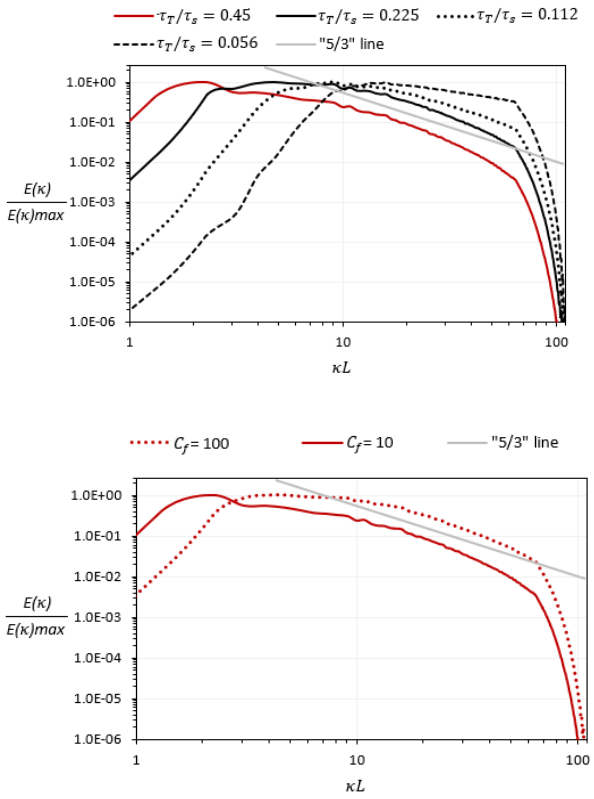

(a) $C_f = 10$, at $\tau_T/\tau_s = 0.056, 0.112, 0.225$ and 0.45 **(b) $C_f = 100$, and $C_f = 10$ at $\tau_T/\tau_s = 0.45$**

Figure 29. Normalized energy spectra for forcing simulation of homogeneous isotropic turbulence, with different time-scale targets (τ_T), imposing different turbulent length scales (l_s) , on 128^3 grid, using volume-averaging results with (a) $C_f = 10$, at $\tau_T/\tau_s = 0.056, 0.112, 0.225$ and 0.45 and (b) $C_f = 100$, and $C_f = 10$ at $\tau_T/\tau_s = 0.45$

Results for isotropic turbulence are summarized in Table 5. For all cases the statistically targeted forcing method reproduces some level of resolved turbulence that approximates an isotropic flow. As seen in the previous results, for sufficiently refined mesh in which sufficient separation exists between the largest resolved length scale and the mesh size, a portion of the

turbulent energy spectrum arises that approximates Kolmogorov inertial scaling. The degree to which the prescribed target Reynolds stress tensor is reproduced depends directly on the magnitude of the forcing time scale, which controls the overall strength of the forcing term. As seen in Table 5, all of the cases that produced at least 90% of the target turbulent kinetic energy had forcing time scale ratios (τ_f/τ_s) less than 0.05. It is worth noting that none of the cases studies exhibited any numerical instability, which indicates that the STF method can be effectively implemented with a judicious choice of forcing time scale that allows both accurate and stable solutions for synthetic turbulence generation.

Table 5. Summary of turbulence statistics for Homogeneous Isotropic STF cases

(Green color implies target and over 90% of target statistics)

					Target Reynolds stress				
					$\overline{u_1^{r}u_1^{r}}^{"}/k^{"}$	$\overline{u_2^{r}u_2^{r}}^{"}/k^{"}$	$\overline{u_3^{r}u_3^{r}}^{"}/k^{"}$		
					0.6666	0.6666	0.6666		
					Resolved Reynolds stress				
Averaging Method	***Spatially Filtered***	τ_T/τ_s	τ_f/τ_s	***Grid***	$\overline{u_1^{r}u_1^{r}}/k^{"}$	$\overline{u_2^{r}u_2^{r}}/k^{*}$	$\overline{u_3^{r}u_3^{r}}/k^{"}$	***Max % Difference***	***(k/k^{*}) ratio%***
Volume	No		0.045	32^3	0.6601	0.6560	0.6665	1.59	99.13
Volume	No		0.45	32^3	0.5725	0.5433	0.5684	18.49	84.21
Volume	No		0.045	64^3	0.6562	0.6522	0.6495	2.56	97.90
Volume	No		0.45	64^3	0.5725	0.5505	0.5701	17.41	84.66
Volume	No		0.045	128^3	0.6567	0.6532	0.6548	2.01	98.23
Volume	No		0.45	128^3	0.5811	0.5433	0.5776	18.49	85.10
Volume	No		4.5	128^3	0.2211	0.2359	0.2151	67.73	33.60
Volume	Yes	0.45	0.045	128^3	0.6211	0.6203	0.6191	7.13	93.03
Volume	Yes	0.45	0.45	128^3	0.4881	0.5009	0.4996	26.78	74.43
Volume	Yes	0.45	4.5	128^3	0.2098	0.2238	0.2041	69.39	31.88
Volume	No		0.45	192^3	0.5778	0.5887	0.5800	13.33	87.32
Volume	No		0.00033	128^3	0.6665	0.6665	0.6665	0.01	99.98
Volume	No		0.0033	128^3	0.6655	0.6658	0.6649	0.26	99.81
Volume	No		0.0045	128^3	0.6651	0.6651	0.6655	0.23	99.78
Volume	No		0.045	128^3	0.6563	0.6515	0.6539	2.27	98.08
Volume	No		0.067	128^3	0.6379	0.6501	0.6456	4.31	96.68
Volume	Yes	0.45	0.45	128^3	0.4881	0.5009	0.4996	26.78	74.43
Volume	Yes	0.225	0.225	128^3	0.4875	0.4947	0.4913	26.87	73.68
Volume	Yes	0.112	0.112	128^3	0.4973	0.4969	0.4985	25.45	74.64
Volume	Yes	0.056	0.056	128^3	0.4912	0.4909	0.4902	26.46	73.62
Time	Yes	0.45	0.045	128^3	0.6128	0.5968	0.5880	11.80	89.88
Time	No		0.045	128^3	0.6544	0.6378	0.6363	4.54	96.42
Time	No		0.45	128^3	0.5464	0.5108	0.4923	26.14	77.47
Time	No		4.5	128^3	0.3467	0.2871	0.3161	56.93	47.50

4.5.2. Homogeneous Anisotropic Turbulence

In principal there is no restriction of the STF method to an isotropic target Reynolds stress. To demonstrate the ability of the method to synthetically generate an arbitrary anisotropic turbulent velocity field, simulations were run on the 128^3 cell grid with τ_f/τ_s = 4.5, 0.45, and 0.045. Results were obtained using volume averaging and no spatial filtering. A first case was run for unequal normal stresses but zero shear stress (denoted ZSS). The target statistics for the ZSS case were prescribed as:

$$\bar{u}_1^* = \bar{u}_2^* = \bar{u}_3^* = 0 \tag{35}$$

$$\overline{u_1'u_1'}^* = 0.5\,k^*,\ \overline{u_2'u_2'}^* = k^*,\ \overline{u_3'u_3'}^* = 1.5\,k^* \tag{36}$$

$$\overline{u_1'u_2'}^* = \overline{u_1'u_3'}^* = \overline{u_2'u_3'}^* = 0 \tag{37}$$

An additional case was run with the same mesh and simulation conditions, but with finite shear stress components (denoted FSS). The target statistics for this case were prescribed as:

$$\bar{u}_1^* = \bar{u}_2^* = \bar{u}_3^* = 0 \tag{38}$$

$$\overline{u_1'u_1'}^* = 0.5\,k^*,\ \overline{u_2'u_2'}^* = k^*,\ \overline{u_3'u_3'}^* = 1.5\,k^* \tag{39}$$

$$\overline{u_1'u_2'}^* = 0.36\,k^*,\ \overline{u_1'u_3'}^* = 0.44\,k^*,\ \overline{u_2'u_3'}^* = 0.62\,k^* \tag{40}$$

Figure 30 shows the contours of instantaneous velocity magnitude for both anisotropic test cases with forcing time scale τ_f/τ_s = 4.5 and 0.45. Similar to the isotropic turbulence results, the maximum velocity magnitude increases with a decrease in the forcing time scale. Likewise, the structure of the velocity field is qualitatively similar to the isotropic results shown in Fig. 16. The time history of the turbulent kinetic energy for the anisotropic case is shown in Fig. 31. The behavior again resembles that of the isotropic test case. It is interesting to note in Fig. 31 (b) that the decay of turbulent kinetic energy differs for the two different anisotropic cases, with more rapid decay occurring for the case with finite shear stress components. Figure 32 shows the energy spectra for the anisotropic cases. Consistent with the other results, the spectra are similar to those for the isotropic test cases, with the peak wavenumber determined by the domain size and the dissipation cutoff wavenumber corresponding to the characteristic mesh size. As for the isotropic cases, a portion of the spectrum is apparent that approximates -5/3 inertial range scaling.

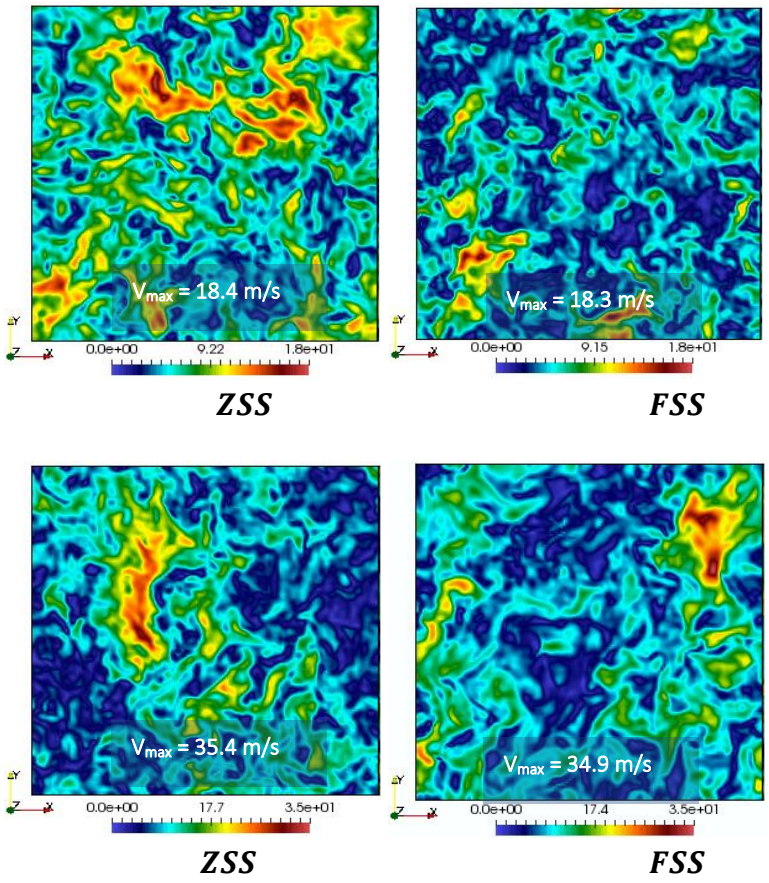

Figure 30. Contours of instantaneous velocity magnitude for forcing simulation of homogeneous anisotropic turbulence with volume averaging, on 128^3 grid, for zero shear stress (ZSS) results (left) with $\tau_f/\tau_s = 4.5$ and 0.45 and imposed finite shear stress (FSS) results (right) with $\tau_f/\tau_s = 4.5$ and 0.45.

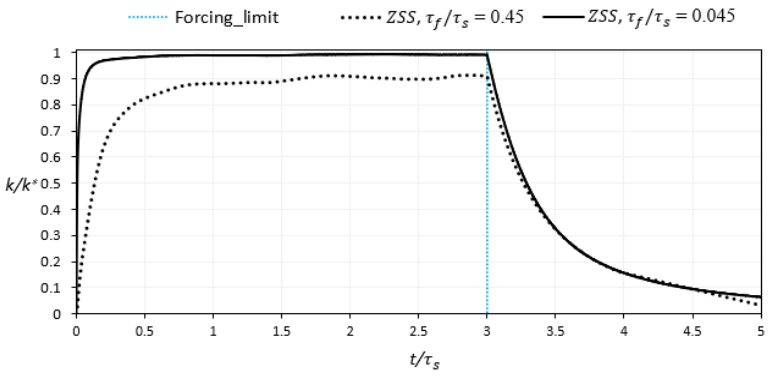

(a) ZSS results, at $\tau_f/\tau_s = 0.45$ and 0.045

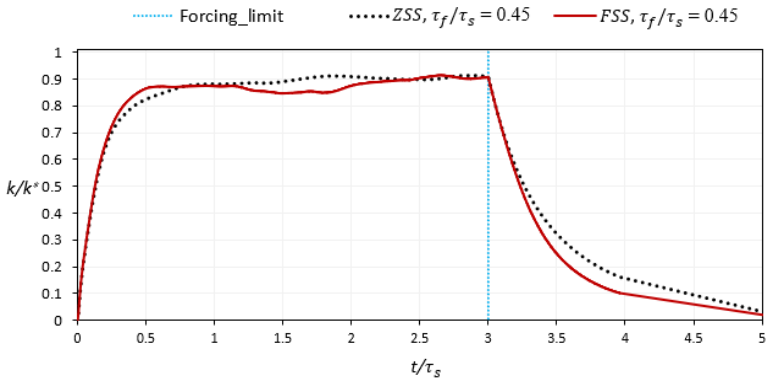

(b) ZSS and FSS results, at $\tau_f/\tau_s = 0.45$

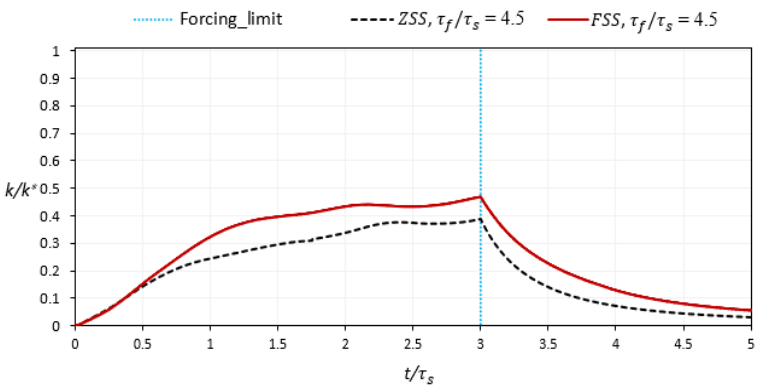

(c) ZSS and FSS results, at $\tau_f/\tau_s = 4.5$

Figure 31. Time evolution of turbulent kinetic energy, k/k^* for forcing simulation homogeneous anisotropic turbulence with volume averaging, on 128^3 grid, (a) zero shear stress (ZSS) results, at $\tau_f/\tau_s = 0.45$ and 0.045 , (b) ZSS and FSS results, at $\tau_f/\tau_s = 0.45$, and (c) ZSS and FSS results, at $\tau_f/\tau_s = 4.5$.

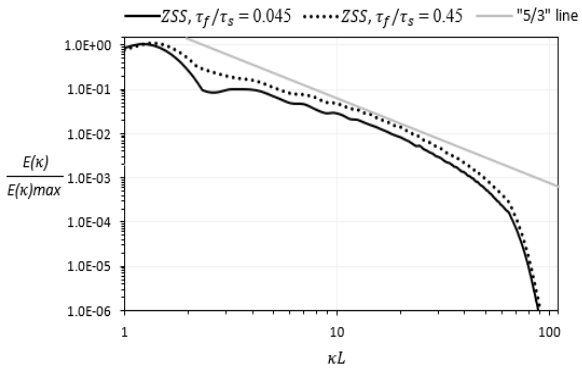

(a) ZSS results, at $\tau_f/\tau_s = 0.45$ and 0.045

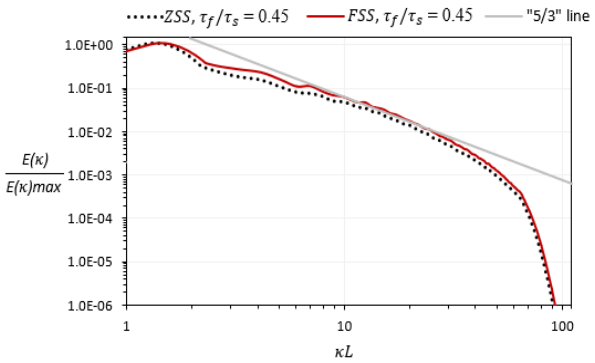

(b) ZSS and FSS results, at $\tau_f/\tau_s = 0.45$

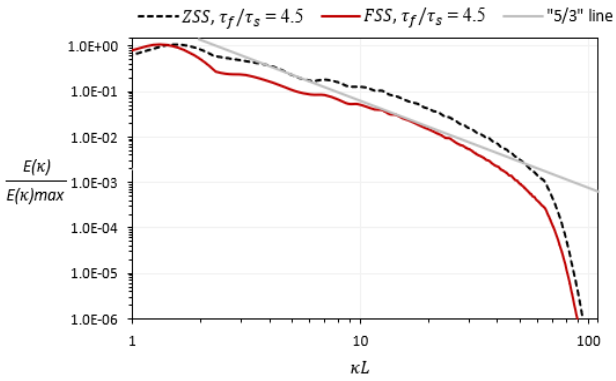

(c) ZSS and FSS results, at $\tau_f/\tau_s = 4.5$

Figure 32. Normalized energy spectra for forcing simulation of homogeneous anisotropic turbulence with volume averaging, on 128^3 grid, (a) zero shear stress (ZSS) at $\tau_f/\tau_s = 0.45$ and 0.045, (b) ZSS and finite shear stress (FSS) results, at $\tau_f/\tau_s = 0.45$, and (c) ZSS and FSS results, at $\tau_f/\tau_s = 4.5$

Table 6 summarizes the results in terms of the resolved turbulence statistics. The maximum difference between the target and resolved Reynolds stress components for each case is shown next to the far-right column. As the strength of the forcing term is increased by decreasing the value of the forcing time scale τ_f, the resolved stress components agree more closely with their target values. For the ZSS case at $\tau_f = 0.045$, the maximum difference is 2.18%. For both isotropic (Table 5) and anisotropic (Table 6) cases, the results indicate that selection of coefficients to provide a sufficiently large forcing term can successfully be used to reproduce the desired target statistics.

6. Summary of turbulence statistics for Homogeneous Anisotropic STF cases

(Green color implies target and over 90% of target statistics)

				Target Reynolds Stress							
				$\overline{u_1'u_1'}^{"}/k^{"}$	$\overline{u_1'u_2'}^{*}/k^{*}$	$\overline{u_1'u_1'}^{"}/k^{"}$	$\overline{u_1'u_3'}^{*}/k$	$\overline{u_3'u_3'}^{"}/k^{"}$	$\overline{u_2'u_3'}^{*}/k^{*}$		
				0.3333	0.2400	0.6666	0.2933	0.9999	0.4133		
				Resolved Reynolds Stress							
Averaging Method	***Finite Shear Stress (FSS)***	τ_f/τ_s	***Grid***	$\overline{u_1'u_1'}/k^{"}$	$\overline{u_1'u_2'}/k^{*}$	$\overline{u_2'u_2'}/k^{*}$	$\overline{u_1'u_3'}/k^{*}$	$\overline{u_3'u_3'}/k^{"}$	$\overline{u_2'u_3'}/k^{*}$	***Max % Difference***	***(k/k*) ratio%***
Volume	No (ZSS)	0.045	128^3	0.3354		0.6520		0.9849		2.18	98.61
Volume	No (ZSS)	0.45	128^3	0.3368		0.5214		0.8291		21.79	84.36
Volume	No (ZSS)	4.5	128^3	0.1964		0.2336		0.2993		70.07	36.46
Volume	Yes (FSS)	0.45	128^3	0.3940	0.1795	0.5618	0.1972	0.7906	0.2780	32.77	87.32
Volume	Yes (FSS)	4.5	128^3	0.0931	0.0220	0.1180	0.0334	0.1678	0.0405	90.84	18.95

4.6. SUMMARY AND CONCLUSION

A new method for synthetic turbulence generation in scale-resolving turbulent flow CFD simulations is presented. The new method, denoted Statistically Targeted Forcing (STF), incorporates a source term in the momentum equation to drive the local, instantaneous velocity vector towards a target value. The target value is computed at each instant and location in the

simulation based on a mapping of the resolved first- and second-order statistics to the desired, target single-point statistics. The resolved statistics can be computed during the simulation using either volume averaging for homogeneous turbulence or time averaging for stationary turbulence.

The method was evaluated by performing several test simulations of homogeneous turbulence, using LES with the Smagorinsky subgrid stress model and or the MILES (implicit LES) modeling approach. Qualitative and quantitative results were presented which showed that the method was able to reproduce the target Reynolds stress components after a relatively short period of simulation time. The simulations using volume averaging responded more quickly than those using time averaging since there is no inherent lag in statistical calculations. It was demonstrated that the forcing time scale can be varied to control the strength of the forcing term, and reducing the time scale was found to be an effective means of reducing the time required for evolution to a quasi-stationary turbulent state, and for improving the accuracy of the forced simulation.

Energy spectra showed that the simulations reproduced the characteristic inertial range scaling when a sufficiently fine mesh was used, although energy pile up occurred near the cutoff wavenumber when an appropriate dissipative subgrid stress model was not employed. It was also demonstrated that spatial filtering can be used to control the effective large-eddy length scale. In sum, the results indicate that the STF method is capable of reproducing a synthetic homogeneous turbulence field with prescribed first- and second-order statistics and appropriate spectral content, which can be used to specify initial and/or boundary conditions for LES simulations. The method is relatively simple to implement, non-stochastic, stable, and computationally efficient. The STF method may therefore offer an attractive alternative for synthetic turbulence generation in three-dimensional Navier-Stokes CFD codes. Future work will investigate extension of the method for

generation of inlet freestream and boundary layer conditions for LES of wall bounded turbulent flows.

CHAPTER V

SCALE-RESOLVING SIMULATIONS OF A STATISTICALLY TARGETED FORCING METHOD FOR SYNTHETIC TURBULENCE GENERATION IN A FREESTREAM TURBULENCE

Work from this chapter has been submitted to the ASME Journal of Fluids Engineering (JFE).

5.1. INTRODUCTION

Freestream turbulence is increasingly important in many engineering applications especially for engineering design and analysis, it has been specified on several occasions as time-dependent turbulence boundary and/or initial (B/I) conditions far upstream of computational domain. It occurs in atmospheric turbulence surrounding aircrafts, resultant wake turbulence from an object, flow turbulence in ducts as well as in unbounded flows and other significant cases in industrial engineering applications. Computational fluid dynamics (CFD) methods for effectively reproducing time-dependent inflow freestream turbulence (FST) boundary conditions in scale-resolving simulations within a spatially developing domain is therefore increasingly needed and is of significant value in many engineering applications. Most importantly, FST is usually specified as a boundary and/or initial (B/I) conditions far upstream of a computational domain, therefore, reproduction or generation of freestream turbulence boundary layer in a spatially developing flow domain is relatively challenging and of particular interest in this study. Simulations with high fidelity methods such as Direct Numerical Simulations (DNS) and Large-Eddy Simulations (LES) are relatively accurate and expensive for industrial applications while

Reynolds-averaged Navier-Stokes (RANS) simulations is less accurate but industrially affordable. Hybrid RANS-LES (HRL) modeling framework has been previously documented in literature to provide a competitive advantage in terms of accuracy and cost compared to either LES or RANS model alone. Therefore, efficient methods for prescribing or reproducing complex conditions such as FST far upstream or within a computational domain is increasingly needed.

The feasibility of resolving freestream turbulence is narrow for most researchers without synthetic turbulence generation (STG), this is because FST is usually located far upstream of the computational domain. Most times, it is not feasible to include the source of turbulent B/I condition within a simulation. For instance, the interaction of an aerodynamic vehicle with a turbulent freestream flow. The source of the freestream turbulence is in fact due to the interaction of the atmospheric boundary layer (ABL) with the ground, but available resources would typically prevent simulating the ABL flow in addition to the local vehicle aerodynamics. Therefore, utilizing STG methods in generating or specifying such a turbulent B/I condition instead of simulating the actual process of natural or bypass laminar-to-turbulent transition via high fidelity methods of DNS or LES, is more appropriate for large Reynolds number. Hence, the purpose of STG methods is to replace turbulent content obtained from fully resolved simulations with a reasonable approximation of turbulence for a substantially lower computational cost. In addition, the methods usually provide the flexibility of selectively locating turbulent content (as turbulence B/I conditions) in specific regions of the computational domain where they are needed.

Research interest on generation of turbulence B/I conditions has been progressive over the past two decades, ranging from library-based methods to recycling/rescaling to synthetic turbulence generation (STG) with controlled forcing. Recycling/rescaling is one of the renowned methods for prescribing turbulence boundary conditions. To produce a recycled turbulent content,

streamwise periodic boundary conditions are imposed on the computational domain or a portion of the domain to ensure that the turbulent flow leaving the outlet is reintroduced at the inlet. Rescaling of the velocity field can be performed to ensure that the turbulent statistics remain appropriately spatially developing. Dhamankar et al. [81], Morgan et al. [80], and Wu [79], previously published that recycling/rescaling facilitate the development of equilibrium turbulence by introducing fluctuations on the inflow boundary. This method was used, for example, by Spalart et al. [78] to perform large-eddy simulation of a turbulent boundary layer. Lund et al. [17] used the recycling/rescaling method to perform an auxiliary simulation of a turbulent boundary layer, and then extracted planes of time-dependent velocity data to be mapped to the inlet of a simulation with a more complex geometry. Several other studies have extended the recycling/rescaling approach to simulate complex wall bounded flows [18-20]. Schlüter et al. [21] used the recycling/rescaling method to impose fluctuating velocities at the outlet to an LES region of a simulation to impose the statistics obtained from a RANS solution in the downstream region.

A different class of methods to recycling/rescaling is synthetic turbulence generation (STG). For applications of practical engineering interest on complex geometries, STG methods have the potential to reproduce turbulent fluctuations at desired locations and with desired statistical distributions, without the need to run an auxiliary simulation. STG methods can also be used to specify inflow boundary conditions as well as initial conditions for a simulation.

Kraichnan [22] proposed one of the first STG methods for isotropic turbulence, by utilizing a spectral approach to artificially produce an isotropic turbulent velocity field from random Fourier modes. This approach of generating isotropic velocity fields with a specified energy spectrum has been used for example to generate initial conditions for DNS of isotropic turbulence [23,24]. Lee et al. [51] similarly proposed a Fourier transform-based STG method to generate

inflow boundary conditions, however one limitation of this method is that it is not applicable to wall-bounded flows due to statistical inhomogeneity in the wall-normal direction.

Using a similar approach for isotropic turbulence, Lundgren [52] defined a forcing term in the momentum equations that is proportional to the fluctuating velocity component. This isotropic linear forcing (ILF) term imitates the natural production mechanism in the turbulent kinetic energy equation. This ILF forcing can be restricted to low wave number modes when using spectral numerical methods. Rosales et al. [53] extended the method in [52] by formulating the forcing term in physical space. In order to control the length scales, it has been suggested in Klein et al. [77] to make the forcing proportional to a high pass filtered velocity fluctuation. However, implementation of a high pass filter on an arbitrary unstructured grid is not straightforward.

A different algorithmic approach proposed by Jarrin et al. [54,55] is the synthetic eddy method (SEM), which is used to generate realistic synthetic eddies at the inflow of an LES simulation. Results have shown that the synthetic eddy field can evolve to physically realistic turbulent flow after a relatively short distance downstream of the inlet. Some limitations exist in the SEM method such as depletion of the smaller scales of turbulence. This has motivated modification of the SEM to include momentum source terms that energize the velocity fluctuations for some distance downstream.

Keating et al. [56] explain how inappropriate modeling of the scale and structure of synthetic turbulence can lead to a rapid dissipation of velocity fluctuations and an increase in the time/distance required for the flow to recover into a fully turbulent state. Therefore, most recent STG methods attempt to introduce some degree of spatial and temporal coherence through artificial control forcing techniques.

Spille-Kohoff and Kaltenbach [57] proposed an inflow STG method based on an added forcing source term in the wall-normal momentum equation. This forcing term enhances the velocity fluctuations in that direction, to match a desired "target" profile of Reynolds shear stress. This technique enhances the wall-normal fluctuations at discrete locations, with amplitude proportional to the difference between the calculated Reynolds shear stress and a provided target profile. This is an example of an STG method with a controlled forcing feedback loop to achieve a target statistical distribution. They documented that the method reduces the error in the Reynolds shear stress to acceptable values within five channel half heights, although the coefficient of friction and the turbulent kinetic energy required longer downstream distances to reach their fully developed values. Similarly, Schmidt and Breuer [76] documented a method that depends on applying a local volume force to superimpose synthetic turbulence at user-specified locations of the computational domain, which can easily be implemented by adding a source term into a Navier–Stokes momentum equation.

Recently, B. de Laage de Meux et al. [58] proposed a method to impose target statistics of the flow in terms of mean velocity and resolved turbulent stress, using a method denoted anisotropic linear forcing (ALF). The time-dependent forcing function is proportional to the instantaneous velocity via a tensor transformation. The method was found to provide accurate results for isotropic, anisotropic, and spatially developing turbulence test cases for LES and hybrid RANS-LES simulations. More recently, Tangermann et al. [64] implemented a STG method that controlled a freestream turbulent intensity based on applying local volume forces has been adapted and supplemented with a control loop in order to compensate for alterations of the turbulence structure resulting from the numerical treatment and physical reasons. The method showed that turbulence length scale and intensity agree with the prescribed target values.

Therefore, formulation of a STG method based on an added forcing source term that is proportional to instantaneous velocity via tensorial transformation can be implemented within a computational domain to match desired target statistics.

This study introduces a recently published statistical targeted forcing (STF) method based on the latter methods. A variant of STG method with controlled forcing within the simulation domain, implemented via added source terms (controller mechanism) in the momentum and energy equations. Recently, Shobayo and Walters [65] validated the STF method for homogeneous isotropic and anisotropic turbulent flow, where results showed that the method can accurately match the desired target statistics. The objective of this study is to investigate the STF method for a freestream turbulent flow using three different classes of modeling approach: RANS, LES, and hybrid RANS-LES. Specifically, this study investigates the capability of STF method to act as a restoring force towards a target statistical state within a time-averaging framework. Furthermore, dynamic hybrid RANS-LES model (DHRL), a type of HRL simulation methodology, has been documented in the literature [36-37,66] as HRL model that provides competitive advantage in terms of accuracy and cost compared to k-ω SST (RANS) [40] or MILES (LES) alone [36]. In general, we seek to investigate and validate STF method's performance, analysis of the influence of STF method parameters, effect of mesh resolution, and effect of choice of modeling frameworks in a freestream turbulent flow.

5.2. SIMULATION DETAILS

This study extends the application of the STF method to reproducing freestream turbulence in a spatially developing turbulent freestream flow domain using k-ω SST (RANS), MILES

(LES), and DHRL models. The STF method is evaluated within the modeling framework of k-ω SST, MILES, Smagorinsky (SMAG), and DHRL models.

The test case considered here is fully developed inflow freestream turbulence in a prototypical hexahedral flow channel that is statistically homogeneous normal to the mean flow direction. The domain extends $10\delta \times 2\delta \times 2\delta$ in the streamwise (x), and normal (y and z) directions, respectively, where δ denotes the half-channel extent in either of the normal directions. Boundary conditions are periodic in the normal directions, and inflow and outflow boundary conditions are specified in streamwise direction.

Simulation results showed that the effective pressure gradient throughout the domain is relatively small and constant, with a total pressure variation of ~ $46Pa$ (<0.05% of 1atm) and is therefore has negligible effect on fluid properties. The remainder of this section briefly reviews the mathematical formulation of the STF method, SST, MILES, SMAG, DHRL models, and other simulation details such as FST channel flow test case geometry, boundary and initial conditions, computational grid, numerical schemes and CFD flow solver.

5.2.1. STF Method Formulation

Shobayo and Walters [65] previously documented that the statistically targeted forcing (STF) method seeks to induce a synthetic turbulence field through the addition of a time-dependent, non-stochastic forcing term in the momentum equation. The forcing term is formulated to drive the instantaneous, local velocity towards a "target" user-specified first- and second-order single-point turbulent statistics i.e., the mean velocity vector and Reynolds stress tensor. The STF method is implemented by adding a forcing term, f_i, to the momentum and

energy equations. The momentum and energy equations, with the forcing term included for single-phase, single-species, compressible flow are briefly reviewed here:

$$\frac{\partial}{\partial t}(\rho u_i) + \frac{\partial}{\partial \mathrm{x_j}}\left(\rho u_i u_j\right) = -\frac{\partial p}{\partial \mathrm{x}_i} + \frac{\partial}{\partial \mathrm{x_j}}\left(\sigma_{ij}\right) + f_i \tag{1}$$

$$\frac{\partial}{\partial t}(\rho E) + \frac{\partial}{\partial \mathrm{x_j}}\left(\rho u_j H\right) = \frac{\partial}{\partial \mathrm{x_j}}\left(q_j + u_i \sigma_{ij}\right) + u_i f_i \tag{2}$$

where f_i is defined as:

$$f_i = \frac{\rho}{\tau_f}(u_i^* - u_i) \tag{3}$$

In the above, the flow variables ρ, u, p, E, and H may represent local instantaneous (DNS) or filtered (LES) quantities. Likewise, the viscous stress tensor σ_{ij} and heat flux vector q_j include both molecular and, for LES, subfilter contributions. Here u_i^* is a target local, instantaneous velocity and τ_f is a characteristic time scale for the forcing term. The STF method is implemented by adding a forcing term, f_i, to the momentum and energy equations.The source term is constructed such that during each time step of a simulation, the resolved velocity vector is forced toward a target velocity vector that would in principle yield a desired target statistical distribution for the time-varying velocity field. Inputs to the model include prescription of a local target mean velocity, $\bar{u}_i^*$, and turbulent stress tensor

$$\overline{u_i' u_j'}^* = \left(\overline{u_i u_j} - \bar{u}_i \bar{u}_j\right)^* \tag{4}$$

where the overbar denotes either Reynolds or Favre (mass-weighted) averaging.

The key aspect of the forcing method is the calculation of the target velocity vector u_i^*. It is first noted that the transformation proposed by can be used to map an ensemble of isotropic velocity fluctuations v' to an ensemble of fluctuations that satisfy a target statistical distribution $T_{ij} = \overline{u_i' u_j'}^*$ as follows:

$$u_i'^* = B_{ij} v_j' \tag{5}$$

$$B_{ij} = \begin{bmatrix} \sqrt{T_{11}} & 0 & 0 \\ T_{21}/B_{11} & \sqrt{T_{22} - B_{21}^2} & 0 \\ T_{31}/B_{11} & (T_{32} - B_{21}B_{31})/B_{22} & \sqrt{T_{33} - B_{31}^2 - B_{32}^2} \end{bmatrix} \tag{6}$$

Similarly, an ensemble of resolved fluctuations satisfying a particular statistical distribution $R_{ij} = \overline{u_i' u_j'}$ can be mapped to an isotropic distribution v' using the inverse of the Lund coefficient matrix:

$$v_i' = A_{ij}^{-1} u_j' \tag{7}$$

$$A_{ij}^{-1} = \begin{bmatrix} 1/A_{11} & 0 & 0 \\ -A_{21}/(A_{11}A_{22}) & 1/A_{22} & 0 \\ (A_{21}A_{32} - A_{31}A_{22})/(A_{11}A_{22}A_{33}) & -A_{32}/(A_{22}A_{33}) & 1/A_{33} \end{bmatrix} \tag{8}$$

$$A_{ij} = \begin{bmatrix} \sqrt{R_{11}} & 0 & 0 \\ R_{21}/A_{11} & \sqrt{R_{22} - A_{21}^2} & 0 \\ R_{31}/A_{11} & (R_{32} - A_{21}A_{31})/A_{22} & \sqrt{R_{33} - A_{31}^2 - A_{32}^2} \end{bmatrix} \quad (9)$$

It is therefore possible to define a mapping from a distribution of resolved velocity fluctuations u_i' with known statistical second moment tensor (turbulent stress) R_{ij} to a distribution $u_i'^*$ with target turbulent stress T_{ij} as:

$$u_i'^* = C_{ij} u_j' \quad (10)$$

$$C_{ij} = B_{ik} A_{kj}^{-1} \quad (11)$$

The instantaneous target velocity used in the forcing function includes the target fluctuating velocity as well as the target mean velocity:

$$u_i^* = \bar{u}_i^* + C_{ij} u_j' \quad (12)$$

Where the fluctuating velocity is defined relative to the mean:

$$u_i' = u_i - \bar{u}_i \quad (13)$$

In practice STF method is implemented as follows. First a target statistical velocity distribution is specified prior to the simulation in terms of $\bar{u}_i^*$ and $\overline{u_i' u_j'}^*$. As the simulation proceeds, the resolved statistics $\bar{u}_i$ and $\overline{u_i' u_j'}$ are obtained using an appropriate averaging technique. At each time step, the transformation tensor C_{ij} is computed at each point in the domain based on $\overline{u_i' u_j'}^*$ and $\overline{u_i' u_j'}$. During each iteration, the fluctuating velocity u_i' is computed, and the target instantaneous velocity u_i^* is found using Eq. (12). The forcing term f_i defined in Eq. (14) is then computed using Eq. (3) and included as an additional source term in the momentum and energy equations. Shobayo and Walters [65] concluded that the forcing term can be defined as a function of the characteristic large-eddy turbulent timescale, τ_T, forcing coefficient, f_c (C_f [65]), and target fluctuating velocity, u_i^*. Type of spatial filtering and averaging method used for the simulations in this study are anisotropic spatial filtering and time averaging respectively. For further details on the STF method, readers are referred to Ref. [65].

$$f_i = \rho \frac{f_c}{\tau_T}(u_i^* - u_i) \tag{14}$$

5.2.2. Spatial Filtering

Spatial filtering is implemented in the STF method to allow the user to have some measure of control of the turbulent length scale. All simulations adopting spatial filtering in this study were performed using a second-order differential elliptic filter [27]. In this method, for anisotropic filter, the filtered resolved velocity ($\hat{u}_i$) is obtained by solution of Eq. (15), where ϕ_{jk} is the tensorial filter width or size:

$$\frac{\partial}{\partial x_j}\left(\phi_{jk}\frac{\partial \hat{u}_i}{\partial x_j}\right) = \hat{u}_i - u_i \tag{15}$$

Spatial filtering is implemented in the STF method by first re-defining fluctuating velocity (u_i') in Eq. (16) as filtered fluctuating velocity (u_i''):

$$u_i'' = (u_i - \hat{u}_i) - \left(\bar{u}_i - \bar{\hat{u}}_i\right) \tag{16}$$

The instantaneous target velocity used in the forcing function includes the target filtered fluctuating velocity ($C_{ij}u_j''$) as well as the target mean velocity ($\bar{u}_i^*$):

$$u_i^* = \bar{u}_i^* + (\hat{u}_i - \bar{u}_i) + C_{ij}u_j'' \tag{17}$$

At every iteration, the filtered transformation tensor C_{ij} is computed at each point in the domain based on a modified target turbulent stress, T_{ij}, and resolved turbulent stress, R_{ij}, where M_{ij} is a term that represents the contribution to the turbulent stress by the interaction between the filtered and instantaneous velocity:

$$T_{ij} = \overline{u_i' u_j'}^* - M_{ij} \tag{18}$$

$$R_{ij} = \overline{u_i' u_j'} - M_{ij} \tag{19}$$

$$M_{ij} = \frac{1}{2}\left[\left(\overline{\hat{u}_i u_j} + \overline{u_i \hat{u}_j}\right) - \left(\bar{\hat{u}}_i \bar{u}_j + \bar{u}_i \bar{\hat{u}}_j\right)\right] \tag{20}$$

Equation (15) represents an isotropic spatial filtering operation. In practice, the STF method adopts a generalized anisotropic filter defined by:

$$\frac{\partial}{\partial x_j}\left(\tau_T^2 \, \overline{u_j' u_k'}^* \, \frac{\partial \hat{u}_i}{\partial x_k}\right) = \hat{u}_i - u_i \tag{21}$$

Anisotropic filtering is a relatively simple way to incorporate the fact that turbulence can have different length scales in different directions. The method assumes that regardless of their length scale, large eddies (i.e. velocity fluctuations) will share the same time scale. The tensorial filter width is defined to depend on a characteristic turbulent time scale, τ_T, and the target turbulent stress tensor, $\overline{u_i' u_j'}^*$. For freestream turbulence, spatial variations and turbulent fluctuations are not statistically uniform in all directions and the filtered resolved velocity ($\hat{u}_i$) is obtained by solution of Eq. (21). For isotropic turbulence, the anisotropic filtering operation is formally similar to the isotropic filter defined in Eq. (15). For this case, spatial variations and turbulent fluctuations are statistically uniform in orthogonal and spanwise directions only, hence the tensorial filter width is defined as:

$$\phi_{jk} = \tau_T^2 \left(\overline{u_j' u_k'}^*\right) \tag{22}$$

5.2.3. Shear-Stress Transport (SST) Model

A commonly used example of the RANS modeling approach is the Shear-Stress Transport (SST *k*-ω) model [40]. It has been widely and successfully used for practical RANS CFD simulation of complex turbulent flows. Recall the overbar in Eq. (4) represents Reynolds-averaging (for this model), the turbulent stress tensor and eddy viscosity is modeled using the Boussinesq hypothesis as:

$$\tau_{ij}{}^{RANS} = \nu_t \left(\frac{\partial \overline{u_i}}{\partial x_j} + \frac{\partial \overline{u_j}}{\partial x_i}\right) - \frac{2}{3}\bar{k}\delta_{ij} \tag{23}$$

$$\nu_t = \frac{a_1 k}{max(a_1 \omega, SF_{sst})} \tag{24}$$

where F_{sst} is a blending function, a_1 is a constant, and S represents an invariant measure of the strain-rate magnitude. F_{sst} obtains a value of unity for boundary-layer flows, and a value of zero for free shear layers far from a wall.

Two transport equations, one for the turbulent kinetic energy (k) and the other for the specific turbulence dissipation rate (ω), are incorporated into the SST k-ω modeling framework as follows:

$$\frac{D\rho k}{Dt} = \tau_{ij}\frac{\partial u_i}{\partial x_j} - \beta^*\rho\omega k + \frac{\partial}{\partial x_j}\left[(\mu + \sigma_k\mu_t)\frac{\partial k}{\partial x_j}\right] \quad (25)$$

$$\frac{D\rho\omega}{Dt} = \frac{\gamma}{\nu_t}\tau_{ij}\frac{\partial u_i}{\partial x_j} - \beta\rho\omega^2 + \frac{\partial}{\partial x_j}\left[(\mu + \sigma_\omega\mu_t)\frac{\partial \omega}{\partial x_j}\right] + 2(1-F_1)\rho\sigma_{\omega 2}\frac{1}{\omega}\frac{\partial k}{\partial x_j}\frac{\partial \omega}{\partial x_j} \quad (26)$$

The blending function F_1 plays a similar role as F_{sst}, serving as an indicator function for near-wall and far field regions of the flow. Near the wall, $F_1 = 1$, and a k-ω model form is recovered. Far from the wall, F_1 tends to 0. For further details on the model, readers are referred to Ref. [40]. Some simulations in this study used the STF method with SST k-ω model to compare the model's performance with MILES and DHRL in reproducing synthetic freestream turbulence. Particularly, the modeled "turbulent kinetic energy" (k) for this model is compared with "target" k, and hybrid or resolved k of other models.

5.2.4 Monotonically Integrated LES (MILES) and LES Subgrid Stress Model

Some simulations presented here use both the Smagorinsky eddy-viscosity based subgrid stress model [61], and Monotonically Integrated LES (MILES) [62]. Three reasons are apparent for the two choices of LES models, first, to investigate effect of explicit LES modeling compared to Implicit LES, second, to examine effect of spatial filtering on STF method for both cases, and third, to evaluate DHRL model, when the LES component is MILES and/or Smagorinsky model. The Smagorinsky (SMAG) eddy-viscosity based subgrid stress model, deviatoric part of subgrid stress tensor and eddy-viscosity are expressed as:

$$\tau_{ij}^{SGS} = 2\nu_T S_{ij} \quad (27)$$

The eddy viscosity is formulated as:

$$\nu_T = (C_s \Delta)^2 \sqrt{2S_{ij}S_{ij}} \quad (28)$$

where Δ is the characteristic mesh size, equal to the cube root of cell volume in the current simulations, and the coefficient $C_s = 0.1$ is used for related simulations. For MILES model – Implicit LES model [62], which has been widely and successfully used for practical LES simulation of complex turbulent flows. For clarity, the fundamental differences between conventional LES modelling and MILES. The conventional LES approach such as that of Smagorinsky [61], uses an explicit model for the deviatoric part of the subgrid stress tensor based on a (subgrid) eddy viscosity as shown in Eqs. (23-24). In contrast, for the MILES model, τ_{ij}^{SGS} is modeled as zero ($\tau_{ij}^{SGS} = 0$), and the turbulent stress tensor (τ_{ij}^{MILES}), is implemented using high-resolution upwind algorithms for the convective terms, such as the Monotonic Upwind Scheme for Conservation Laws (MUSCL). Nonlinear high-frequency filters built into the numerical algorithms effectively provide implicit SGS models, in which the numerical dissipation serves to represent the effect of subfilter scales on the resolved variable fields.

5.2.5 Dynamic Hybrid RANS-LES (DHRL) Formulation

A detailed formulation of the DHRL modeling methodology is available in Walters et al. [36]. DHRL is most appropriately considered as a framework for blending arbitrary RANS and LES model variants into a hybrid RANS-LES model, rather than a specific model in itself. The following sections briefly present the previously documented baseline RANS-LES blending

methodology for the DHRL model. For further details on DHRL and variants, interested readers are referred to Refs. [36-37,66]. The hybrid turbulent stress tensor (τ_{ij}), and the blending function (α) are expressed as:

$$\tau_{ij} = \alpha\tau_{ij}^{SGS} + (1-\alpha)\tau_{ij}^{RANS} \tag{29}$$

$$\alpha = \frac{\underbrace{\overline{u_i''u_j''}\,\overline{S_{ij}}}_{\substack{Resolved\ turbulent \\ Production}}}{\underbrace{\tau_{ij}^{RANS}\overline{S_{ij}}}_{\substack{RANS \\ Production}} - \underbrace{\overline{\tau_{ij}^{SGS}}\,\overline{S_{ij}}}_{\substack{Inhomogeneous \\ SGS\ Production}}} \tag{30}$$

The terms τ_{ij}^{SGS} and τ_{ij}^{RANS} are the subgrid stress predicted by any candidate LES model and the turbulent stress predicted by any candidate RANS model, respectively. The numerator in Eq. (26) represents the production of turbulent kinetic energy (k) due to the resolved turbulent scales in the flow. The term in the denominator is the difference of $\tau_{ij}^{RANS}\overline{S_{ij}}$, which is the production of k predicted by the RANS model, and $\overline{\tau_{ij}^{SGS}}\,\overline{S_{ij}}$, which is the mean component of the subgrid scale turbulent kinetic energy production. Eq. (25) indicates that the model operates in a pure LES mode only if the resolved scale production is equal to or greater than the predicted RANS production; otherwise, the model behaves in a transitional mode where an additional RANS stress compensates for reduced LES content. This leads to a smooth variation of turbulent production across the transition region. In regions with zero LES content, i.e. numerically steady flow, the model operates in a pure RANS mode. For the current model implementation, the RANS part of DHRL is found using the eddy viscosity computed by the k-ω SST model as shown in Eqs. (11-

12). MILES is used for the LES model component, hence τ_{ij}^{SGS} is zero. Application of the STF method within hybrid RANS-LES framework is tested with this model, and its performance is compared with other models.

5.2.6. FST Channel Flow (FST-CF) Test Case

The FST-CF test case represents a prototypical flow with uniform mean velocity in the streamwise direction and periodic boundary conditions in the normal directions. The mean velocity is non-zero in streamwise direction only. The FST-CF implies a nearly homogeneous turbulence domain except that turbulence varies only in the streamwise direction. It provides a simple geometry that allows for investigation of spatial development of turbulence statistics particularly when the STF method forcing is active and when turbulent kinetic energy (k) decay is apparent downstream of the forcing region. The FST-CF domain had dimensions of $L_x \times L_y \times L_z = 10\pi \times 2\pi \times 2\pi$, half-channel height, δ is π, and all boundaries were periodic except the inflow and outflow boundaries. For all the simulations in this study, both inlet conditions and initial conditions are specified to be: u_1 = 35.22 m/s, $u_2 = u_3 = 0$, and ρ and T some constant values chosen to yield the appropriate Mach number (Ma =0.1) and Reynolds number (Re = 7000). The freestream velocity (U_∞), freestream temperature (T_∞) and density (ρ_∞) are specified as inlet boundary and initial conditions. The freestream Mach number was close to 0.1, which approximates incompressible flow conditions Inflow and outflow boundary conditions (BC) are specified in streamwise directions, periodic BC is imposed in orthogonal and spanwise directions. Two structured, uniform, Cartesian meshes were used for the simulations, corresponding to a coarse mesh of 1,310,720 ($320 \times 64 \times 64$) cells, and a refined mesh of

10,485,760 ($640 \times 128 \times 128$) cells. The FST-CF geometry is illustrated in Fig. 1, showing the coordinates, channel half-height (δ), and location of the inflow and outflow boundary conditions.

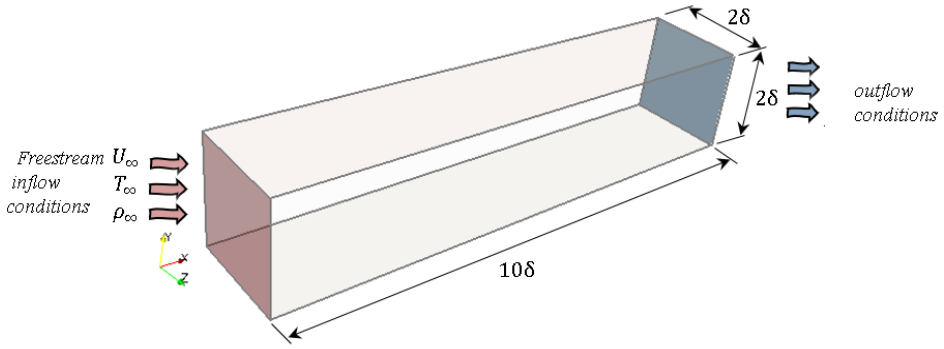

Figure 33. FST-CF Computational domain

The study focuses on investigating the complex flow physics in the spatial development of freestream turbulence along the streamwise distance due to varying intensities of STF forcing particularly from region of turbulent kinetic energy (k) production to when turbulent kinetic energy (k) decay is apparent. Hence, key issues investigated included:

- Effect of mesh resolution on STF Method and different modeling approaches
- Effect of critical parameters such as turbulence time scale, length scale, and forcing coefficient on the method
- Spectral characteristics of the turbulence generated by the forcing method at different streamwise distances
- Method performance when turbulent kinetic energy (k) level is constant and when k decay is apparent

- Comparison of STF method prediction of resolved turbulent statistics with target turbulent statistics using k-ω SST, MILES, Smagorinsky, and DHRL models

5.2.7. STF Forcing Region with Boundary and Initial (B/I) Conditions

For the FST-CF domain, the target statistics in the STF method forcing region ($0 \leq x \leq 2\pi$), the inflow and outflow boundary conditions (BCs), and other freestream inflow turbulence conditions, the target statistics, are illustrated in Fig. 34, where periodic boundary conditions (BC) are imposed in both orthogonal and spanwise directions. Periodic BCs are applied on the normal directions. Freestream temperature and density are relatively constant throughout the domain, the flow domain is within incompressibility conditions with Mach number of approximately 0.1. The imposed mean pressure gradient is relatively small and less than 1.5Pa/m, this initiates the flow and relatively retain the fluid properties.

$$\bar{u}_1^* = U_\infty = 35.22\ m/s \ \text{ and } \ \overline{u_1'u_1'}^* = \overline{u_2'u_2'}^* = \overline{u_3'u_3'}^* = 50\ m^2/s^2 \tag{31}$$

$$\overline{u_1'u_2'}^* = \overline{u_1'u_3'}^* = \overline{u_2'u_3'}^* = 0 \tag{32}$$

5.2.8. Computational Fluid Dynamics Solver

All simulations in this study were performed using the open source CFD code FlowPsi [59], a finite-volume density-based solver constructed in C++ using the Loci framework. FlowPsi uses high-resolution approximate Riemann solvers and implicit numerical methods. For the present

study, all simulations were run with a Mach number close to 0.1, based on inflow freestream velocity, U_∞ to simulate incompressible flow conditions. Inviscid fluxes are reconstructed using a modified skew symmetric flux (SSF) scheme. The SSF scheme is a generalization of the kinetic energy consistent (KEC) central difference scheme of Subbareddy and Candler [60], blended with a small second-order upwind flux contribution. For all simulations in this paper, the blending distribution was 95% central difference and 5% upwind. The SSF scheme has been shown to provide low numerical dissipation and effective resolution of high wavenumber velocity and pressure modes in unsteady turbulent flow simulations.

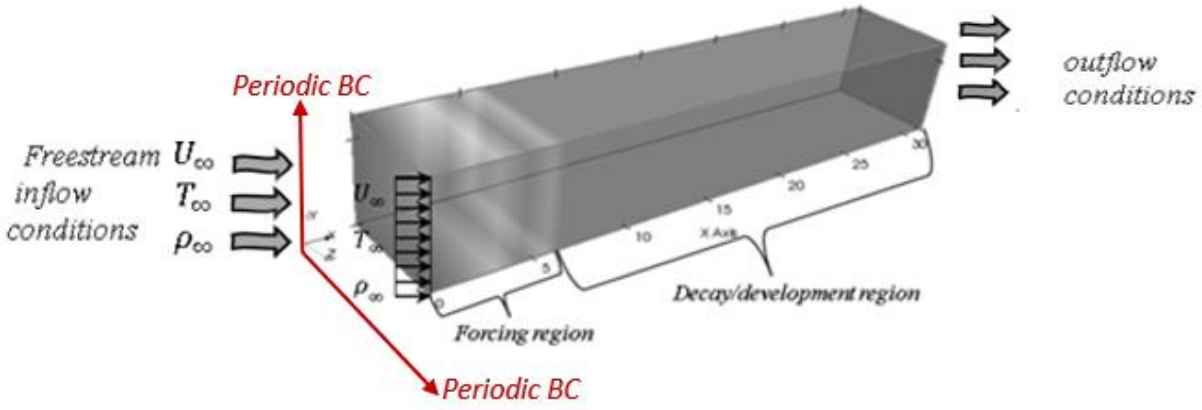

Figure 34. Illustration of initial and boundary conditions, STF forcing and development regions.

5.2.9 Computational Grid

Ansys meshing software was used to generating two structured single-block computational grids. Five uniform coarse grids of 64^3 (262,144) cells were merged along the streamwise direction to generate a single-block coarse grid of 1,310,720 cells, and similarly, five uniform refined grids of 128^3 (2.0972 million) cells were merged to a single-block refined grid of 10,485,760 cells. The characteristic mesh size (Δ) for coarse and refined grids are $\frac{2\delta}{64}$ and $\frac{2\delta}{128}$.

The two meshes were used to investigate the effect of mesh size on the STF method using different modeling methods. Fig. 35 provides an illustration of the two-dimensional views of the computational grids including topology and resolution levels for the coarse and refined cases.

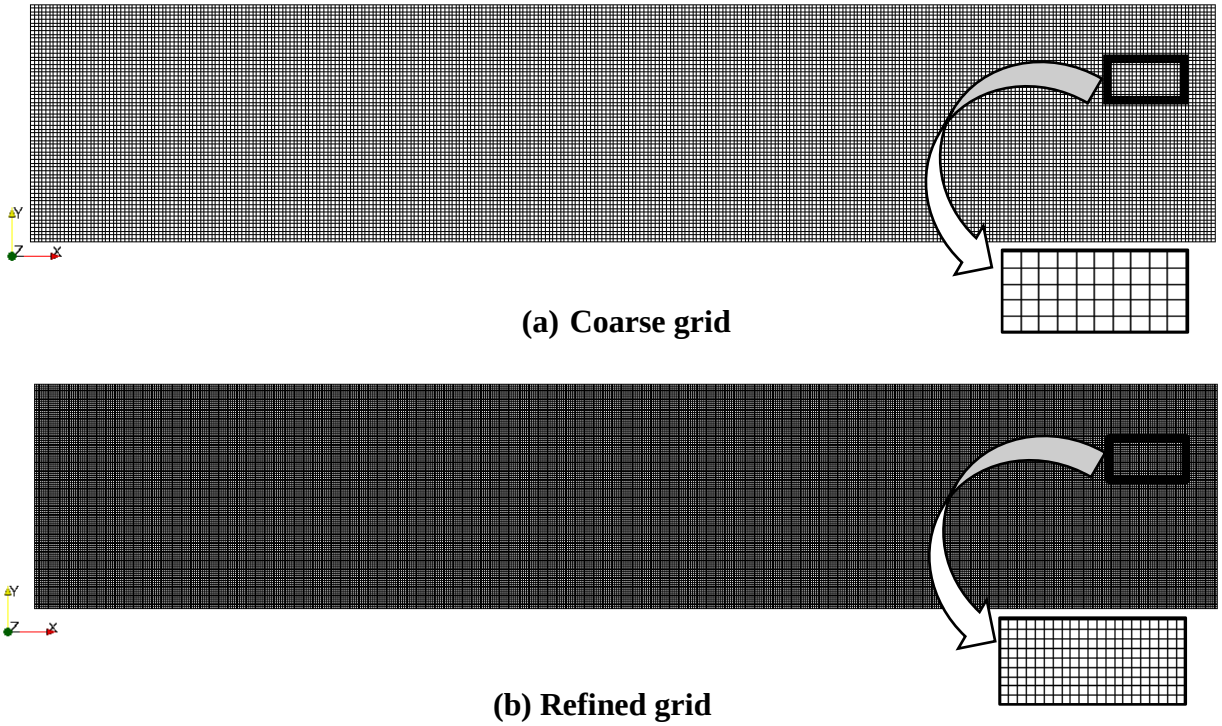

Figure 35. 2D-view computational (a) coarse grid, and (b) refined grid

5.3. RESULTS AND DISCUSSION

Table 7 summarizes the results of freestream turbulence (FST) statistics for STF cases at x/δ =2, which corresponds to the downstream extent of the forcing region. Results are shown for

both MILES and DHRL models, on coarse and refined grid, with and without spatial filtering, and with varying values of τ_f and τ_T. The Table highlights ratios of resolved-to-target mean velocity, resolved-to-target Reynolds stress components, and maximum percentage difference between resolved Reynolds stress components for each case. As the strength of the forcing term is increased by reducing the value of τ_f, the resolved stress components agree more closely with their target values. Data highlighted in green denotes resolved turbulent kinetic energy of over 90% of the target value, indicating that the STF produces well resolved turbulence statistics in terms of one-point correlations. The remainder of this section discusses the results in more detail, including the effects of turbulence model, mesh size, spatial filtering, and STF method parameter values.

Table 7. Summary of Freestream turbulence (FST) statistics for STF cases at x/δ =2 (Target values are highlighted in yellow. Green color indicates simulation that resolves over 90% of target turbulent kinetic energy.)

					Target Mean Velocity and Reynolds Stress at x/δ =2					
					$U_\infty/\ \bar{u}_1^*$	$\overline{u_1'u_1'}^{"}/k^{"}$	$\overline{u_2'u_2'}^{"}/k^{"}$	$\overline{u_3'u_3'}^{"}/k^{"}$		
					1	0.6666	0.6666	0.6666		
					Velocity	*Resolved Reynolds stress*				**tke_ratio**
FST Cases	***Spatial Filtering***	$\tau_T/\ \tau_\infty$	$\tau_f/\ \tau_\infty$	***Grid***	$\bar{u}_1/\ \bar{u}_1^*$	$\overline{u_1'u_1'}/k^{"}$	$\overline{u_2'u_2'}/k^{*}$	$\overline{u_3'u_3'}/k^{"}$	***Max % Difference***	***(k/k*) ratio%***
DHRL	No		0.045	5 x 64^3	0.9990	0.6342	0.6073	0.6071	8.92	92.43
MILES	No		0.045	5 x64^3	0.9983	0.6373	0.6087	0.6087	8.69	92.74
DHRL	No		0.045	5 x128^3	0.9949	0.5971	0.5838	0.5794	13.08	88.01
MILES	No		0.045	5 x128^3	0.9949	0.5961	0.5839	0.5799	13.01	87.99
DHRL	No		0.45	5 x 64^3	1.0017	0.4255	0.3337	0.3336	49.95	54.64
MILES	No		0.45	5 x 64^3	1.0005	0.4363	0.3349	0.3351	49.76	55.32
DHRL	No		4.5	5 x 64^3	1.0029	0.0692	0.0296	0.0298	95.55	6.43
MILES	No		4.5	5 x 64^3	1.0029	0.0698	0.0298	0.0297	95.54	6.46
DHRL	Yes		0.045	5 x 64^3	0.9992	0.6311	0.6013	0.6009	9.85	91.66
MILES	Yes	4.5	0.045	5 x 64^3	0.9993	0.6299	0.6006	0.6004	9.92	91.55
SMAG	No		0.045	5 x 64^3	1.0001	0.6259	0.6296	0.6292	6.11	94.23
SMAG	Yes	4.5	0.045	5 x 64^3	0.9993	0.6299	0.6006	0.6004	9.92	91.55
MILES	Yes	2.25	0.045	5 x 64^3	0.9999	0.6464	0.6232	0.6232	6.52	94.64
MILES	Yes	1.12	0.045	5 x 64^3	1.0008	0.6491	0.6322	0.6315	5.27	95.64
MILES	Yes	0.56	0.045	5 x 64^3	1.0006	0.6459	0.6292	0.6288	5.67	95.19

5.3.1 Instantaneous and Mean velocity

In order to normalize presented results, a freestream characteristic time scale is defined as $\tau_\infty = \delta/U_\infty$. Figure 36 shows the contours of streamwise instantaneous (u_1/U_∞) and mean velocity $(\bar{u}_1/U_\infty)$ for forcing simulation of freestream turbulence at a turbulent time scale $\tau_f/\tau_\infty = 0.045$, using both the MILES and DHRL modeling approaches on the coarse grid.

Specifically, Fig. 36(a) shows a three-dimensional view of the flow domain, and it is apparent that the magnitude of resolved turbulent fluctuations is higher in the forcing region, $0 \leq x/\delta < 2$ than in the downstream development region, $2 \leq x/\delta \leq 10$, where forcing is zero. Downstream of the forcing region, the turbulence level decays in the streamwise direction as expected. Both DHRL and MILES results show resolved turbulent velocity fluctuations at all streamwise locations. Though not shown, results using the SST k-ω RANS model yielded only the mean flow solution as expected, with constant velocity (u_1) throughout the domain.

In the forcing region, the STF method enforces a relatively constant mean flow for the scale-resolving models, as expected. For each of the models investigated, the mean velocity at all points in the domain was within 0.3% of the prescribed target value, U_∞. Small observed differences can be attributed to uncertainty in statistical averaging, which necessarily occurred over a finite time interval. Figure 36(b) shows contours of streamwise instantaneous velocity (u_1/U_∞) on planar slices at different streamwise locations. The contours show qualitative reproduction of turbulent flow structures, and decay of turbulent kinetic energy downstream of the forcing region.

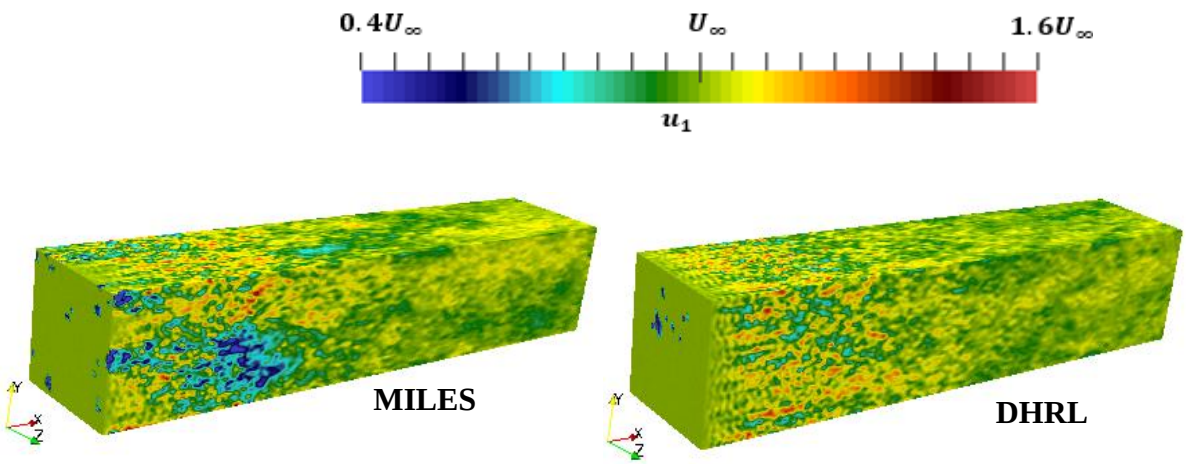

(a) 3D view

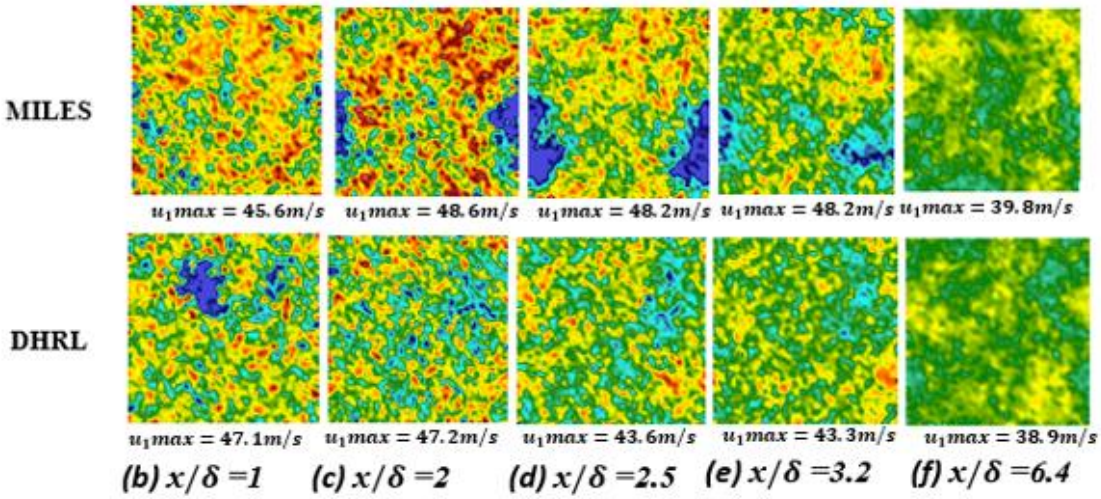

(b) 2D view

Figure 36. Contours of streamwise instantaneous velocity for forcing simulation of freestream turbulence with $\tau_f/\tau_\infty = 0.045$ using MILES, and DHRL models: (a) 3D view; (b) 2D yz-plane view at different streamwise locations.

5.3.2 Streamwise Normal Reynold Stress

Figure 37 shows contours of the streamwise normal Reynolds stress ($\overline{u_1' u_1'}$) for forcing simulation of freestream turbulence with forcing time scale $\tau_f/\tau_\infty = 0.045$, for MILES and DHRL models on the coarse grid. An initial spike in the turbulent stress is apparent immediately downstream of the inlet, followed by a region in which it remains relatively constant over the remainder of the forcing region. Downstream of the forcing region ($2 \leq x/\delta \leq 10$), the stress decays in the streamwise direction as expected.

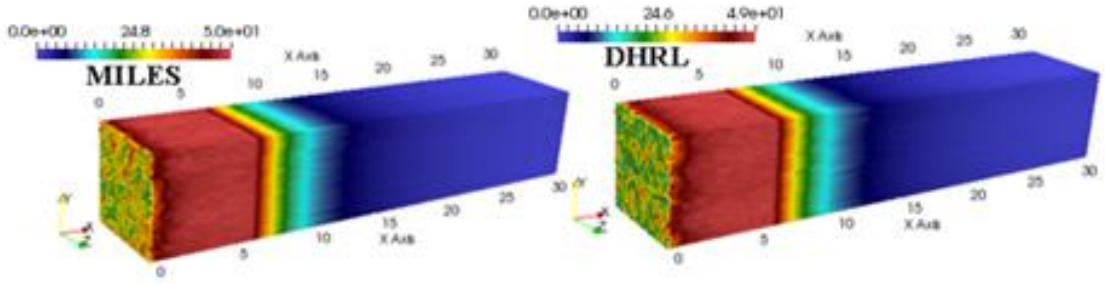

Figure 37. Contours of streamwise normal Reynolds stress ($\overline{u_1' u_1'}$) for forcing simulation of freestream turbulence with $\tau_f/\tau_\infty = 0.045$, using MILES and DHRL models.

Fig. 38 shows a plot of the spatial evolution of normalized resolved normal stress $\overline{(u_1' u_1'}/\overline{(u_1' u_1'}^*)$ for STF forcing simulations of freestream turbulence with $\tau_f/\tau_\infty = 0.045$ using SST, MILES, and DHRL models on the coarse grid. Results shown are planar-averaged over the *y* and *z* directions, but as seen in Fig. 5 the turbulent stress is relatively uniform over cross-sections normal to the streamwise direction. Simulations with the SST model predicted a peak value at the

inlet ($x/\delta = 0$), and monotonic decay in the streamwise direction since no forcing of turbulent velocity fluctuations was applied for that model. Near the outlet of the forcing region at $x/\delta = 2$, both the DHRL and MILES results underpredict $\overline{u_1' u_1'}^*$ by 5%. Downsteam of the forcing region, spatial decay of $\overline{u_1' u_1'}$ is more rapid with DHRL and MILES results compared to the SST model. This is likely due to the fact that the large-eddy length scales in the scale-resolved simulations are relatively small (this can be seen qualitatively for example in Fig. 38), while the effective length scale for the SST model is significantly larger. Increasing the inlet boundary condition value for specific dissipation rate (ω) in the SST simulations would result in a more rapid decay of TKE and closer agreement with the MILES and DHRL results. Both qualitative and quantitative results in Figs. 36-38 indicate that the results obtained with the MILES and DHRL models are in very close agreement. This is to be expected since the mean flow gradient for this freestream flow case is zero everywhere, and observing Eqs. (29,30) it is apparent that the DHRL model should operate in a pure LES mode. The results presented here (and other results though not shown) confirm that the use of the STF forcing method does not negatively impact the ability of the DHRL model to effectively resolve turbulence in LES mode for freestream flow. For the remainder of the paper, only pure LES results using MILES or the Smagorinsky model will be shown as representative of scale-resolving simulations.

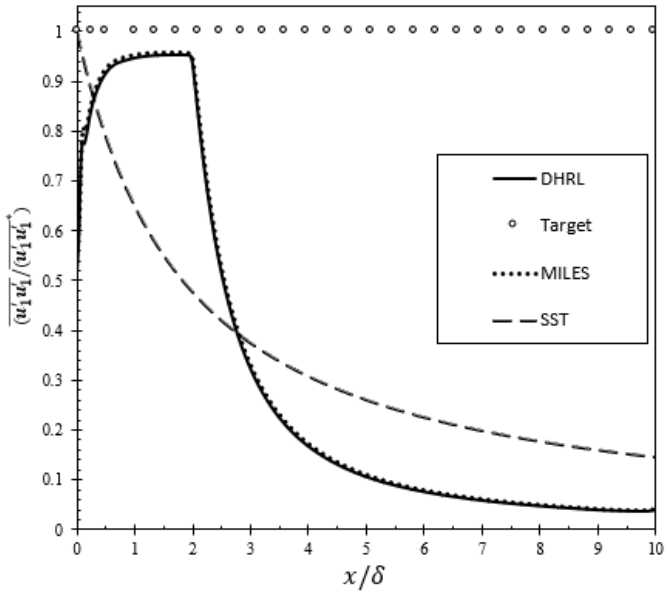

Figure 38. Spatial evolution of normalized resolved normal stress $\overline{(u_1'u_1')}/\overline{(u_1'u_1')}^*$) for forcing simulation of freestream turbulence with $\tau_f/\tau_\infty = 0.045$ using SST, MILES, and DHRL models to compute turbulence statistics

5.3.3 Turbulent Kinetic Energy

Figure 39 shows contours of resolved turbulent kinetic energy (k) for forcing simulations of freestream turbulence with $\tau_f/\tau_\infty = 0.045$ on the coarse grid. Similar to Fig. 37, higher values of k are apparent at $0 \leq x/\delta < 2$, while a decay is evident downstream of the forcing region at $2 \leq x/\delta \leq 10$. Each of the normal Reynolds stress components behaves similarly to the streamwise component, with a relatively rapid increase to near the target value just downstream of the inlet, followed by a nearly constant distribution in the forcing region, and decay downstream of the forcing region. As a consequence k follows a similar pattern. The

distribution of turbulent kinetic energy is shown quantitatively in Fig. 40, with looks similar to the MILES result shown in Fig. 38 for normalized streamwise Reynolds stress.

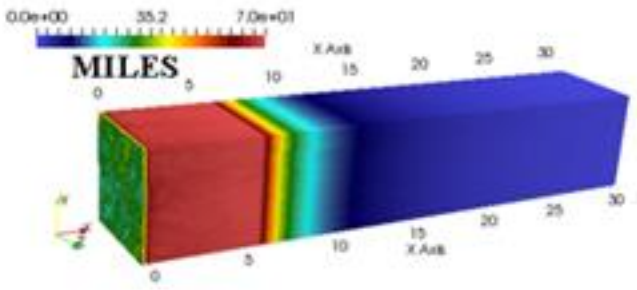

Figure 39. Contours of resolved turbulent kinetic energy (k) for forcing simulation of freestream turbulence with $\tau_f/\tau_\infty = 0.045$ using SST, MILES, and DHRL models to compute turbulence statistics.

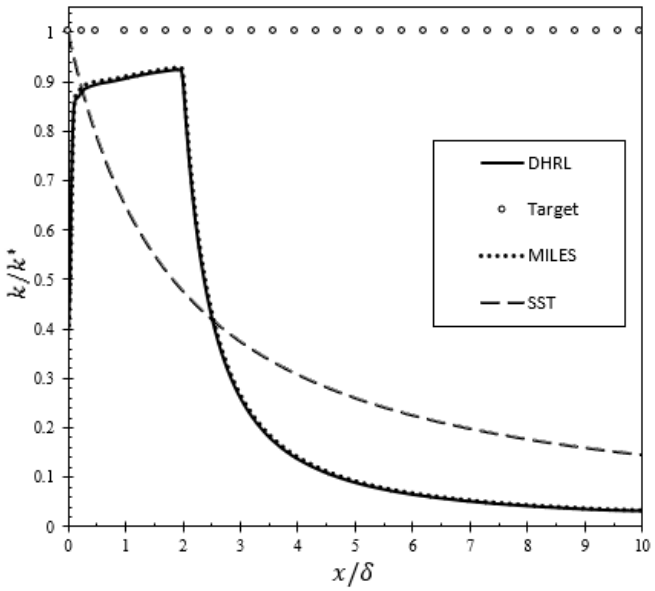

Figure 40. Spatial evolution of normalized turbulent kinetic energy (k/k^*) for forcing simulation of freestream turbulence with $\tau_f/\tau_\infty = 0.045$ using SST, MILES, and DHRL models.

Figure 41 shows the time evolution of normalized turbulent kinetic energy (k/k^*) during the first 0.5 seconds of simulation time for forcing simulation of freestream turbulence with $\tau_f/\tau_\infty = 0.045$ on the coarse grid. The value shown is volume-averaged over the entire flow domain. There is an initial spike in resolved TKE as the model rapidly inputs energy due to the initially low value of resolved TKE obtained from statistical averaging. As the simulation proceeds, there is an initial transient period followed by an asymptotic evolution to the final, stationary value.

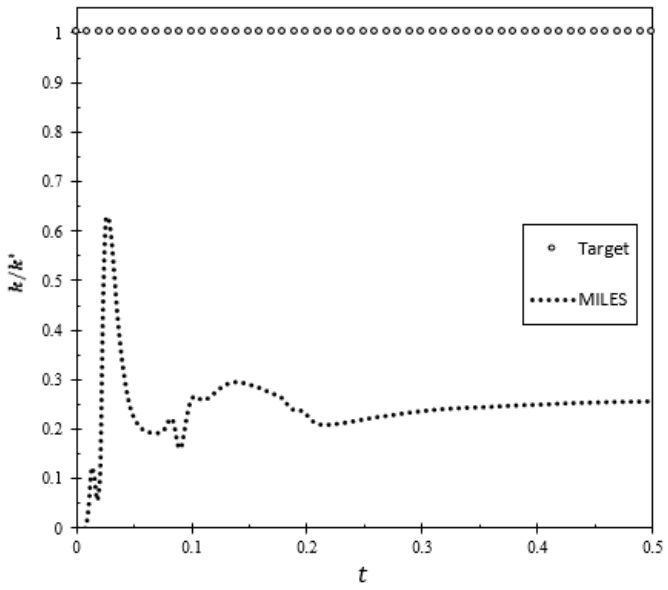

Figure 41. Time evolution of normalized turbulent kinetic energy (k/k^*) for forcing simulation of freestream turbulence with $\tau_f/\tau_\infty = 0.045$ during the first 0.5 second of the simulation time.

To investigate the spectral characteristics of the turbulence generated by the synthetic forcing method at different streamwise locations, a single-point temporal fast Fourier transform was applied to the velocity field at different probe locations corresponding to x/δ =*1*, *2*, and *6.4* and integrated over a time period in frequency (f) space to obtain the energy spectrum density as a function of frequency for forcing simulation of freestream turbulence with $\tau_f/\tau_\infty = 0.045$. The result is shown in Fig. 42. The SST model is not considered due to that model's negligible velocity fluctuations. Also shown for reference is the Kolmogorov -5/3 law denoted as "5/3 line" in the figure. At x/δ =*1*, the energy density appears to be nearly unform up to the cut off frequency imposed by the mesh size and the mean velocity. Farther downstream in the forcing region, at x/δ =*2*, the spectrum has shifted to reflect a shape more indicative of Kolmogorov inertial range

scaling. Downstream of the forcing region at x/δ =6.4, energy decay is apparent, and the spectrum even more closely approximates the correct shape and shows evidence of an inertial subrange.

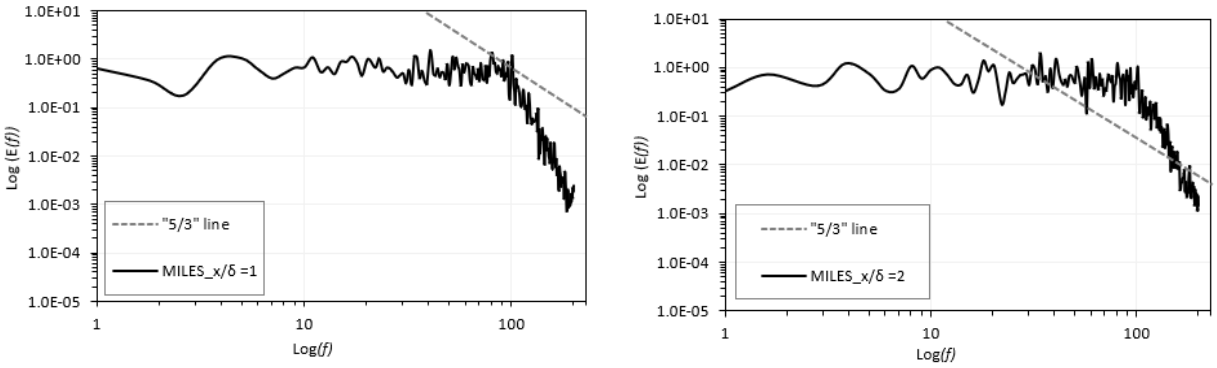

(a) x/δ =1 **(b) x/δ =2**

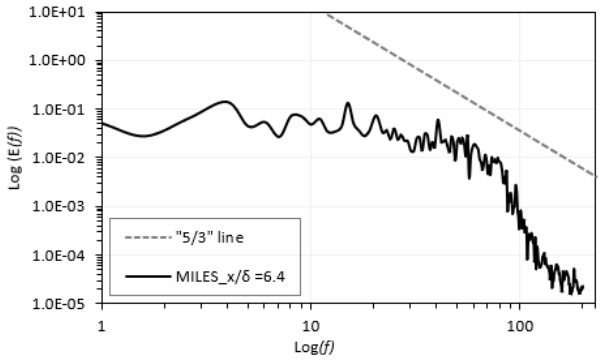

(c) x/δ =6.4

Figure 42. Energy density spectra for forcing simulation of freestream turbulence with $\tau_f/\tau_\infty = 0.045$, using MILES at different streamwise locations corresponding to the middle of the forcing region (a), the downstream edge of the forcing region (b) and the downstream decay region (c).

5.3.4. Effect of Mesh Resolution

Figure 43 shows a comparison of contours of streamwise instantaneous velocity (u_1) for forcing simulations of freestream turbulence with $\tau_f/\tau_\infty = 0.045$ on coarse and refined grids. On both grids, qualitative features of resolved turbulent scales are apparent, but the smallest visible scales are noticeably smaller on the refined grid as expected. As a consequence, the effective dissipation rate is higher on the refined mesh and the stationary values of the normal Reynolds stresses and turbulent kinetic energy are lower than on the coarse mesh. The effect of mesh size on resolved scales is also reflected in the one-dimensional energy spectra shown in Fig. 44. First, it is apparent that regardless of the streamwise location, spectral energy dissipates more rapidly on the refined mesh compared to coarse mesh. Second, the spectrum on coarse grid reflect a shape more indicative of Kolmogorov inertial range scaling. Specifically, at x/δ =1, 2 and 6.4 spectral characteristics of the turbulence generated by the STF method apparently shows that the coarse grid spectrum reflects a shape more indicative of Kolmogorov inertial range scaling. At energy dissipation range for all streamwise locations, evidence of slight energy pile up is apparent on refined grid energy spectra near the highest frequency value, this slightly deviates from the correct spectral behavior. In sum, the total spectral energy is higher on the coarse mesh than on refined mesh at different streamwise locations and the maximum difference in their spectral energy is less than 8% which is relatively negligible.

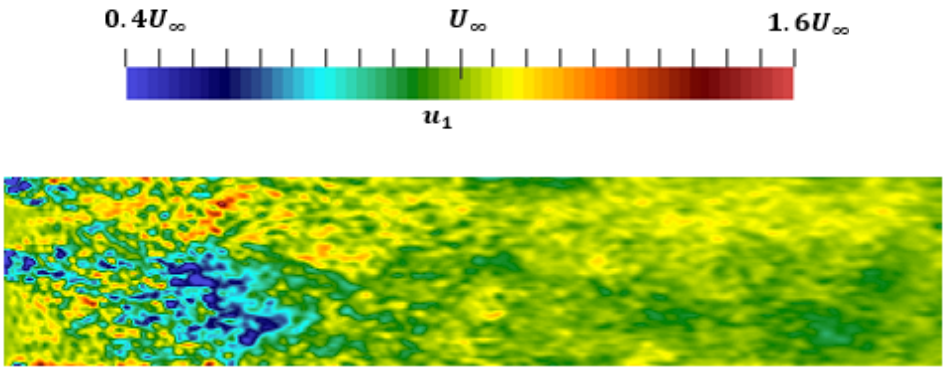

(a) Coarse grid

(b) Refined grid

Figure 43. Contours of streamwise instantaneous (u_1) and mean velocity ($\overline{u}_1$) for forcing simulation of freestream turbulence with $\tau_f/\tau_\infty = 0.045$ using MILES to compute turbulence statistics on (a) coarse, and (b) refined grids.

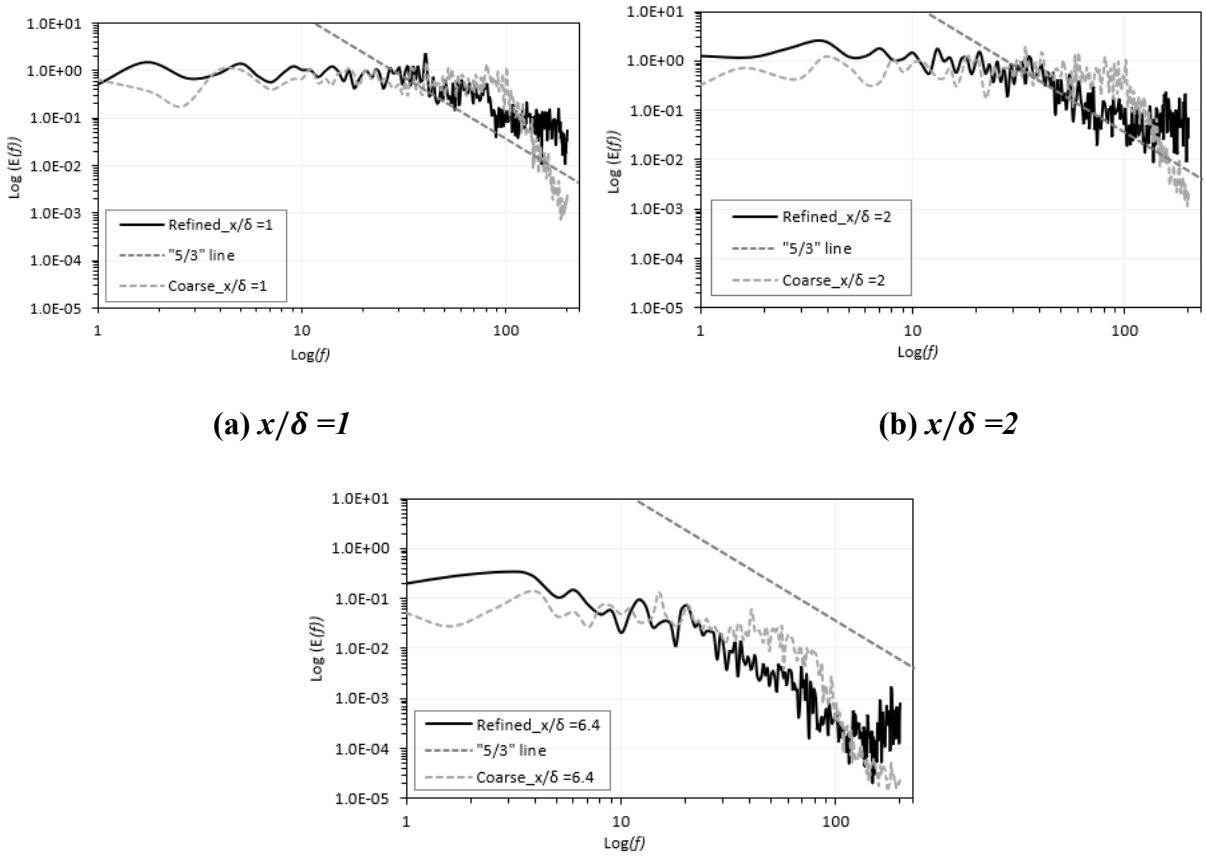

(a) $x/\delta = 1$ **(b)** $x/\delta = 2$

(c) $x/\delta = 6.4$

Figure 44. Energy density spectra for forcing simulation of freestream turbulence with $\tau_f/\tau_\infty = 0.045$, using MILES on both coarse and refined grids at different streamwise locations corresponding to the middle of the forcing region (a), the downstream edge of the forcing region (b) and the downstream decay region (c).

5.3.5 Effect of Forcing Coefficient

Figure 45 shows contours of instantaneous (u_1) velocity for three forcing simulations of freestream turbulence using different values of the forcing coefficient, C_f, such that the effective forcing time scale is $\tau_f/\tau_\infty = 4.5,\ 0.45$, and 0.045, respectively. For the highest value of τ_f, turbulent structures are only apparent as relatively low amplitude streaks, indicating that the strength of the forcing term is not sufficient to produce realistic turbulent flow structures. As the value of C_f is increased, consequently the value of τ_f is reduced and the resolved turbulence level increases, as indicated by the increased value of V_{max}. Similarly, the structure of the fluctuations becomes more indicative of isotropic freestream turbulence. The results suggest that the value of the forcing time scale should be on the order of the length of time required for the mean flow to traverse the forcing region. When the forcing time scale is significantly smaller, the STF forcing method apparently does not have sufficient time to act on the velocity field and produce a realistic turbulent freestream flow.

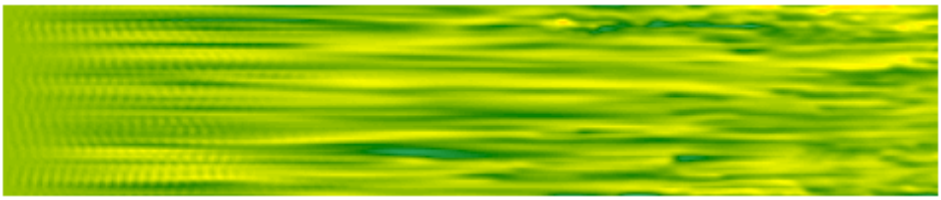

$Vmax = 40.337\ m/s$

(a) $\tau_f/\tau_\infty = 4.5$

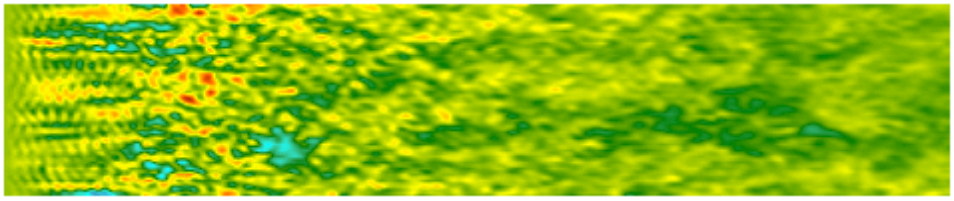

$Vmax = 48.353\ m/s$

(b) $\tau_f/\tau_\infty = 0.45$

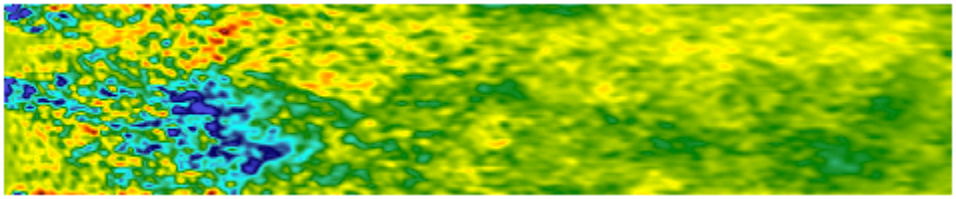

$Vmax = 55.635\ m/s$

(c) $\tau_f/\tau_\infty = 0.045$

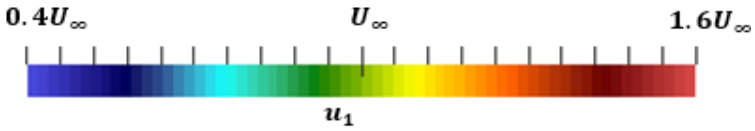

Figure 45. Contours of instantaneous (u_1) and mean velocity ($\bar{u}_1$) for forcing simulation of freestream turbulence using MILES at (a) $\tau_f/\tau_\infty = 4.5$, (b) $\tau_f/\tau_\infty = 0.45$, and (c) $\tau_f/\tau_\infty = 0.045$.

The spatial evolution of the ratio of target-to-resolved turbulent kinetic energy (k/k^*) for forcing simulations with effective forcing time scales of $\tau_f/\tau_\infty = 4.5$, 0.45, and 0.045 are shown in Fig. 46. As the value of τ_f is reduced, the resolved turbulence level more rapidly approaches

the target value, consistent with the results shown in Fig. 45. For the two largest time scales, there is insufficient strength of the forcing term to drive the turbulence statistics close to the target values. As seen for the largest value of $\tau_f/\tau_\infty = 4.5$, the resulting turbulent kinetic energy level in the forcing region is only approximately 5% of the desired level.

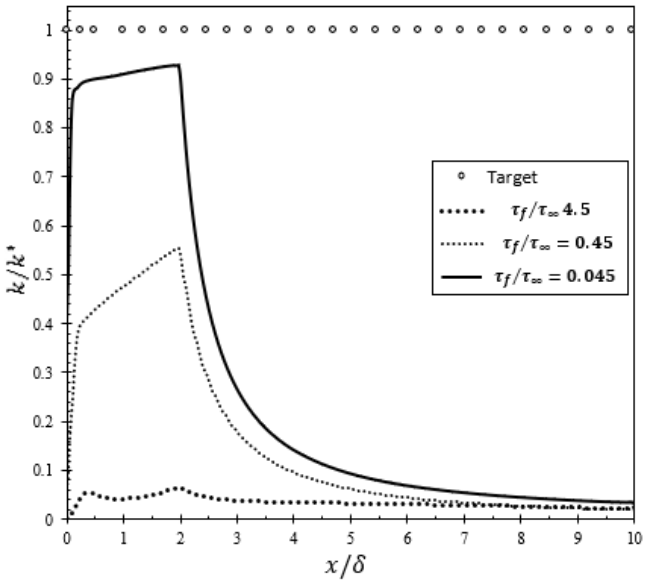

Figure 46. Spatial evolution of normalized turbulent kinetic energy (k/k^*) for forcing simulation of freestream turbulence using MILES at forcing time scales of $\tau_f/\tau_\infty = 4.5$, 0.45, and 0.045.

Figure 47 shows energy spectra for forcing simulations of freestream turbulence at $\tau_f/\tau_\infty = 4.5$, 0.45, and 0.045, at three downstream locations corresponding to x/δ =1, 2, and 6.4. Interestingly, at each location the spectrum shape with highest forcing coefficient which implies the lowest forcing time scale, $\tau_f/\tau_\infty = 0.045$ more closely matches the Kolmogorov inertial subrange represented by the -5/3 law. At x/δ *=1*, the frequency spectra of lower forcing coefficients consequently higher forcing time scales, $\tau_f/\tau_\infty = 0.45$ and 4.5 do not reproduce the correct spectra behavior, indicating that the strength of the forcing term is not sufficient to reproduce realistic Kolmogorov spectral behavior. Farther downstream in the forcing region, at x/δ *=2*, the frequency spectrum of $\tau_f/\tau_\infty = 0.45$ has shifted to reflect a shape more indicative of Kolmogorov inertial range scaling, while that of $\tau_f/\tau_\infty = 4.5$ do not reproduce correct behavior. Downstream of the forcing region at x/δ *=6.4*, energy decay is apparent, and the frequency spectra even more closely approximate the correct shape at lower energy level with the three different values of the forcing coefficient. The key point is that consistent with results shown previously, a higher value for the forcing coefficient produces more accurate results, regardless of the streamwise location in a freestream turbulence.

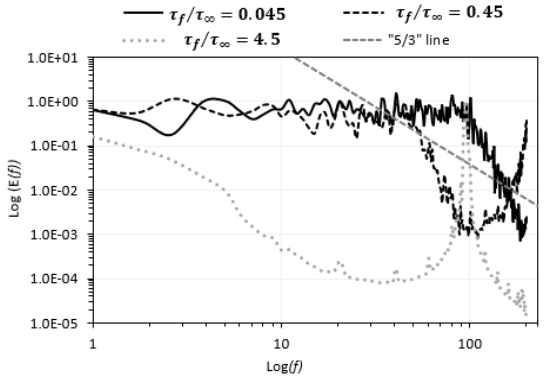

(a) x/δ =1

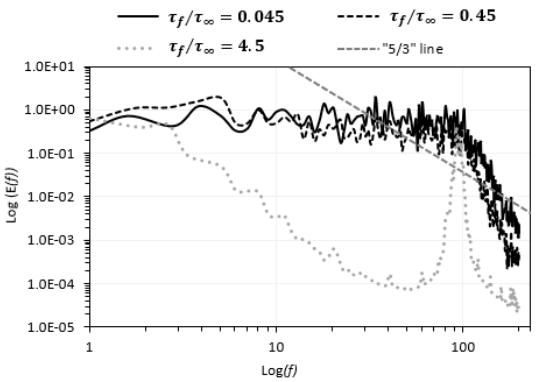

(b) x/δ =2

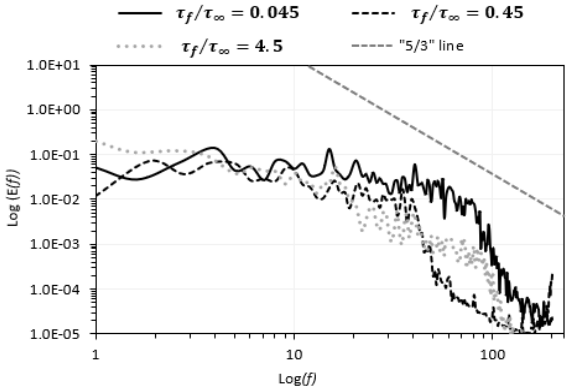

(c) x/δ =6.4

Figure 47. Energy density spectra for forcing simulations of freestream turbulence with three different values of the forcing coefficient using MILES at downstream locations corresponding to the middle of the forcing region (a), the downstream edge of the forcing region (b), and the downstream decay region (c).

5.3.6. Effect of Explicit LES modelling and Spatial filtering

Previously documented results for homogeneous turbulence showed that the subgrid stress model used in the LES had a non-trivial effect on the resulting velocity field when using the STF method [65]. Specifically, use of MILES led to so-called energy pile up in the high wavenumber portion of the energy spectrum, whereas use of the Smagorinsky model provided sufficient dissipation in the small scales to prevent this from occurring. The low wavenumber portion was relatively unaffected. Results in this section compare analogous results from the MILES and Smagorinsky models for the freestream turbulence test case.

Ref. [65] also presented results obtained using spatial filtering, the purpose of which is to allow the control of turbulent length scale in addition to turbulent stress distribution. In that paper an anisotropic filtering method was introduced based on the assumption that energy containing turbulent velocity fluctuations share a nearly equal large-eddy time scale even when length and velocity scales are different for different directions. Briefly, the tensorial filter width is defined to depend on the characteristic turbulent time scale, τ_T, and the target turbulent stress tensor, $\overline{u_j' u_k'}^*$ as shown in Eq. (21). This equation is solved simultaneously with the instantaneous resolved velocity to yield a filtered velocity component, $\hat{u}_i$. The filtered velocity is then used to model the forcing term as shown in Eqs. (15-22). Results using spatial filtering are also presented and discussed in this section.

Recall, Eq. (15) below (*previously shown) is the key anisotropic filtering equation used for this study, where the tensorial filter width, $\phi_{jk} = \tau_T^2 \left(\overline{u_j' u_k'}^*\right)$.

$$\frac{\partial}{\partial x_j}\left(\phi_{jk}\frac{\partial \hat{u}_i}{\partial x_k}\right) = \hat{u}_i - u_i \qquad *(15)$$

Figure 48 shows contours of instantaneous streamwise velocity for forcing simulation of freestream turbulence using two different SGS models, and both with and without spatial filtering. The filter time scale for this case is $\tau_T/\tau_\infty = 4.5$ and the forcing coefficient is $C_f = 100$, which yields a forcing time scale of $\tau_f/\tau_\infty = 0.045$. The fluctuating velocity field is qualitatively similar for all cases with some key differences apparent. First, for both spatially filtered and non-spatially filtered cases, the decay of turbulence downstream of the forcing region is apparently more rapid for the MILES simulation. This is likely due to the increased energy in the small scales which more rapidly extract energy from the larger scales once the turbulent forcing is removed. This difference is evident from Fig. 48 (a), in which the visible scales of turbulence are smaller in the forcing region for MILES versus the Smagorinsky model. Second, observing both MILES and Smagorinsky model results, the scale of resolved turbulence appears to be smaller for the spatially filtered cases. This result is consistent with the homogeneous turbulence results presented in Ref. [65].

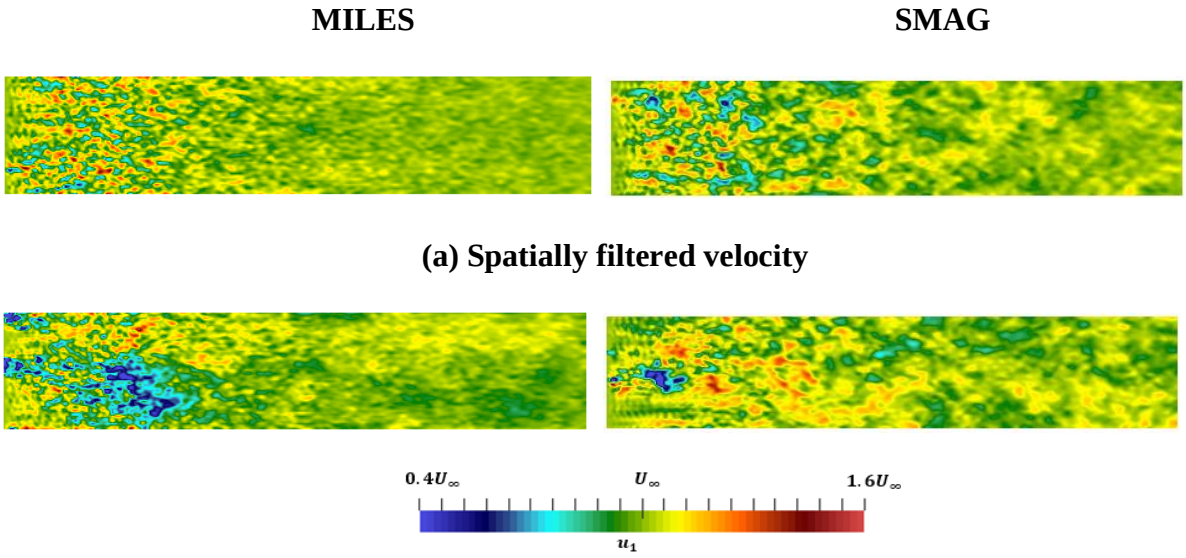

(a) Spatially filtered velocity

(b) Non-spatially filtered velocity

Figure 48. Contours of instantaneous velocity for forcing simulation of freestream turbulence with forcing time scale $\tau_f/\tau_\infty = 0.045$ and two different LES SGS methods: (a) spatially filtered, and (b) non-spatially filtered.

Figure 49. presents the energy spectra for forcing simulations of freestream turbulence for the same conditions shown in Fig. 48. The spectra are presented at streamwise locations corresponding to the middle of the forcing region ($x/\delta = 1$), the outlet of the forcing region ($x/\delta = 2$), and in the downstream decay region ($x/\delta = 6.4$). Differences between the curves are somewhat difficult to distinguish due to the noisy characteristics of the finite time window over the statistics were gathered. Nevertheless, it is apparent that for both spatially filtered and non-spatially filtered results, the energy in the low wavenumber portion of the spectrum is greater for the simulations with the Smagorinsky model versus MILES. This is consistent with the contours shown in Fig. 48. In all other aspects the spectra are similar regardless of SGS model or spatial

filtering, energy decay and a development towards a correct inertial range spectrum as the flow moves downstream.

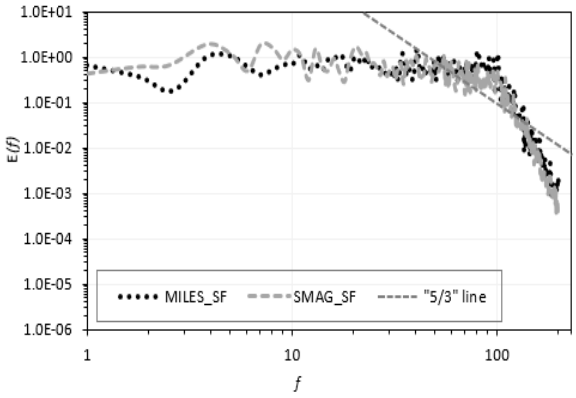

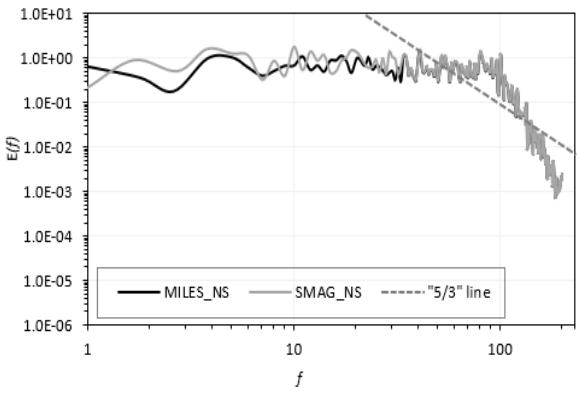

(i)Spatially filtered ***(ii) Non-spatially filtered***

Figure 49(a) x/δ ***=1***

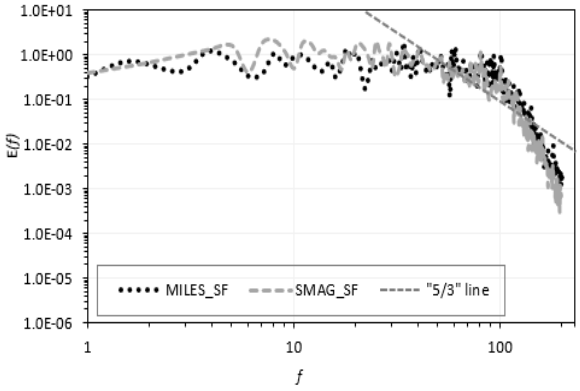

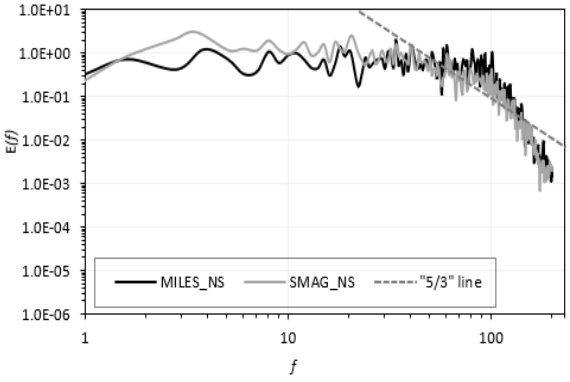

(i)Spatially filtered ***(ii) Non-spatially filtered***

Figure 49*(b)* x/δ ***= 2***

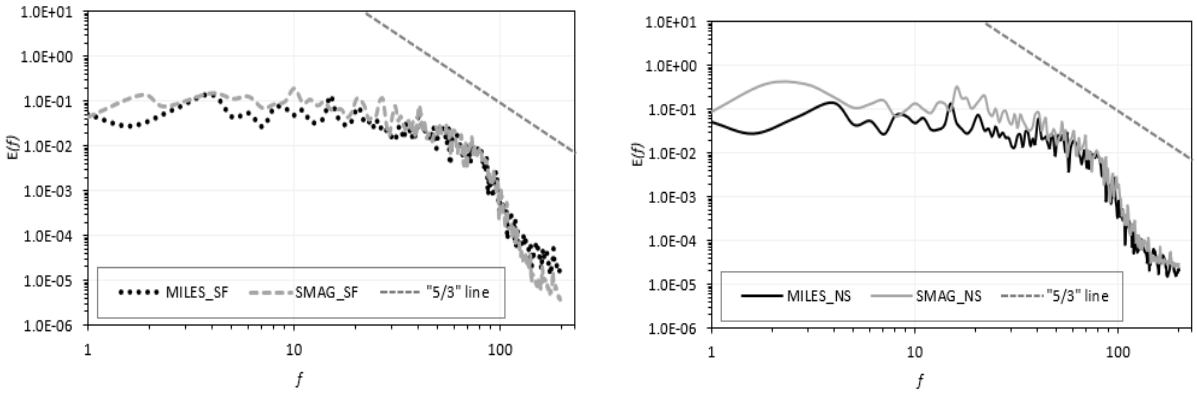

(i)Spatially filtered ***(ii) Non-spatially filtered***

Figure 49(c) x/δ = *6.4*

Figure 49. Energy density spectra for forcing simulation of freestream turbulence with spatially (SF) and non-spatially (NS) filtered velocity using MILES and Smagorinsky models at: (a) x/δ = *1,* (b) x/δ = *2,* and (c) x/δ = *6.4.*

Spatial evolution of normalized turbulent kinetic energy (k/k^*) for simulations matching conditions in Figs. 48 and 49 is shown in Fig. 50. The development of turbulent energy within the forcing region shows differences for all four combinations shown, but the overall energy level at the outlet of the forcing region is within 3% of each other, and within 10% of the target value. The effect of spatial filtering and SGS model is most apparent in the downstream decay region $x/\delta > 2$. The smaller resolved scales of the MILES model result in a more rapid decay compared to Smagorinsky model results, for both spatially filtered and non-spatially filtered simulations. Similarly, regardless of SGS model, spatial filtering results in more rapid energy decay, due to the smaller scale of the resolved turbulent eddies in the forced simulation.

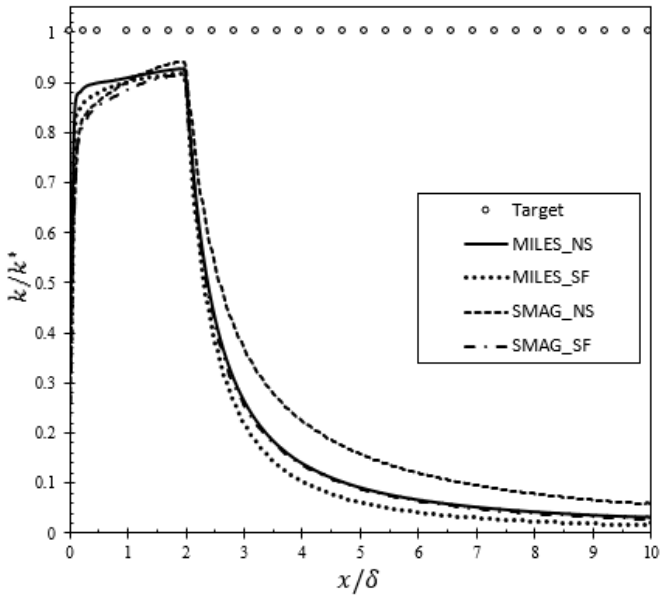

Figure 50. Spatial evolution of normalized turbulent kinetic energy $\left(\frac{k}{k^*}\right)$ for forcing simulation of freestream turbulence with spatially (SF) and non-spatially (NS) filtered velocity using MILES and Smagorinsky models.

5.3.7. Effect of Time-scale Coefficient

The effect of spatial filtering was further investigated by running additional simulations using different filter time scales, corresponding to $\tau_T/\tau_\infty = 1.12, 2.25, \text{and } 4.5$, with MILES as the SGS model and forcing coefficient $C_f = 100$. Figure 51 shows contours of instantaneous streamwise velocity for the three cases. Figures 52 and 53 show the spatial evolution of the resolved turbulent kinetic energy and energy density spectrum at the outlet of the forcing region, respectively. Within the forcing region, as the filter time scale is reduced, the forcing time scale is likewise reduced since C_f is held constant. As a consequence, the turbulence energy level in

the forcing region increases. As τ_T is reduced, the spatial filter width is similarly reduced and the size of the largest resolved turbulent fluctuations decreased. This is apparent in Fig. 52, which shows that the downstream decay rate becomes larger as τ_T becomes smaller. All three of the figures indicate that decreasing the filter time effectively changes the scale of the forced turbulence.

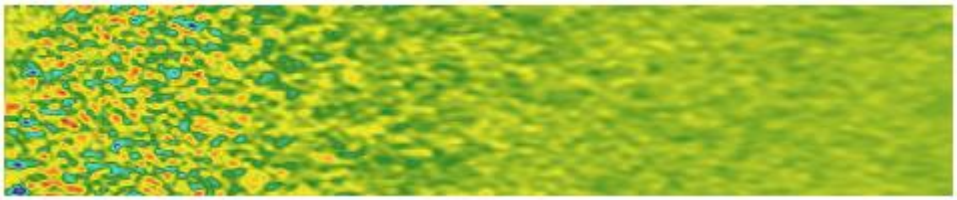

(a) $\tau_T/\tau_\infty = 1.12$

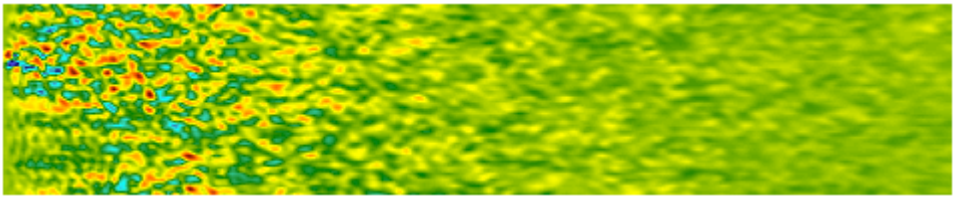

(b) $\tau_T/\tau_\infty = 2.25$

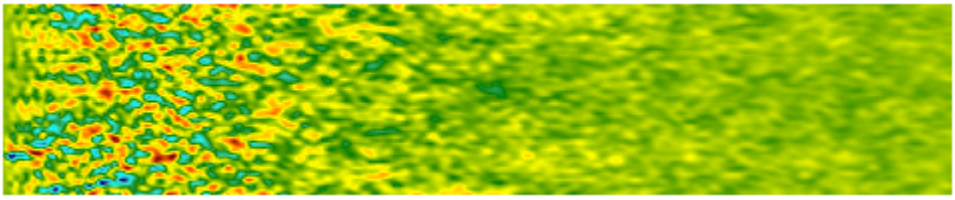

(c) $\tau_T/\tau_\infty = 4.5$

Figure 51. Contours of instantaneous streamwise velocity for forcing simulation of freestream turbulence using MILES, $C_f = 100$, and three different filter time scales: (a) $\tau_T/\tau_\infty = 1.12$, (b) $\tau_T/\tau_\infty = 2.25$, and (c) $\tau_T/\tau_\infty = 4.5$.

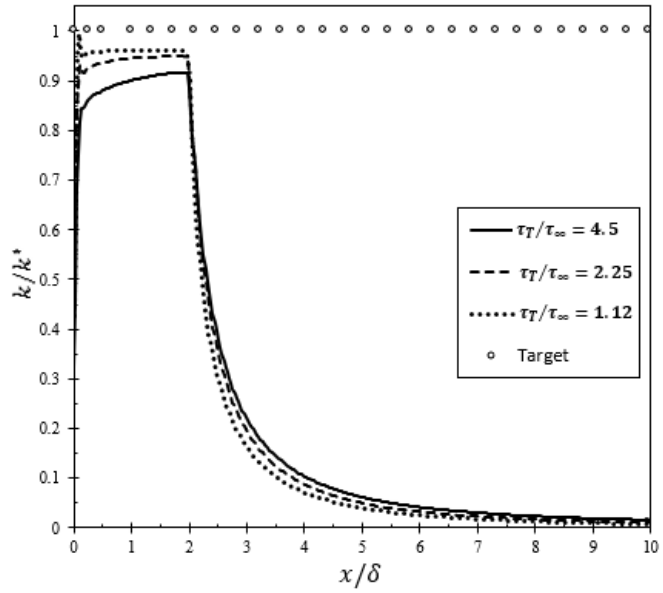

Figure 52. Spatial evolution of normalized turbulent kinetic energy (k/k^*) for forcing simulation of freestream turbulence using MILES, $C_f = 100$, and three different filter time scales.

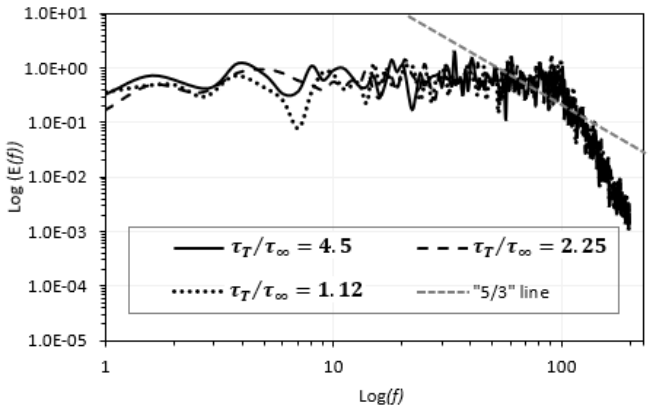

Figure 53. Energy density spectra for forcing simulation of freestream turbulence using MILES, $C_f = 100$, and three different filter time scales.

Table 8 summarizes the results in terms of resolved turbulent kinetic energy level in the STF simulations. The ratio of resolved-to-target energy (k/k^*) is shown for LES (MILES and SMAG) cases at the core and outlet of the forcing region ($x/\delta = 1, 2$), and when energy decay is apparent ($x/\delta = 6.4$) . It is apparent that all of the cases with the smallest investigated forcing time scale ($\tau_f/\tau_\infty = 0.045$) resolve at least 90% of the target energy, while none of the cases with a larger time scale resolved a sufficient amount of energy to be representative of the desired statistics. This is consistent with results in [65]. Overall, the results indicate that the STF method can be used to generate synthetic freestream content for LES simulations provided that appropriate mesh, spatial filtering, and model coefficients are used.

Table 8. Summary of turbulent kinetic energy results for STF cases on coarse grid at x/δ = 1, 2,and 6.4. (Target values are highlighted in yellow. Green color indicates value within 10% of target value at outlet of forcing region.)

				Target Turbulent Kinetic Energy = 75m/s (k^*)		
				Resolved Energy Spectrum (k/k^*)		
FST Cases	***Spatial Filtering***	τ_T/τ_∞	τ_f/τ_∞	x/δ =1	x/δ =2	x/δ =6.4
MILES	No		0.045	0.9078	0.9274	0.0613
MILES	No		0.45	0.4778	0.5532	0.0399
MILES	No		4.5	0.0420	0.0646	0.0303
SMAG	No		0.045	0.9036	0.9423	0.1108
SMAG	Yes	4.5	0.045	0.8879	0.9163	0.0574
MILES	Yes	4.5	0.045	0.9014	0.9155	0.0367
MILES	Yes	2.25	0.045	0.9458	0.9464	0.0283
MILES	Yes	1.12	0.045	0.9604	0.9564	0.0219

5.4. SUMMARY AND CONCLUSION

A relatively new method for synthetic turbulence generation, Statistically Targeted Forcing (STF), method is investigated to reproduce freestream turbulent inflow statistics at Mach number of 0.1 and Re_b of 7000 (based on bulk velocity and half-channel height) in a prototypical channel flow with periodic-walls in wall-normal and spanwise directions only. The method incorporates a source term in the momentum equation to drive the local, instantaneous velocity vector towards a target value. The target value is computed at each instant and location in the simulation based on a mapping of the resolved first- and second-order statistics to the desired, target single-point statistics. Also, three different classes of modeling approach: RANS, LES, and hybrid RANS-LES. Specifically, k-ω SST RANS, MILES, Smagorinsky (SMAG) LES subgrid stress model, and DHRL (resolved and hybrid results) models were investigated. Analysis of the influence of STF method critical parameters, effect of mesh resolution, and effect of choice of modeling frameworks in a freestream turbulent flow were performed. All simulations used time averaging technique to compute mean statistics.

The method was evaluated by performing several test simulations of freestream turbulence, using SST, MILES, SMAG, and DHRL with the FlowPsi finite volume CFD solver, and SSF numerical scheme - a low-dissipation numerics to facilitate resolution of the temporally and spatially varying variable fields in turbulent flow. Qualitative and quantitative comparison of turbulence statistics such as instantaneous and mean velocity, Reynold stress, turbulent kinetic energy, resolved energy spectrum, and effects of mesh sensitivity, forcing coefficients, time-scale coefficients, spatial filtering and explicit LES modelling were compared to target statistics

were presented. Results showed that the method was able to reproduce the inflow freestream turbulence target mean velocity at over 99% accuracy for SST, MILES, and DHRL models. However, for turbulent kinetic energy and Reynold stress, STF method with SST model deviated grossly from target statistics while DHRL and MILES results showed improved performance. The hybrid results of DHRL model reproduced over 66% of target statistics. For the mesh sensitivity analysis, SST is near grid independence while DHRL and MILES are less sensitive to mesh refinement for mean velocity statistics. Effect of forcing coefficient, f_c or effective turbulent time scale, τ_f/τ_∞ on the method was investigated and result were provided which showed that effect of forcing coefficient, f_c on SST model is negligible. For other models considered, as the value of f_c is increased (which implies τ_f/τ_∞ is reduced), the resolved turbulence level more rapidly approaches the target value and energy decay is rapid and apparent with lower values of f_c. Comparison between explicit and implicit LES modeling showed that Smagorinsky (SMAG) explicit subgrid stress LES model evidently showed improved results in comparison to MILES result. Effect of spatial filtering on the method was investigated and the result showed that non-spatially filtered velocity simulation reproduced higher level of accuracy in forcing region, however, in the development region, spatially filtered velocity simulation apparently dissipates more rapidly than the non-spatially filtered cases except for hybrid results of DHRL. The energy spectral analysis showed that STF method is capable of reproducing appropriate spectral content for all models considered with correct inertial range behavior that relatively matches the -5/3 law. Spectral analysis results are in quantitative agreement with physical space results.

In sum, the results indicate that the STF method is capable of reproducing a synthetic freestream turbulence field with prescribed first- and second-order statistics and appropriate spectral content, which can be used to specify initial and/or boundary conditions for LES simulations. The method is relatively simple to implement, non-stochastic, stable, and computationally efficient. The STF method may therefore offer an attractive alternative for synthetic turbulence generation in three-dimensional Navier-Stokes CFD codes and it is relatively applicable to LES and hybrid RANS-LES simulations. Future work will investigate improvement of the method with RANS models by modeling mean flow statistics instead of fluctuating velocity statistics for synthetic generation of turbulent statistics.

CHAPTER VI

STATISTICALLY TARGETED FORCING (STF) METHOD FOR SYNTHETIC TURBULENCE GENERATION OF INITIAL CONDITIONS IN TEMPORALLY-DEVELOPING TURBULENT MIXING LAYER

Work from this chapter was presented at and will be published in the proceedings of the ASME Fluids Engineering Division Summer Conference 2021

6.1 INTRODUCTION

Turbulent free shear flows play an important role in many engineering applications, including external aerodynamics, combustion furnaces, oceanic flows, chemical lasers, internal combustion engines, and gas turbines. The planar mixing layer is an idealization of these types of flows that has been well studied to better understand the key physical features of free shear flows. The majority of studies are of mixing layers that evolve spatially, for example the flow downstream of two fluid streams of different velocity separated by a splitter plate. An alternative is the temporally-developing turbulent mixing layer (TTML), which is statistically homogeneous in two (streamwise and spanwise) directions and includes a mean velocity gradient in the third direction that evolves with respect to time. While some experimental, large eddy simulation (LES), and direct numerical simulation (DNS) studies of TTML are available in the literature, a key outstanding issue for scale-resolving simulations is the specification of appropriate initial conditions. Indeed, methods for cost-effectively reproducing time-dependent turbulence boundary and/or initial (B/I) conditions is of significant potential value for simulation in many engineering applications. In particular, the use of synthetic turbulence generation methods may

reduce computational expense by obviating the need for precursor simulations or recycling/rescaling methods that are often used in spatially-developing flows.

Previous experimental measurements of the statistics of high-Reynolds-number self-similar turbulent mixing layers are available in the literature [1-6]. However, a large variation in experimental results is evident in even the most basic statistical quantities, such as the normalized growth rate (r_w) and the turbulent stress ($\overline{u_i' u_j'}$) distribution. For example, in Liepmann et al. [67] the recorded experimental value of r_w is 0.081, while in Wygnanski et al. [68] it is 0.098. These results suggest that initial conditions play a role even in flows that exhibit nominally self-similar behaviors.

Several direct numerical simulations (DNS) of turbulent mixing layers have been performed. To investigate variations in previous experimental studies, the DNS of Rogers and Moser [73] specifically examined the three-dimensional time-dependent incompressible flow of a temporally evolving mixing layer. They concluded that the self-similarity of the flow is demonstrated by the evolution of the momentum thickness, the evolution of the total dissipation rate of kinetic energy, the collapse of the mean velocity profiles, and the collapse of the Reynolds stress profiles and the vorticity statistics. The values of statistical quantities computed from the simulations were within the range of experimental observations.

More recently, the DNS of Pantano et al. [74] highlighted the effect of different freestream densities in compressible flow and quasi-incompressible flow with a convective Mach number, M_c = 0.3, 0.7, and 1.1. The DNS results were compared with experimental results obtained by Bell and Mehta [71] and Spencer and Jones [69] for incompressible shear layers. For incompressible flow, M_c = 0.3, they documented peak turbulence intensities in the DNS as:

streamwise, $\sqrt{\overline{u'_1 u'_1}}/\Delta u$ = 0.17, vertical, $\sqrt{\overline{u'_2 u'_2}}/\Delta u$ = 0.134, spanwise, $\sqrt{\overline{u'_3 u'_3}}/\Delta u$ = 0.145, and Reynolds shear stress, $\sqrt{\overline{u'_1 u'_2}}/\Delta u$ = 0.103, where Δu is the mean velocity difference between upper and lower fluid streams. The peak intensities and the self-similar profiles of these turbulent statistics agree well with both experiments and the previous DNS by Rogers and Moser [73]. Although previous temporarily evolving mixing layer DNS by Rogers and Moser [73], and Pantano et al. [74] are in good agreement. It has also been previously documented that temporally and spatially evolving mixing layers are qualitatively and quantitatively similar [75].

Methods for boundary/initial (B/I) conditions in scale-resolving turbulent flow simulations range from library-based methods to recycling/rescaling to synthetic turbulence generation (STG) with controlled forcing methods. The goal of B/I condition methods such as synthetic turbulence generation (STG) is to replace turbulent content obtained from fully resolved simulations with a reasonable approximation of turbulence for a substantially lower computational cost. Additionally, with STG methods, turbulent content can be selectively prescribed in specific regions of the computational domain or on the boundaries, providing flexibility such that turbulence B/I conditions are only used in regions where they are needed.

For recycling/rescaling methods, turbulent content is recycled by imposing streamwise periodic boundary conditions on a portion of the domain such that the turbulent flow leaving the outlet is reintroduced at the inlet. As an example, Spalart and Watmuff [16] used this method to perform large-eddy simulation of a turbulent boundary layer. Rescaling of the velocity field can be performed to ensure that the turbulent statistics remain appropriately spatially developing. Lund et al. [17] used the recycling/rescaling method to perform an auxiliary simulation of a

turbulent boundary layer, then extracted planes of time-dependent velocity data to be mapped to the inlet of a simulation with a more complex geometry. Several other studies have extended the recycling/rescaling approach to simulate complex wall bounded flows [18-20]. Schlüter et al. [21] used the recycling/rescaling method to impose fluctuating velocities at the outlet to an LES region of a simulation to impose the statistics obtained from a Reynolds-averaged Navier-Stokes (RANS) solution in the downstream region.

For applications of more practical engineering interest on complex geometries, STG methods are a suitable alternative to recycling/rescaling methods. They have the potential to reproduce turbulent fluctuations at desired locations and with desired statistical distributions, without the need to run a full auxiliary simulation. STG methods can be used to specify inflow boundary conditions or as initial conditions for a simulation. For example, for isotropic turbulence, a spectral approach can be used to artificially produce an isotropic turbulent velocity field from random Fourier modes [22-24]. Other researchers have highlighted different STG methods and their formulations [51-57]. For example, Lundgren [52] defined a forcing term in the momentum equations that is proportional to the fluctuating velocity component. This isotropic linear forcing (ILF) term imitates the natural production mechanism in the turbulent kinetic energy equation, which is restricted to low wavenumber modes when a spectral approach is used. Rosales et al. [53] extended this method by formulating the forcing term in physical space.

De Laage de Meux et al. [58] proposed a method to impose target statistics of the flow in terms of mean velocity and resolved turbulent stress, using a method denoted anisotropic linear forcing (ALF). The time-dependent forcing function is proportional to the instantaneous velocity via a tensor transformation. The method was found to provide accurate results for isotropic,

anisotropic, and spatially developing turbulence test cases for LES and hybrid RANS-LES simulations. More recently, Shobayo and Walters [27] validated a proposed Statistically Targeted Forcing (STF) method for homogeneous isotropic and anisotropic turbulent flow, where results showed that the method can accurately match the desired target statistics.

The objective of this study is to evaluate the performance of the newly proposed STF method to capture the vortex dynamics of the temporally-evolving turbulent mixing layer and effectively match target mean velocity and resolved turbulent stress predictions for a large-eddy simulation. The STF method is a variant of STG with controlled forcing within the simulation domain, implemented via added source terms in the momentum and energy equations. The method can be viewed to act as a time-dependent restoring force to enforce a target statistical state within a time-averaging framework. Simulation results are presented for a temporally-developing turbulent mixing layer (TTML) and results are compared to target statistical velocity and turbulent stress distributions obtained from DNS simulations of Pantano et al [74] and interrogated to evaluate the effect of different aspects of the forcing method and simulation details.

6.2. STATISTICALLY TARGETED FORCING (STF) METHOD FORMULATION

6.2.1. General Description of the Method

This section briefly reviews the statistically targeted forcing (STF) method. The STF method seeks to induce a synthetic turbulence field through the addition of a time-dependent, non-stochastic forcing term in the momentum equation. The forcing term is constructed to drive the instantaneous, local velocity towards a "target" velocity that satisfies the user-specified first-

and second-order one-point statistics for the turbulence, i.e., the mean velocity vector and Reynolds stress tensor. To introduce the method, we consider the general form of the continuity, momentum, and energy equations for single-phase, single-species, compressible flow:

$$\frac{\partial \rho}{\partial t} + \frac{\partial}{\partial \mathrm{x_j}}\left(\rho u_j\right) = 0 \tag{1}$$

$$\frac{\partial}{\partial t}\left(\rho u_i\right) + \frac{\partial}{\partial \mathrm{x_j}}\left(\rho u_i u_j\right) = -\frac{\partial p}{\partial \mathrm{x}_i} + \frac{\partial}{\partial \mathrm{x_j}}\left(\sigma_{ij}\right) \tag{2}$$

$$\frac{\partial}{\partial t}\left(\rho E\right) + \frac{\partial}{\partial \mathrm{x_j}}\left(\rho u_j H\right) = \frac{\partial}{\partial \mathrm{x_j}}\left(q_j + u_i \sigma_{ij}\right) \tag{3}$$

In the above, the flow variables ρ, u, p, E, and H may represent local instantaneous (DNS) or filtered (LES) quantities. Likewise, the viscous stress tensor σ_{ij} and heat flux vector q_j include both molecular and, for LES, subfilter contributions.

The STF method is implemented by adding a forcing term, fi, to the momentum and energy equations:

$$\frac{\partial}{\partial t}\left(\rho u_i\right) + \frac{\partial}{\partial x_j}\left(\rho u_i u_j\right) = -\frac{\partial p}{\partial x_i} + \frac{\partial}{\partial x_j}\left(\sigma_{ij}\right) + f_i \tag{4}$$

$$\frac{\partial}{\partial t}(\rho E) + \frac{\partial}{\partial x_j}\left(\rho u_j H\right) = \frac{\partial}{\partial x_j}\left(q_j + u_i \sigma_{ij}\right) + u_i f_i \tag{5}$$

The source term is constructed such that during each time step of a simulation, the resolved velocity vector is forced toward a target velocity vector that would in principle yield a desired target statistical distribution for the time-varying velocity field. The general form of the forcing term is:

$$f_i = \frac{\rho}{\tau_f}(u_i^* - u_i) \tag{6}$$

Here u_i^* is a target local, instantaneous velocity and τ_f and is a characteristic time scale for the forcing term. Inputs to the model include prescription of a local target mean velocity, $\bar{u}_i^*$, and turbulent stress tensor, $\overline{u_i' u_j'}^*$:

$$\overline{u_i' u_j'}^* = \left(\overline{u_i u_j} - \bar{u}_i \bar{u}_j\right)^* \tag{7}$$

where the overbar denotes either Reynolds or Favre (mass-weighted) averaging.

The key aspect of the forcing method is the calculation of the target velocity vector u_i^*. It is first noted that the transformation proposed by Lund et al. [17] can be used to map an ensemble

of isotropic velocity fluctuations v' to an ensemble of fluctuations that satisfy a target statistical distribution $T_{ij} = \overline{u_i' u_j'}^*$ as follows:

$$u_i'^* = B_{ij} v_j' \tag{8}$$

$$B_{ij} = \begin{bmatrix} \sqrt{T_{11}} & 0 & 0 \\ T_{21}/B_{11} & \sqrt{T_{22} - B_{21}^2} & 0 \\ T_{31}/B_{11} & (T_{32} - B_{21}B_{31})/B_{22} & \sqrt{T_{33} - B_{31}^2 - B_{32}^2} \end{bmatrix} \tag{9}$$

Similarly, an ensemble of resolved fluctuations satisfying a particular statistical distribution $R_{ij} = \overline{u_i' u_j'}$ can be mapped to an isotropic distribution v' using the inverse of the Lund coefficient matrix:

$$v_i' = A_{ij}^{-1} u_j' \tag{10}$$

$$A_{ij}^{-1} = \begin{bmatrix} 1/A_{11} & 0 & 0 \\ -A_{21}/(A_{11}A_{22}) & 1/A_{22} & 0 \\ (A_{21}A_{32} - A_{31}A_{22})/(A_{11}A_{22}A_{33}) & -A_{32}/(A_{22}A_{33}) & 1/A_{33} \end{bmatrix} \tag{11}$$

$$A_{ij} = \begin{bmatrix} \sqrt{R_{11}} & 0 & 0 \\ R_{21}/A_{11} & \sqrt{R_{22} - A_{21}^2} & 0 \\ R_{31}/A_{11} & (R_{32} - A_{21}A_{31})/A_{22} & \sqrt{R_{33} - A_{31}^2 - A_{32}^2} \end{bmatrix} \quad (12)$$

It is therefore possible to define a mapping from a distribution of resolved velocity fluctuations u_i' with known statistical second moment tensor (turbulent stress) R_{ij} to a distribution $u_i'^*$ with target turbulent stress T_{ij} as:

$$u_i'^* = C_{ij} u_j' \quad (13)$$

$$C_{ij} = B_{ik} A_{kj}^{-1} \quad (14)$$

The instantaneous target velocity used in the forcing function includes the target fluctuating velocity as well as the target mean velocity:

$$u_i^* = \bar{u}_i^* + C_{ij} u_j' \quad (15)$$

where the fluctuating velocity is defined relative to the mean:

$$u_i' = u_i - \bar{u}_i \tag{16}$$

In practice the method is implemented as follows. First a target statistical velocity distribution is specified prior to the simulation in terms of $\bar{u}_i^*$ and $\overline{u_i' u_j'}^*$. As the simulation proceeds, the resolved statistics $\bar{u}_i$ and $\overline{u_i' u_j'}$ are obtained using an appropriate averaging technique. At each time step, the transformation tensor C_{ij} is computed at each point in the domain based on $\overline{u_i' u_j'}^*$ and $\overline{u_i' u_j'}$. During each iteration, the fluctuating velocity u_i' is computed, and the target instantaneous velocity u_i^* is found using Eq. (15). The forcing term f_i is then computed using Eq. (6) and included as an additional source term in the momentum and energy equations.

6.2.2. Prescription of the Forcing Time Scale

The forcing time scale τ_f in Eq. (6) is arbitrary. In principle, a smaller value will cause a more rapid transition toward the target statistical velocity field, but too small a value may result in instability or may constrain the flow from developing naturally once resolved turbulence has been introduced. In practice, a user can select a relevant time scale based on the known flow physics of the problem under investigation, numerical and stability considerations, and/or trial and error. It would be advantageous, however, to incorporate a universal time scale that considers both the physical and numerical aspects of the simulation and simplifies the user input requirements. It is proposed, therefore, that an appropriate time scale is of the form:

$$\tau_f \sim \tau_T \tag{17}$$

where τ_T is the characteristic large-eddy turbulent time scale. Depending on the type of simulation performed, the turbulent time scale can be approximated by a characteristic imposed length scale, or from the source of the target statistical distribution. For example, if a precursor Reynolds-averaged Navier-Stokes simulation is used to specify the target mean velocity and Reynolds stress tensor, the dissipation time scale k/ε can be used to specify τ_f. The form of the forcing term becomes:

$$f_i = \rho \frac{C_f}{\tau_T}(u_i^* - u_i) \tag{18}$$

and the coefficient C_f is a user-specified constant that dictates the overall strength of the forcing term. For the current simulations, an arbitrary global turbulent time scale of $\tau_T = 0.002\delta_{m,0}/\Delta u$ is used for all simulations, and the effective forcing time scale is varied by selecting different values of C_f.

6.2.3. Ensemble Averaging

To approximate the Reynolds-averaging operation used in the prescription of the forcing term, time-averaging is used, where the averaged quantity is defined as:

$$\bar{\varphi}(x_i, t) = \frac{1}{t}\int_0^t \varphi(x_i, \tau)\, d\tau \tag{19}$$

Here t is the physical simulation time. In practice this is achieved using a discrete running time average, for which the averaged value at each point in the domain can be determined by:

$$\bar{\varphi}(x_i, t) = \frac{n-1}{n}\bar{\varphi}(x_i, t - \Delta t) + \frac{1}{n}\varphi(x_i, t) \tag{20}$$

where Δt is the time-step size and n is the current number of time steps in the simulation. In the limit $n \to \infty$, the averaged value becomes constant for statistically stationary flow.

For the cases in the current study, the initial part of the simulation is for a turbulence field that is statistically "frozen", and so may be modeled as a stationary flow, and running time averaging used to represent the Reynolds average. Once the simulation has reproduced an appropriate initial condition, the forcing can be removed, and the flow allowed to evolve temporally as the mixing layer grows from the initial state.

6.3. SIMULATION DETAILS

All simulations in this study used the STF method with the Smagorinsky (SMAG) eddy-viscosity based subgrid stress model [61] or implicit monotonically-integrated LES (MILES) [62]**.** The deviatoric part of the subgrid stress tensor for SMAG is expressed as:

$$\tau_{ij}^{SGS} = 2\nu_T S_{ij} \tag{21}$$

and the eddy viscosity is formulated as:

$$\nu_T = (C_s \Delta)^2 \sqrt{2S_{ij}S_{ij}} \tag{22}$$

where S_{ij} is the resolved rate-of-strain tensor, Δ is the characteristic mesh size, equal to the cube root of cell volume in the current simulations, and the coefficient C_s = 0.1. The subgrid stress term $\tau_{ij}^{SGS} = 0$ for MILES but is implicitly implemented using nonlinear high-frequency filters of high-resolution upwind algorithms for the convective terms. The MILES test case is included to investigate effect of implicit and explicit LES modeling on STF method.

6.3.1. Computational Fluid Dynamics Solver

All simulations in this study were performed using the open source CFD code flowPsi [59], a finite-volume density-based solver constructed in C++ using the Loci framework. FlowPsi uses high-resolution approximate Riemann solvers and implicit numerical methods. For the present study, all simulations were run with sufficiently low Mach number to simulate incompressible flow conditions. Inviscid fluxes are reconstructed using a modified skew symmetric flux (SSF) scheme. The SSF scheme is a generalization of the kinetic energy consistent (KEC) central difference scheme of Subbareddy and Candler [60], blended with a small second-order upwind

flux contribution. For all simulations in this paper, the blending distribution was 95% central difference and 5% upwind. The SSF scheme has been shown to provide low numerical dissipation and effective resolution of high wavenumber velocity and pressure modes in unsteady turbulent flow simulations.

6.3.2. Temporally-Developing TML Test Case

The domain represents a hexahedral box that is statistically homogeneous in the streamwise (x) and spanwise (z) directions but non-periodic in the normal (y) direction to capture the turbulence dynamics. The domain is shown in Fig. 58. The domain dimensions are $39.6\delta_{m,0} \times 19.8\delta_{m,0} \times 19.8\delta_{m,0}$, where $\delta_{m,0}$ is the initial momentum thickness of the mixing layer. The boundaries in the normal (vertical) direction have a zero-flux symmetry boundary condition while the streamwise and spanwise boundaries are periodic. Flow was initialized for all cases with a hyperbolic tangent velocity profile for the mean streamwise velocity while all other velocity components were set to zero. Additionally, three dimensional random perturbations of 10% turbulent intensity were imposed. The upper-stream mean velocity is $U_l = -1/2\,\Delta u$, and the lower-stream mean velocity is $U_h = 1/2\,\Delta u$, where Δu is the velocity difference between the two fluid streams. Target velocity distributions were selected such that the Mach number based on maximum instantaneous velocity was approximately 0.3, which approximates incompressible flow conditions. For the thermodynamic state of the fluid, the same constant density was imposed for the higher and lower free-stream velocities, the flow was isothermal, and the top and bottom boundary conditions were adiabatic. Hence density ratio $s = \rho_h/\rho_l = \rho_1/\rho_2$ is 1. The mean pressure was set to a uniform value, $p_0 = 101000$ Pa, temperature was initialized to 293K, and the Prandtl number of air was 0.71.

The momentum and vorticity thickness (δ_m and δ_w) of the mixing layer are defined as :

$$\delta_m = \frac{1}{\rho \Delta u^2} \int_{-\infty}^{\infty} \rho(\frac{1}{2}\Delta u - \widetilde{u_1})(\frac{1}{2}\Delta u + \widetilde{u_1})\, dy \tag{23}$$

$$\delta_w = \Delta u / \langle \frac{\partial u_1}{\partial y} \rangle_{max} \tag{24}$$

where $\widetilde{u_1}$ and $\langle \frac{\partial u_1}{\partial y} \rangle$ represent planar-averaged streamwise velocity and velocity gradient respectively. The initial values of momentum and vorticity thickness are denoted as $\delta_{m,0}$ and $\delta_{w,0}$, respectively. The initial Reynolds number, Re_λ, based on the Taylor microscale, λ, is:

$$Re_\lambda = \langle v' \rangle_{RMS} \lambda / \nu \tag{25}$$

$$\langle v' \rangle_{RMS} = (\overline{u_i' u_i'}/3)^{0.5} \tag{26}$$

where $\langle v' \rangle_{RMS}$ is the root mean square (RMS) velocity magnitude. The momentum thickness Reynolds number, Re_m, based on Δu and $\delta_{m,0}$ is 134, and the vorticity Reynolds number, Re_w, based on Δu and $\delta_{w,0}$ is 638. The initial vorticity thickness $\delta_{w,0} \approx 4.75\, \delta_{m,0}$, which is consistent with the DNS simulation parameters in [74]. The convective Mach number, M_c is 0.3 and defined as $M_c = \frac{\Delta u}{c}$, where c is the speed of sound in air.

Pointwise and Ansys meshing software were used to generate two structured single-block computational grids, in order to evaluate the effect of mesh resolution on the STF method. The coarse and refined grids are about 131,072 and 1.049 million cells respectively. The number of grid cells for both grids are $N_x \times N_y \times N_z$, that is $64 \times 64 \times 32$ for coarse grid, and $128 \times 128 \times 64$ for refined grid, where N_x, N_y, and N_z denotes the number of grid points uniformly distributed in the streamwise, normal, and spanwise directions, respectively. The meshes are illustrated in Fig. 59. Recently, Shobayo and Walters [65] documented that the STF method is relatively mesh insensitive for homogeneous turbulence. In this study we seek to investigate the sensitivity of STF method to mesh resolution particularly in a temporally-developing turbulent mixing layer (TTML) for which the mean velocity gradient is non-zero.

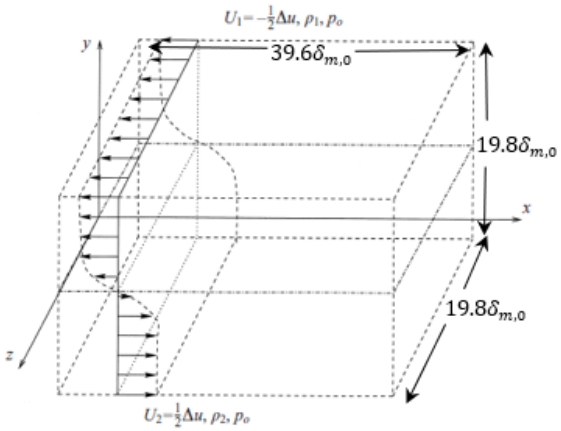

Fig. 54. Computational domain for the temporally-developing turbulent mixing layer (TTML) [8].

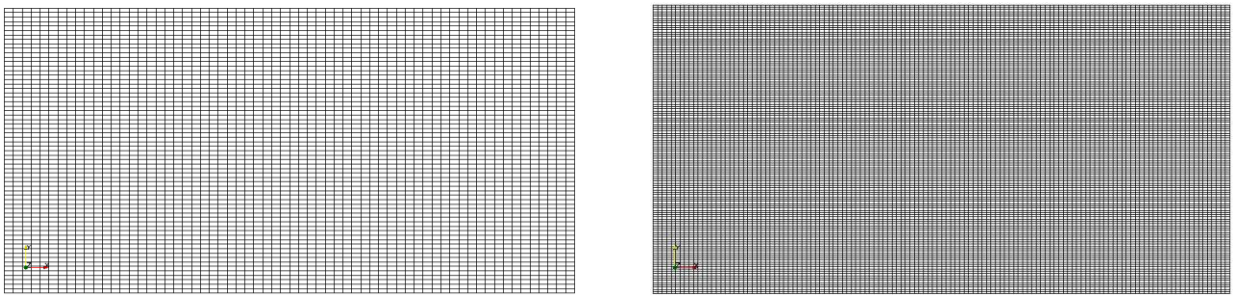

(a) Coarse grid ($64 \times 64 \times 32$ cells) **(b) Refined grid ($128 \times 128 \times 64$ cells)**

Fig. 55. Front view of the computational grids used for TTML simulations: (a) coarse, and (b) refined.

6.4. RESULTS AND DISCUSSION

For all simulations in this study, the forcing terms shown in Eqs. (4,5) are applied throughout the entire domain. The target statistics used in the STF method were defined as mean velocity and Reynolds stress profiles in the vertical direction, and approximately matched the self-similar velocity profiles obtained from DNS in [74]:

$$\Delta u = 100 \frac{m}{s} \tag{27}$$

$$\overline{u_1' u_1'}^{*} = \Delta u^2 (0.16 e^{-2y^2})^2 \tag{28}$$

$$\overline{u_2'u_2'}^* = \Delta u^2(0.135e^{-2.2y^2})^2 \quad (29)$$

$$\overline{u_3'u_3'}^* = \Delta u^2(0.145e^{-3.5y^2})^2 \quad (30)$$

$$\overline{u_1'u_2'}^* = \Delta u^2(0.105e^{-2.8y^2})^2 \quad (31)$$

$$\bar{u}_1(y) = \frac{\Delta u}{2}\tanh\left(\frac{-y}{2\delta_{m,0}}\right), \bar{u}_2 = \bar{u}_3 = 0. \quad (32)$$

Note that throughout the paper ϕ^* and ϕ^{**} denote target and peak target statistics, respectively. Hence, the peak target turbulent kinetic energy is equal to $k^{**} = 323.84\frac{m^2}{s^2}$, and the peak characteristic fluctuating velocity scale for the target flowfield is $u_1{}' = 16\frac{m}{s}, u_2{}' = 13.5\frac{m}{s}$, and $u_3{}' = 14.5\frac{m}{s}$. The average peak characteristic fluctuating velocity is $v' = 14.7\frac{m}{s}$. Initial or baseline simulations employing the STF model were run using time averaging for turbulence statistics, time-scale parameter values of $\tau_T = 1E-06\,s$ and $C_f = 1$, and the Smagorinsky subgrid stress model. Additional cases were run to investigate effects of mesh sensitivity, forcing coefficient, and implicit LES modeling.

Results from all cases are summarized in Table 9 in terms of peak values of the non-zero Reynolds stress components. All of the model combinations yielded a maximum error of less than about 15%. In general, as the strength of the forcing term was increased, the agreement with target statistics and DNS data improved. The results showed little sensitivity to mesh refinement level or subgrid stress model. The remainder of this section will examine the results in more detail.

Table 9. Summary of target peak turbulence statistics for temporally-developing turbulent mixing layer (green color indicates difference of less than 6% compared to DNS target statistics)

				Peak Target Turbulence Statistics			
				$\overline{u_1'u_1'}^{+*0.5}/\Delta u$	$\overline{u_2'u_2'}^{+*0.5}/\Delta u$	$\overline{u_3'u_3'}^{+*0.5}/\Delta u$	$\overline{u_1'u_2'}^{+*0.5}/\Delta u$
			*Target	0.1700	0.1350	0.1450	0.1050
		** Peak Target value		Peak Resolved-to-Target Turbulence Statistics			
Model	τ_s	C_f	**Grid**	$\overline{u_1'u_1'}^{0.5}/\overline{u_1'u_1'}^{+*0.5}$	$\overline{u_2'u_2'}^{0.5}/\overline{u_2'u_2'}^{+*0.5}$	$\overline{u_3'u_3'}^{0.5}/\overline{u_3'u_3'}^{+*0.5}$	$\overline{u_1'u_2'}^{0.5}/\overline{u_1'u_2'}^{+*0.5}$	**Max % Relative Error**
SMAG	2040	0.1	Coarse	1.1529	0.8556	0.9359	1.0933	15.29%
SMAG	2040	0.1	Refined	1.0959	0.8556	0.9917	1.0629	9.59%
SMAG	2040	1	Refined	0.9482	0.9644	0.9952	1.0029	0.29%
SMAG	2040	1	Refined	0.9553	0.9556	0.9903	1.0076	0.76%
SMAG	2040	1	Refined	0.9776	0.9200	0.9855	1.0267	2.67%
SMAG	2040	1	Coarse	0.9659	0.9481	0.9690	1.0257	2.57%
SMAG	2040	1	Refined	1.0100	0.8904	0.9676	1.0524	5.24%
MILES	2040	1	Refined	1.0141	0.8985	0.9821	1.0590	5.90%
SMAG	2040	10	Coarse	0.9471	0.9696	0.9903	1.0029	0.29%
SMAG	2040	10	Refined	0.9453	0.9748	0.9897	1.0019	0.19%
SMAG	1140	1	Refined	0.9671	0.8941	1.0034	0.9743	0.34%
SMAG	1480	1	Refined	0.9671	0.8459	0.9207	0.9438	3.29%
SMAG	1700	1	Refined	1.0135	0.8963	0.9724	1.0581	5.81%
SMAG	2400	1	Refined	1.0071	0.9015	0.9697	1.0524	5.24%
SMAG	2520	1	Refined	1.0041	0.9081	0.9759	1.0533	5.33%
SMAG	2800	1	Refined	1.0059	0.9037	0.9772	1.0543	5.43%
SMAG	3020	1	Refined	1.0035	0.9007	0.9738	1.0438	4.38%
SMAG	3400	1	Refined	1.0594	0.8437	0.9131	0.9752	5.94%

6.4.1. Instantaneous and Mean Velocity

Figure 60 shows contours of instantaneous and mean velocity, highlighting the qualitative features of the upper (U_l) and lower (U_h) streams at different dimensionless simulation times, τ_s. Here $\tau_s = t\Delta u/\delta_{m,0}$ is normalized by initial momentum thickness $\delta_{m,0}$, and velocity difference Δu. Figure 60 shows the spatial variation in mean velocity indicative of fluctuating, apparently turbulent behavior. It is also apparent that the mean velocity reaches a state that indicates a clearly defined mean shear layer by $\tau_s = 1140$, and that the mean velocity remains relatively unchanged beyond that time.

Figure 61 shows contours of streamwise instantaneous velocity (u_1) with forcing term values of $C_f = 1$ and $\tau_T = 1\text{E} - 06\ s$ at different simulation times τ_s. An increase in resolution of velocity scales in the simulation are more evident at higher values of τ_s. Figs. 61 (b, c, and d) are qualitatively similar in showing features of resolved streamwise instantaneous velocity.

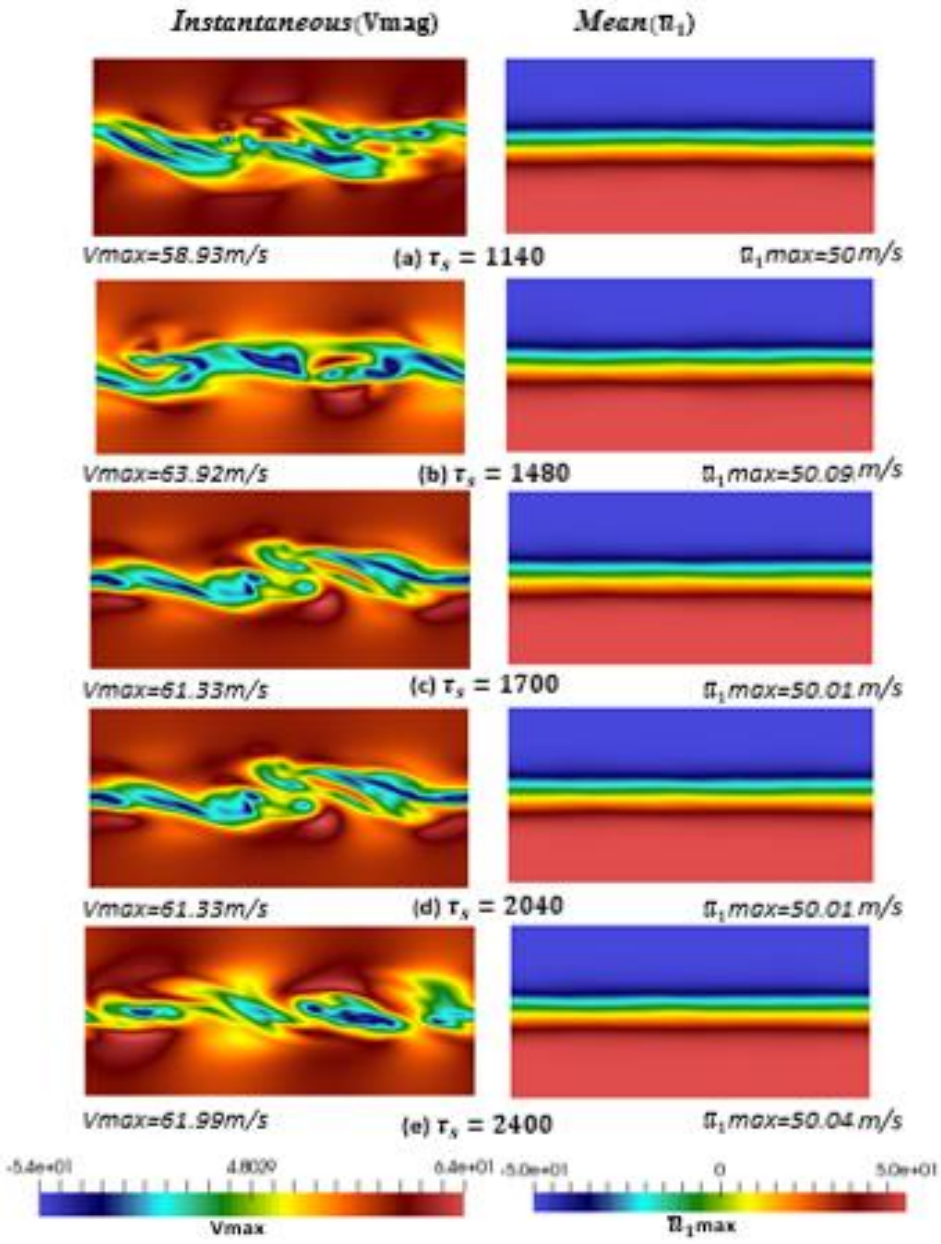

Fig. 56. Contours of instantaneous velocity magnitude with maximum value (Vmax) indicated, and streamwise mean velocity ($\bar{u}_1$) for forcing simulation of TTML for $C_f = 1, \tau_s = 1140$, 1480, 1700, 2040, 2400 on refined grid.

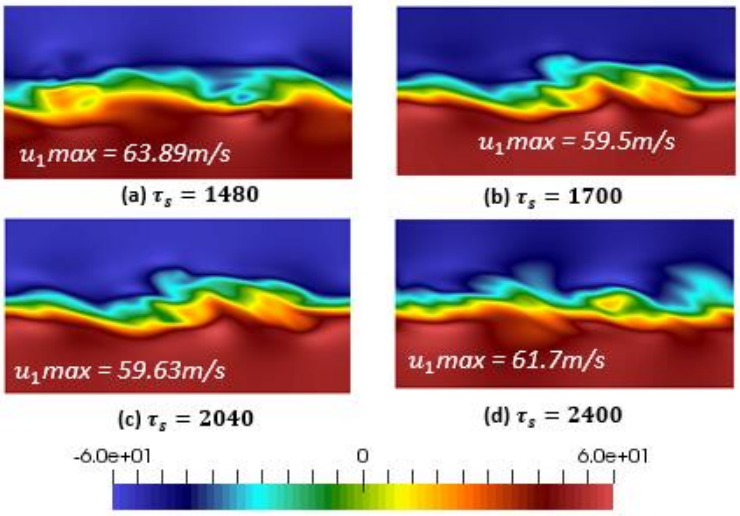

Fig. 57. Contours of streamwise instantaneous velocity (u_1) for forcing simulation of temporally-developing turbulent mixing layer at $C_f = 1$, τ_s = 1480, 1700, 2040, 2400.

Figure 58 illustrates the temporal evolution of the mean streamwise velocity profile of the TTML for $C_f = 1, \tau_T = 1E-06\ s$. The result shows that all profiles qualitatively agree with the DNS data profile [74] in the region $-1 \leq y/\delta_w \leq 1$. The maximum relative integral error over the entire velocity profile is less than 1%, which implies that all profiles have statistically converged. Overall, all profiles are in quantitative agreement with DNS [73,74] and experimental data [69,71,73]. It is apparent that the STF method closely matches the DNS target statistics at $1700 \leq \tau_s \leq 2520$ in comparison to the self-similar state of Rogers and Moser [73] DNS result at $105 < \tau_s < 150$, and that of Pantano and Sarkar [74] at $261 < \tau_s < 518$. This comparison is not exact, since the previous studies tracked the evolution of the growing mixing layer towards a self-similar state while the current study seeks to artificially impose a desired statistical state. However, the result does demonstrate that the STF method can potentially be used to relatively

quickly achieve an approximate initial condition for the mean velocity in the self-similar mixing layer.

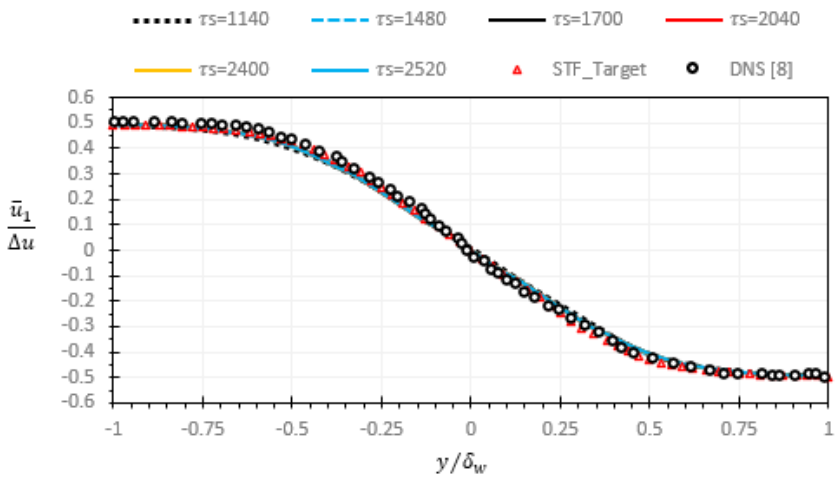

Fig. 58. Mean streamwise velocity for forcing simulation of temporally-developing turbulent mixing layer at $C_f = 1, \tau_s = 1140$, 1480, 1700, 2040, 2400, 2520 and target state on refined grid.

6.4.2. Resolved Turbulent Stress

Figure 59 shows the contours of resolved turbulent stress for forcing simulation of temporally evolving turbulent mixing shear layer at $C_f = 1, \tau_T = 1E-06\ s,$ and $\tau_s = 2040$. The result shows that the statistical profiles are approximately homogeneous in the streamwise direction (though not shown, the contours are similarly distributed in the spanwise direction), and a clear variation is present in the vertical direction. The peak values for all components lie approximately at the center of the mixing layer, as expected.

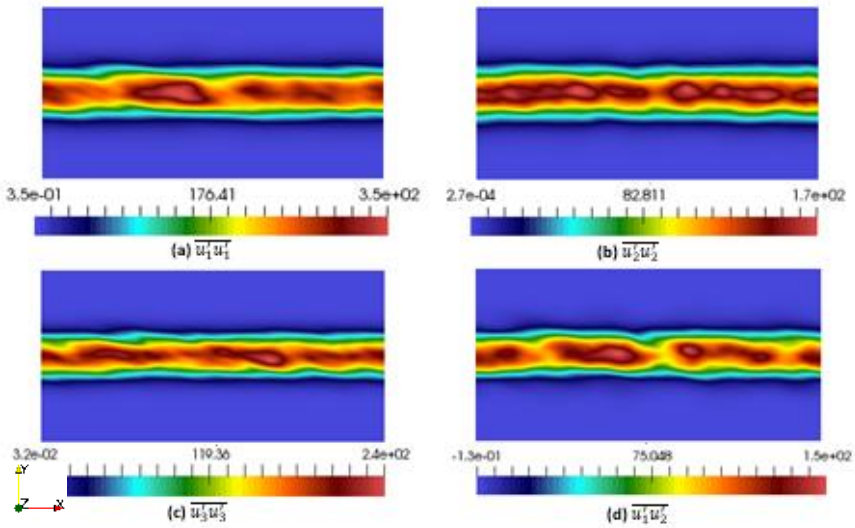

Fig. 59. Contours of (a) streamwise $\overline{u_1'u_1'}$, (b) vertical $\overline{u_2'u_2'}$, and (c) spanwise $\overline{u_3'u_3'}$ normal stress, and (d) Reynolds shear stress $\overline{u_1'u_2'}$ for forcing simulation of temporally-developing turbulent mixing layer at $C_f = 1, \tau_s = 2040$ on refined grid.

Figure 60 shows the predicted plane-averaged normal and shear Reynolds stress components for the forcing simulation of TTML at $C_f = 1, \tau_T = 1E-06\ s$, and different simulation times. Two points are apparent. First, the peak turbulence values are located in the center of the domain in agreement with the imposed target distributions. Second, at simulation times of $1700 \leq \tau_s \leq 2520$, the resolved turbulent stress profiles are all statistically converged. Table 9 shows that 101% of $\overline{u_1'u_1'}^{**}$, 89% of $\overline{u_2'u_2'}^{**}$, 96.8% of $\overline{u_3'u_3'}^{**}$, and 105% of $\overline{u_1'u_2'}^{**}$ are reproduced by the STF method at $\tau_s = 2040$.

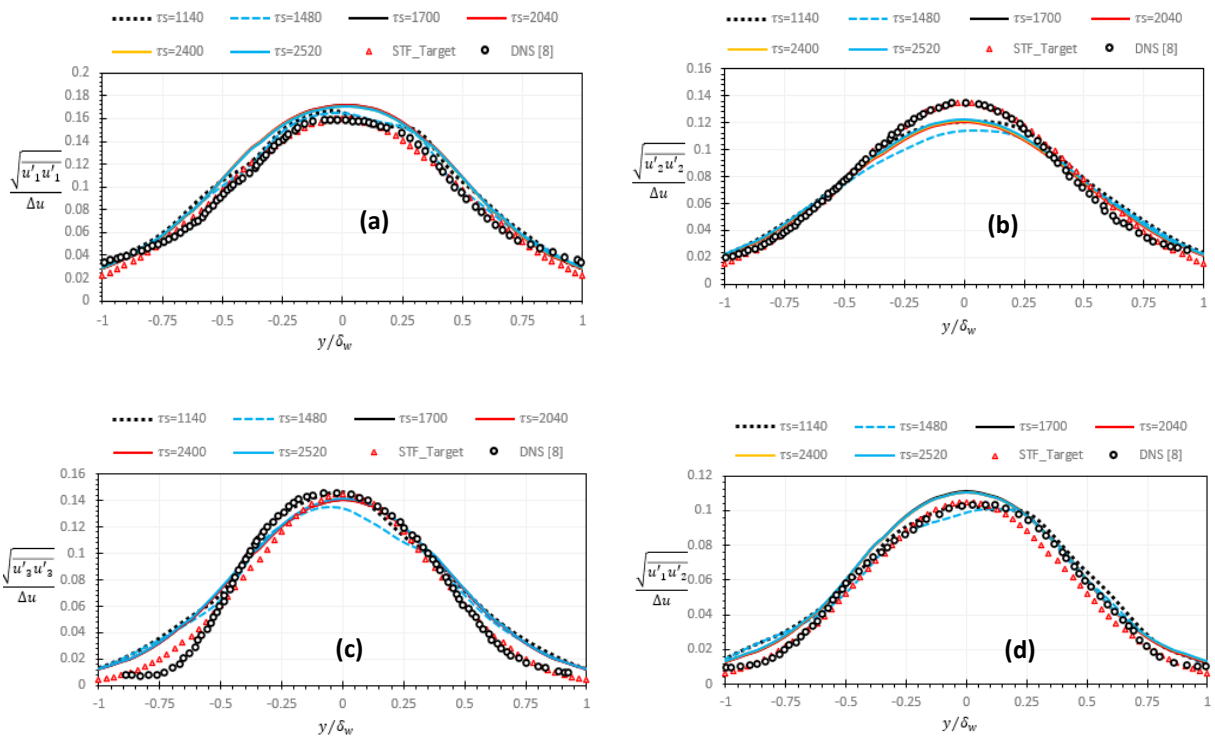

Fig. 60. (a) Streamwise (b) vertical and (c) spanwise root mean square (RMS) velocity, and (d) Reynolds shear stress for forcing simulation of temporally-developing turbulent mixing layer at $C_f = 1, \tau_s = 1140$, 1480, 1700, 2040, 2400, 2520 and target state on refined grid, compared to DNS[74].

6.4.3. Energy Spectrum

To investigate the spectral characteristics of the turbulence generated by the STF method, the fast Fourier transform was applied to the streamwise fluctuating velocity field at different dimensionless simulation times, τ_s, to obtain the one-dimensional energy density as a function of

wavenumber magnitude (κ) at the mixing layer centerplane. Figure 61 shows one dimensional energy spectra for $C_f = 1, \tau_T = 1E-06\, s$, and different values of simulation time, τ_s. Two interesting points are apparent from the energy spectra. First, qualitative energy spectra profiles effectively reproduce the correct behavior and match the Kolmogorov -5/3 law in the inertial region of the spectrum. Second, energy spectra obtained at different simulation times (τ_s) are slightly different near the low- and high-wavenumber portions, consequently with only very small differences in 1D energy spectra at different values of τ_s.

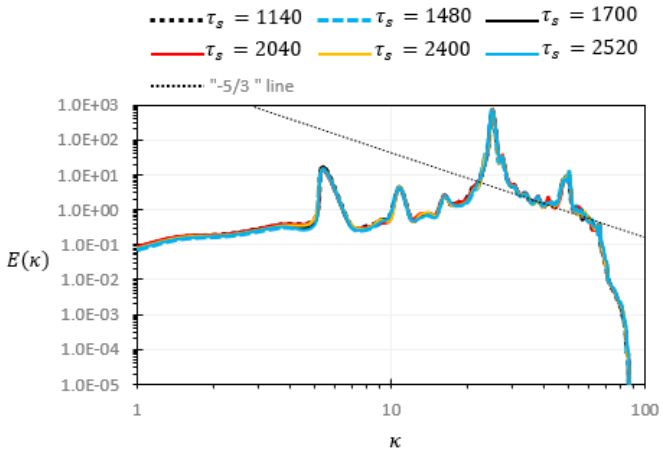

Fig. 61. One dimensional energy spectra for forcing simulation of temporally-devolving turbulent mixing layer at $C_f = 1, \tau_s = 1140$, 1480, 1700, 2040, 2400, and 2520 on refined grid.

6.4.4. Effect of Mesh Resolution

Figures 58 and 60 show that STF target data is in very good agreement with DNS data [8] but slightly different, hence both DNS data and target statistics will be used to benchmark results

for the remaining sections of this study. Figure 62 illustrates qualitative features by showing contours of instantaneous velocity magnitude for forcing simulation of TTML at $C_f = 1, \tau_T = 1E-06\ s,$ and $\tau_s = 2040$ on coarse (131,072 cells) and refined (1.049 million cells) grids. Finer grained features of the resolved velocity are more apparent on the refined grid compared to the coarse grid as shown in Fig. 62, which implies more resolution of small-scale flow features as the mesh resolution is increased, as expected.

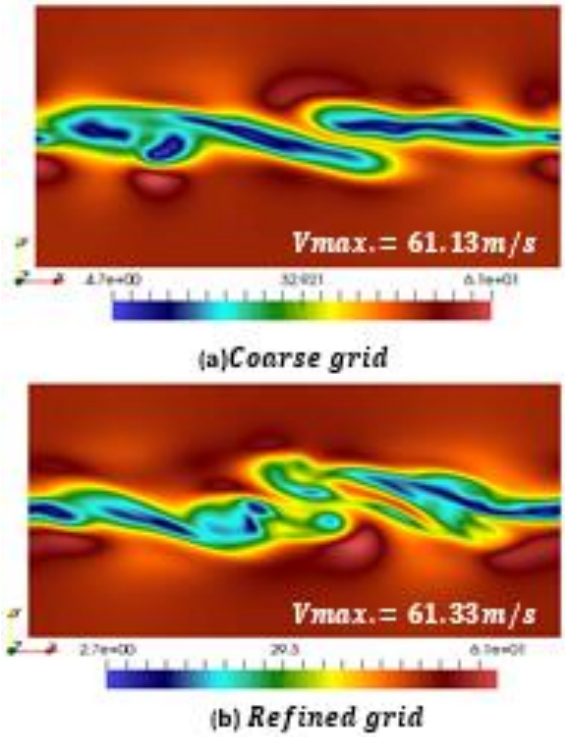

Fig. 62. Contours of instantaneous velocity magnitude for forcing simulation of temporally-developing turbulent mixing layer at $C_f = 1$, and $\tau_s = 2040$ on coarse and refined grids.

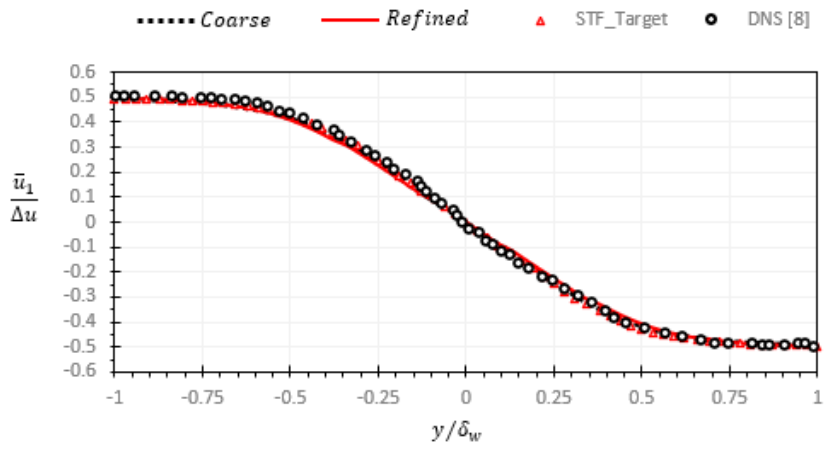

Fig. 63. Mean streamwise velocity for forcing simulation of temporally-developing turbulent mixing layer at $C_f = 1$, and $\tau_s = 2040$ on coarse and refined grid, compared to DNS[74].

Figure 63 illustrates the effect of mesh refinement on predicted mean streamwise velocity profiles for forcing simulation of TTML at $C_f = 1, \tau_T = 1E-06\ s,$ and $\tau_s = 2040$. The profiles are in good qualitative and quantitative agreement with DNS data [74]. It is also clear that the mean velocity distribution is insensitive to mesh refinement. This is expected since the forcing terms in the STF method include a component specifically designed to drive the mean flow towards the target distribution, and the forcing is independent of mesh resolution level.

Figure 64 shows the contours of streamwise resolved turbulent stress at $C_f = 1, \tau_T = 1E-06\ s,$ and $\tau_s = 2040$ on coarse and refined grids. The distribution of turbulent stress is qualitatively similar on both grids.

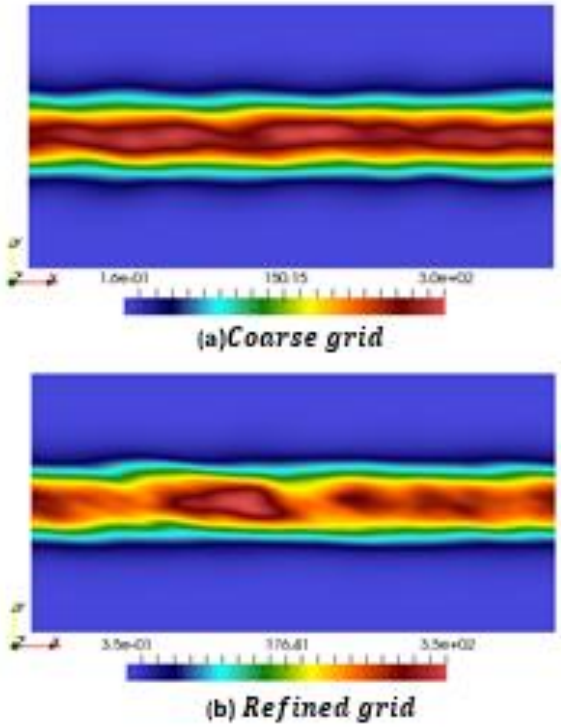

Fig. 64. Contours of streamwise normal stress, $\overline{u_1' u_1'}$ for forcing simulation of temporally-developing turbulent mixing layer at $C_f = 1,$ and $\tau_s = 2040$ on coarse and refined grids.

Additionally, Fig. 65 quantitatively shows the predicted turbulence intensities (RMS velocities) in the streamwise, wall-normal, and spanwise directions and the Reynolds shear stress. All profiles are in close agreement with DNS [74] and/or STF target data, similar to Fig. 60. Likewise, the results from the coarse and refined grids are close to one another, indicating the insensitivity of STF to mesh resolution in terms of one-point statistical quantities.

Figure 66 highlights the differences in the spectral characteristics of one-dimensional energy spectra on coarse and refined grids. While the energy spectra profiles are in qualitative agreement and approximately match the -5/3 law in the inertial range, differences are apparent at regions of low and high wavenumber. As expected, the maximum resolved wavenumber increases by a factor of two on the refined grid. Interestingly, the location of peak energy density, corresponding to the energy containing large-scale eddies, also corresponds to a higher wavenumber on the refined mesh.

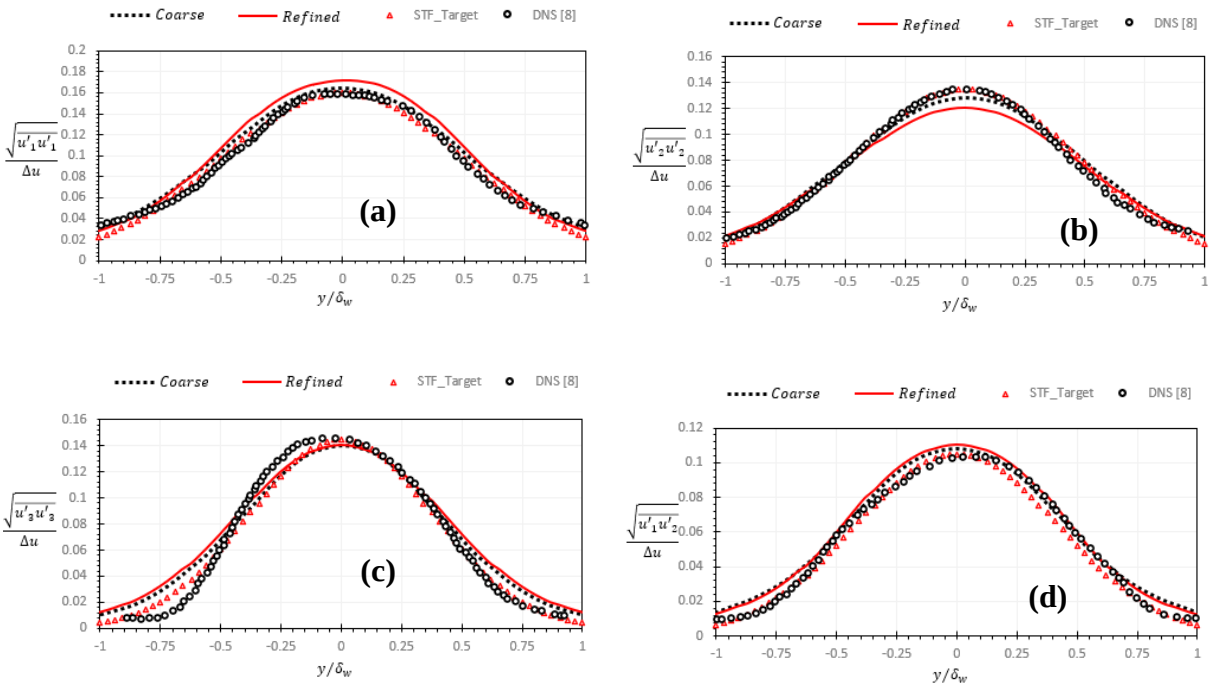

Fig. 65. (a) Streamwise (b) vertical and (c) spanwise root mean square (RMS) velocity, and (d) RMS velocity of Reynolds shear stress for forcing simulation of temporally-developing turbulent mixing layer at $C_f = 1$ and $\tau_s = 2040$ on coarse and refined grids, compared to DNS[74].

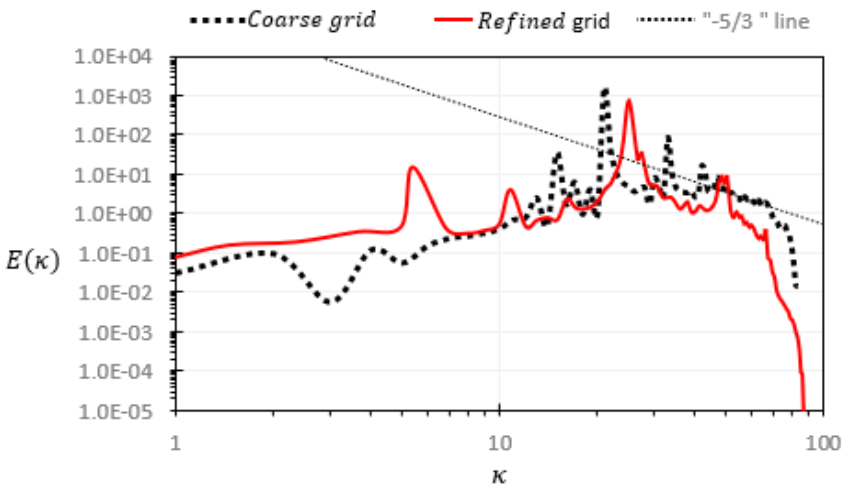

Fig. 66. One dimensional energy spectra $(\overline{u_1' u_1'})$ for forcing simulation of temporally-developing turbulent mixing layer at $C_f = 10$, and $\tau_s = 2040$ on coarse and refined grids .

6.4.5. Effect of Forcing Coefficient

Figure 67 illustrates the effect of varying the forcing coefficient, C_f, on contours of instantaneous velocity magnitude for forcing simulation of TTML at $\tau_s = 2040$ on coarse and refined grids. It is evident that the structure of the instantaneous flowfield is qualitatively similar for the two highest values of C_f, but shows greater vertical extent of turbulent fluctuations for the lowest value $C_f = 0.1$. In addition, the maximum resolved velocity magnitude increases as C_f increases, which is expected since the greater the value of C_f the more strongly the instantaneous velocity is forced toward the instantaneous target value.

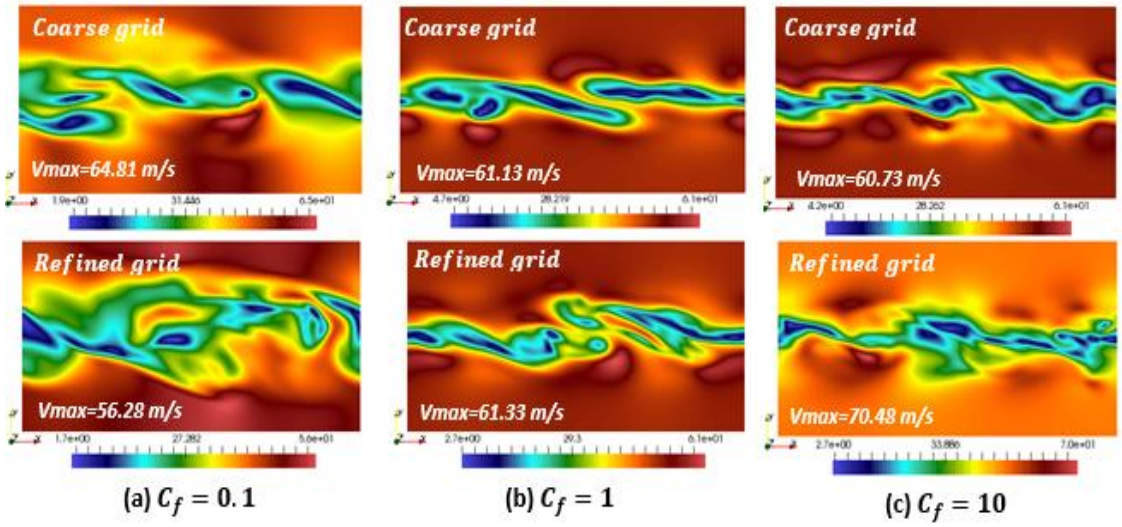

Fig. 67. Contours of instantaneous velocity magnitude with maximum value (Vmax) indicated, for forcing simulation of temporally-developing turbulent mixing layer at $C_f = 0.1, 1, 10$, and $\tau_s = 2040$ on coarse and refined grids.

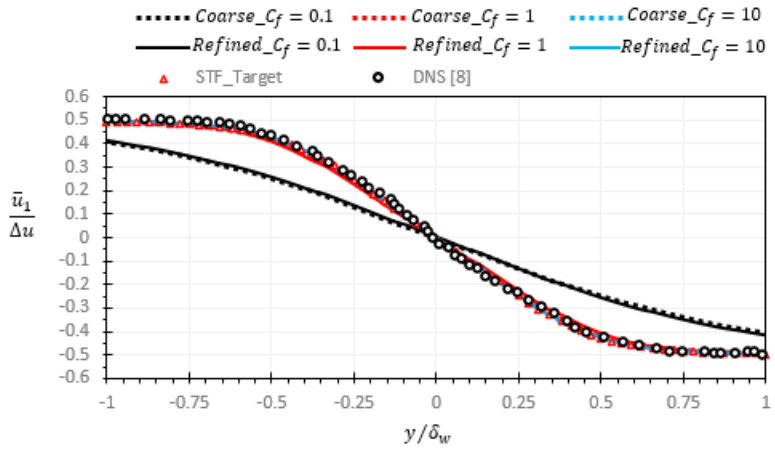

Fig. 68. Mean streamwise velocity for forcing simulation for forcing simulation of temporally-developing turbulent mixing layer at $C_f = 0.1, 1, 10$, and $\tau_s = 2040$ on coarse and refined grids.

Figure 69 shows the predicted mean streamwise velocity profiles at $C_f = 0.1, 1, 10$ at $\tau_s = 2040$ on coarse and refined grids. Regardless of mesh resolution, the profile deviates significantly from DNS data [74] at $C_f = 0.1$, while other profiles are in relatively good agreement with DNS data [74]. This indicates that higher accuracy of results is attained with higher values of C_f, as expected. As shown in Table 9, the most improved prediction of $\bar{u}_1^*$ is at $C_f = 10$ with relative integral error of -0.15% and -0.09% on coarse and refined grids respectively.

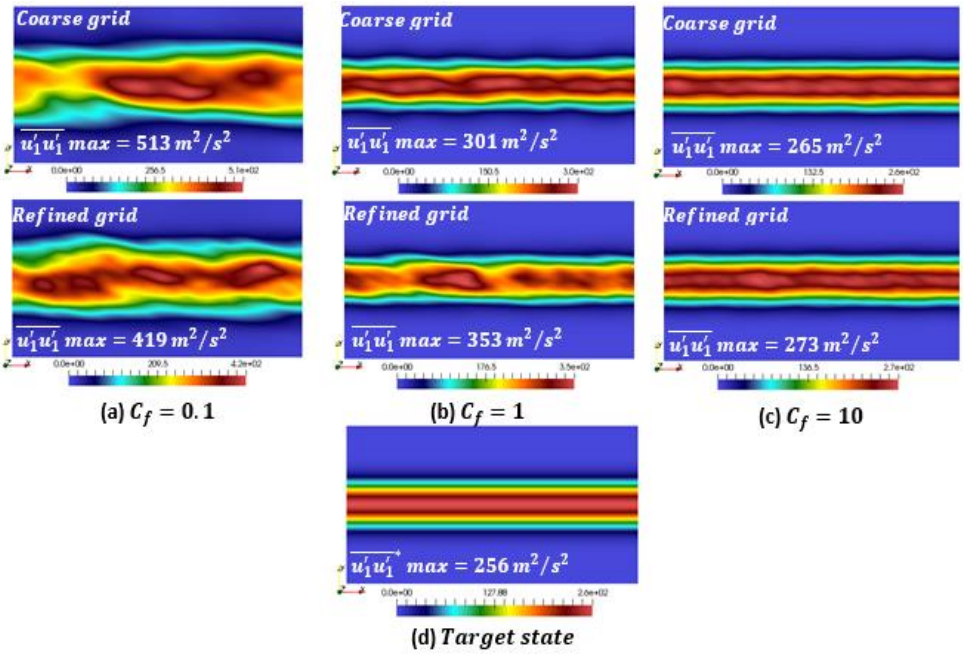

Fig. 69. Contours of streamwise normal stress, $\overline{u_1'u_1'}$ for forcing simulation of temporally-developing turbulent mixing layer at $C_f = 0.1, 1, 10$, and $\tau_s = 2040$ on coarse and refined grids.

Figure 69 shows contours of the streamwise normal turbulent stress at $\tau_s = 2040$ on the coarse and refined grids, for three different values of C_f. For comparison purposes the target distribution is also shown. It is clear that at C_f = 0.1, the width of the turbulent layer is overpredicted relative to the target and the flow shows strong inhomogeneity in the spanwise direction. For the highest value of $C_f = 10$, the distribution is more homogeneous and agrees best with the target distribution. Figure 73 further illustrates that at C_f = 0.1, the forcing coefficient is inadequate to reproduce the target turbulent statistics. Errors in peak predicted values range from a maximum of +22.4% with $C_f = 0.1$ to a minimum of -2.9% at $C_f = 10$. Interestingly, differences in results between coarse and refined meshes are also reduced as the value of C_f is increased from 0.1 to 10. Overall, regardless of mesh resolution, it is apparent that an increase in the value of C_f over the range investigated increases the accuracy of the STF method results.

Table 9 further quantitatively highlights the predicted ratio of peak resolved-to-target turbulence statistics at $\tau_s = 2040$. The STF method results at $C_f = 10, \tau_T = 1E-06\ s$ show the best quantitative agreement with DNS while the results for $C_f = 0.1$ deviate from the target and/or DNS data significantly. It is concluded that the capability of the STF method to reproduce turbulence statistics synthetically is validated provided the value of the forcing coefficient is sufficiently high. Specifically, on the refined grid with $C_f = 10$, and $\tau_T = 1E-06\ s$, the method can reproduce approximately 100% of $\overline{u_1' u_1'}^*$, 97% of $\overline{u_2' u_2'}^*$, 96% of $\overline{u_3' u_3'}^*$, and 99% of $\overline{u_1' u_2'}^*$ at a dimensionless simulation time (τ_s) of 2040.

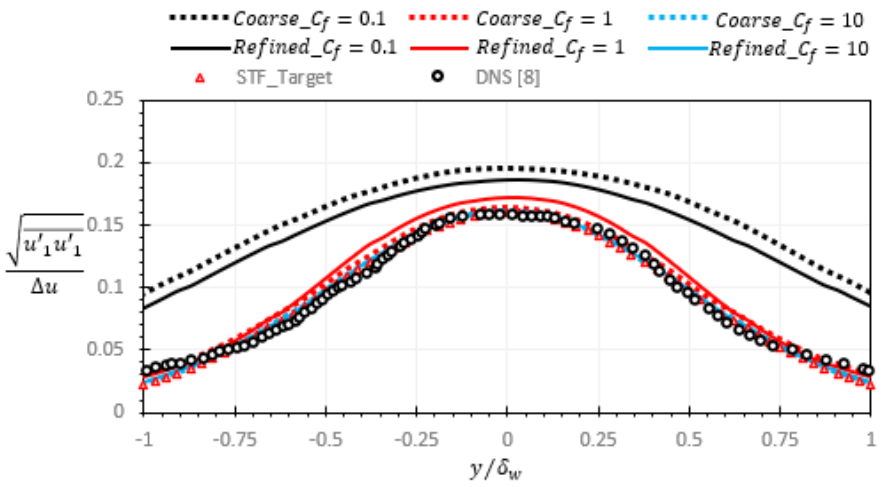

Fig. 70. Streamwise root mean square (RMS) velocity for forcing simulation of temporally-developing turbulent mixing layer at $C_f = 0.1, 1, 10$, and $\tau_s = 2040$ on coarse and refined grids, compared to DNS[74].

To understand the spectral characteristics of the TTML turbulence generated by STF method with different values of C_f, Fig. 71 shows the one-dimensional normalized energy spectra for forcing simulation of the temporally-developing turbulent mixing shear layer at C_f = 0.1, 1, and 10, $\tau_T = 1E-06\ s$ and $\tau_s =$ 2040. Slight differences in the energy spectra profiles are evident but peak values and overall behavior of the spectra are almost identical for the cases with C_f = 1 and 10. Once again the energy spectra profiles qualitatively match the -5/3 law in the inertial range.

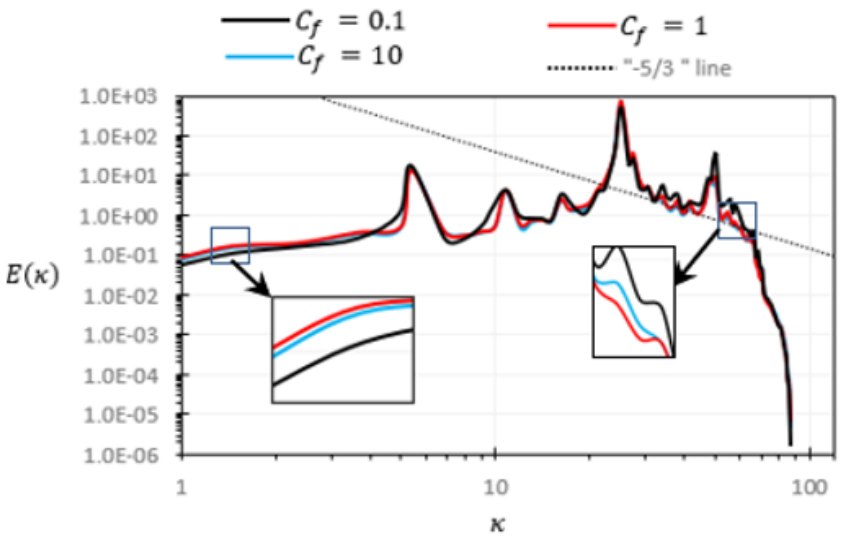

Fig. 71. One dimensional energy spectra for forcing simulation of temporally-developing turbulent mixing layer at $C_f = 0.1, 1, 10$, and $\tau_s = 2040$.

6.4.6. Effect of Subgrid Stress Modeling

To investigate effect of implicit and/or explicit LES modeling, simulations were run using Monotonically Integrated LES (MILES) and compared to the simulations run using the Smagorinsky model. Both simulations were run on the refined grid with a value of the forcing coefficient C_f = 1. Table 9 and Figures 72-74 illustrate the similarities and differences using the different subgrid stress models. There is a negligible difference in results of the STF method obtained with the MILES or Smagorinsky model. The maximum relative difference in the prediction of peak values of the Reynolds stress components was less than 1.5%. These results suggest that the STF method is capable of accurately reproducing turbulent one-point statistics regardless of the details of the LES modeling methodology.

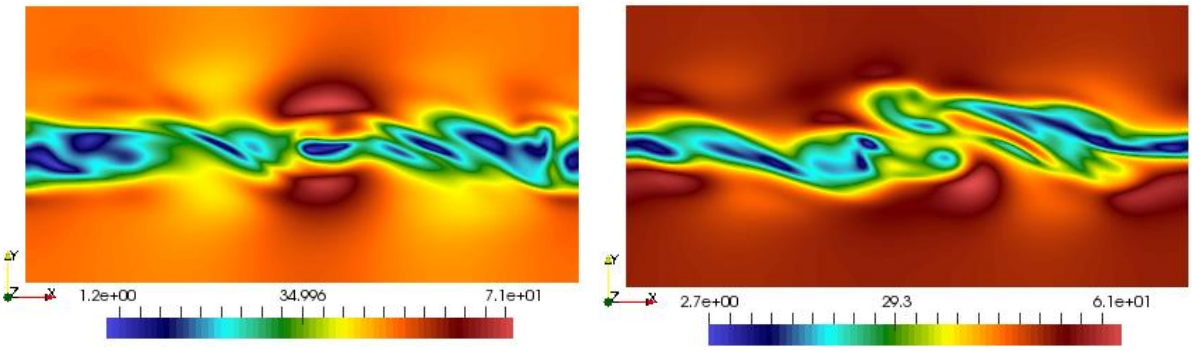

(a) MILES, Vmax = 71.20m/s (b) SMAG, Vmax = 61.33m/s

Fig. 72. Contours of instantaneous velocity magnitude with maximum value (Vmax) indicated for forcing simulation of temporally-developing turbulent mixing layer at $\tau_s = 2040$, and $C_f = 1$ using MILES and Smagorinsky (SMAG) model on refined grid.

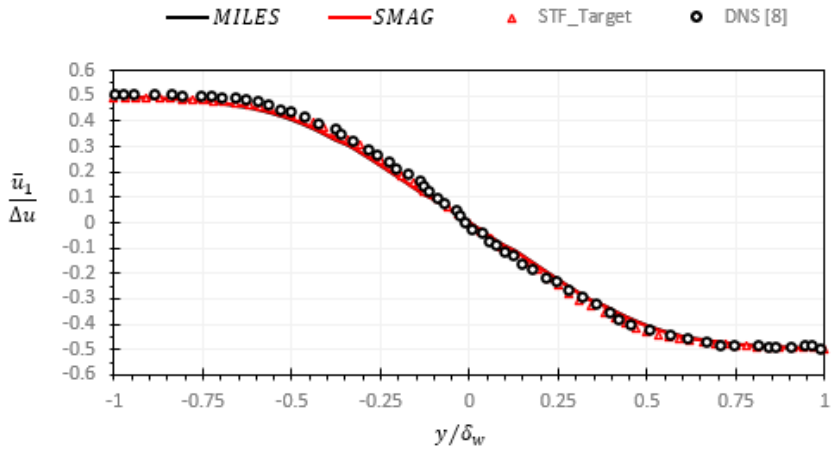

Fig. 73. Mean streamwise velocity for forcing simulation of temporally-developing turbulent mixing layer at $\tau_s = 2040$, and $C_f = 1$ using MILES and Smagorinsky (SMAG) model on refined grid, compared to DNS[74].

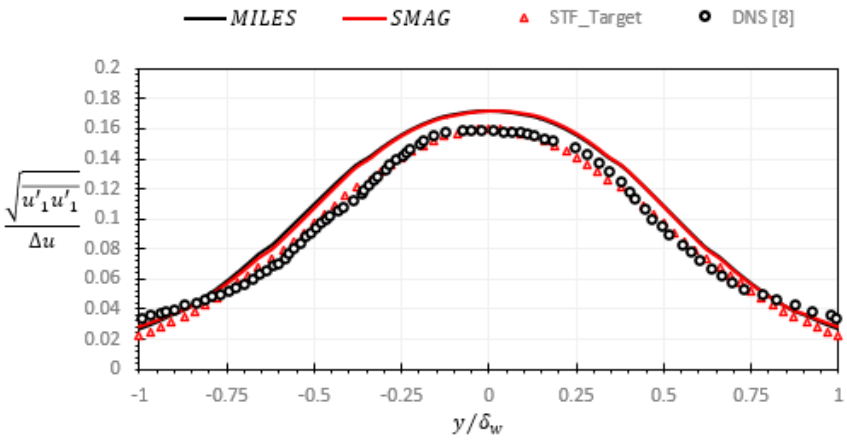

Fig. 74. Streamwise RMS velocity for forcing simulation of temporally-developing turbulent mixing layer at $\tau_s = 2040$, and $C_f = 1$ using MILES and Smagorinsky (SMAG) model on refined grid, compared to DNS[74].

6.5. SUMMARY AND CONCLUSION

A new forcing method for synthetic turbulence generation of initial conditions was applied to the test case of large-eddy simulation (LES) of a temporally-developing turbulent mixing layer (TTML). The new method, denoted Statistically Targeted Forcing (STF), incorporates a source term in the momentum equation to drive the local, instantaneous velocity vector towards a target value. Simulation results in this study are compared to DNS studies of Pantano et al. [74].

The method was evaluated for different values of model coefficients and mesh resolution using LES with the Smagorinsky subgrid stress model. An additional test case was run using MILES. Qualitative and quantitative results were presented which showed that the method was able to reproduce DNS target statistical quantities as initial conditions for the temporally evolving

mixing layer. Specifically, the method reproduced a relatively stable and accurate self-similar state at $1700 \leq \tau_s \leq 2600$ on both coarse and refined grids. This state is similar to the DNS result of Rogers and Moser [73] with self-similar state attained at $105 < \tau_s < 150$, and that of Pantano and Sarkar [74] attained at $261 < \tau_s < 518$. Effect of mesh resolution on the method was also investigated and results showed that the method is relatively insensitive to mesh resolution with coarse-to-refined grids maximum relative error of about 0.2%. The effect of forcing coefficient on the method was also evaluated, and the results presented showed that the STF method agrees more closely with target statistical values as the value of the forcing coefficient is increased. Results using different LES subgrid stress models showed little difference, indicating that the model is relatively agnostic to details of the model or mesh.

In sum, the method can effectively reproduce target/DNS mean velocity and resolved turbulent stress predictions for use as initial conditions of temporally developing mixing layers. Future work will investigate the evolution of the mixing layer once the STF generated initial conditions are applied. We will also seek to extend the method capability to higher Mach number flows.

CHAPTER VII

CONCLUSIONS & FUTURE WORK

7.1. SUMMARY

This dissertation presents improved methods for turbulence modeling in computational fluid dynamics simulations. The focus is on scale-resolving methods, in which some portion of the fluctuating variable field is resolved in the simulation, in contrast to Reynolds-averaged Navier-Stokes (RANS) simulations, which only solve directly for the mean (ensemble- or time-averaged) portion of the variable field. This work addresses issues relevant to large-eddy simulation (LES) and hybrid RANS-LES models. Two novel contributions have been included. First is a modified dynamic hybrid RANS-LES (DHRL) model for improved turbulent heat transfer prediction. Second is a new method for synthetic turbulence generation in CFD simulations, denoted the statistically targeted forcing (STF) method. The formulation and implementation of these methods for different test cases are investigated and discussed in Chapters III, IV, V, and VI. The key highlights of those chapters are summarized here.

In Chapter III, a new version of DHRL was proposed in which a separate RANS-to-LES blending function for turbulent heat flux is computed based on the statistics of the resolved fluctuating temperature field. The performance of the modified variant of the DHRL model was comprehensively investigated and results were compared to other currently used turbulence models including a Reynolds-averaged Navier Stokes (RANS) model (SST k-ω), popular hybrid RANS-LES models (DDES and DDES), and the baseline DHRL model. The test case used for model evaluation was turbulent channel flow with imposed mean streamwise or spanwise

temperature gradient. This case was chosen because it represents a canonical representative case for more general wall-bounded flows with non-negligible wall-parallel heat transfer, and because high-fidelity direct numerical simulation (DNS) results are available for validation purpose. Simulation results highlight the inability the SST k-ω model, and eddy-viscosity RANS models more generally, to accurately predict turbulent heat transfer for cases in which the mean velocity and temperature gradients are not well-aligned. All of the hybrid RANS-LES models were significantly more accurate than the RANS models. The new modified version of the DHRL model showed improved accuracy versus the baseline DHRL variant for cases with both streamwise and spanwise imposed temperature gradient. For the streamwise case the modified DHRL model was the most accurate of all models tested, and was comparable to the DDES model for the spanwise case, both of which outperformed the baseline DHRL and IDDES models. The contents of Chapter III have been published in the *Journal of Fluids Engineering* in a paper titled "Hybrid RANS–LES Simulation of Turbulent Heat Transfer in a Channel Flow With Imposed Streamwise or Spanwise Mean Temperature Gradient."

In Chapter IV, a newly proposed statistically targeted forcing (STF) method for synthetic turbulence generation (STG) was presented. The STF method is a variant of STG with controlled forcing within the simulation domain, implemented via added source terms in the momentum and energy equations to drive the local, instantaneous velocity vector towards a target value. The performance of the STF method was evaluated by performing several test simulations of homogeneous turbulence, using LES with the Smagorinsky subgrid stress model and or the MILES (implicit LES) modeling approach. The resulting flowfield was interrogated to evaluate the accuracy of the method for reproducing target and/or realistic turbulent flow conditions for

the isotropic and anisotropic turbulence test cases. Comprehensive results were presented including Reynolds stress distributions and flowfield energy spectra, highlighting the effect of critical parameters such as averaging technique, mesh resolution, spatially-filtering, and STF model parameters. In sum, the results indicate that the STF method is capable of reproducing a synthetic homogeneous turbulence field with prescribed first- and second-order statistics (over 98% accuracy was documented) and appropriate spectral content, which can be used to specify initial and/or boundary conditions for LES simulations. The method is relatively simple to implement, non-stochastic, stable, and computationally efficient. The contents of Chapter IV have been submitted to the *Journal of Fluids Engineering* in a paper titled "Evaluation of a Statistically Targeted Forcing Method for Synthetic Turbulence Generation in Scale-Resolving Simulations."

In Chapter V, the statistically targeted forcing (STF) method was extended to the case of spatially-developing freestream turbulence. The capability of STF method to accurately reproduce freestream turbulent inflow statistics in a prototypical channel flow domain was evaluated. Three different classes of modeling approach were investigated, including RANS, LES, and hybrid RANS-LES. All simulations used a running time-averaging technique to compute mean statistics, approximating Reynolds-averaging for stationary flow. Results were presented showing the effects of mesh sensitivity, model parameters, spatial filtering, and explicit LES modeling. Results were compared to target turbulent statistics to evaluate the efficacy of the STF method. It was determined that the STF method is capable of reproducing a synthetic freestream turbulence field with prescribed first- and second-order statistics and appropriate spectral content, which can be used to specify inflow boundary conditions for different classes of modeling approach for scale-resolving simulations. It was found that an appropriate choice of

model parameters made it possible to produce turbulent kinetic energy levels within the Smagorinsky, MILES, and DHRL modeling framework that were within 95%, 91% and 90%, respectively, of the target turbulence levels. Results suggest that the STF method may therefore offer an attractive alternative for synthetic turbulence generation in three-dimensional Navier-Stokes CFD for both LES and hybrid RANS-LES simulations. The contents of Chapter V have been submitted to the *Journal of Fluids Engineering* in a paper titled "Statistically Targeted Forcing Method for Synthetic Generation of Freestream Turbulence in Scale-Resolving Simulations."

In Chapter VI, the application of the STF method within the LES framework to a temporally-developing turbulent mixing layer (TTML) flow was investigated. The objective was to investigate the capability of the method to accurately reproduce an initial condition velocity and pressure field for the simulation of mixing layer evolution. The performance of the STF method was evaluated by performing several test simulations of the TTML, using LES with the Smagorinsky subgrid stress model and the MILES (implicit LES) modeling approach. Simulation results were compared to DNS results available in the literature. Qualitative and quantitative results were presented which showed that the method was able to effectively reproduce DNS target statistical quantities as initial conditions for the temporally-devolving mixing layer. Specifically, the method reproduced a relatively stable and accurate self-similar state at on both coarse and refined grids. The effect of mesh resolution was also investigated and results showed that the STF method produced the correct initial state for a range of grid sizes. Overall, the results are significant because they show that the STF concept may be extended beyond freestream turbulence to cases in which mean velocity gradients are non-zero. The contents of Chapter V

were presented and published at the 2021 ASME Fluids Engineering Division Summer Meeting in a paper titled “Statistically Targeted Forcing (STF) Method for Synthetic Turbulence Generation of Initial Conditions in Three-Dimensional Turbulent Mixing Layer Flow.”

7.2. CONCLUSIONS

The most significant conclusions of this research effort are the following.

Chapter III:

- For wall-bounded turbulent flow, traditional eddy-viscosity models cannot accurately resolve turbulent heat transfer in the wall-parallel (streamwise or spanwise) directions, due to the mis-alignment of the mean velocity and temperature gradients. Eddy-viscosity models can accurately resolve the wall-normal heat transfer component, which is expected since these models have been well calibrated to reproduce wall shear stress and convection heat transfer rates in attached boundary layer flows.
- All of the hybrid RANS-LES models investigated were able to predict heat transfer in all three directions (normal, streamwise, and spanwise) with reasonable accuracy, showing the correct trends and approximately reproducing the DNS validation data. The DHRL model showed the most consistently accurate results among the models tested.
- The new variant of the DHRL model proposed in this study, in which separate RANS-to-LES blending functions are implemented for the momentum and energy equations, showed improvement over the baseline DHRL model for prediction of turbulent heat transfer in all three directions. Since the model variant is based on a straightforward

application of the DHRL concept to the energy equation, it is suggested that the new variant should be in place of the baseline variant for simulations involving turbulent heat transfer.

Chapter IV:

- The STF method was demonstrated to produce a temporally and spatially varying velocity field for homogeneous flow with qualitative features indicative of three-dimensional turbulence, and with turbulent kinetic energy and Reynolds stress components close to target, user-specified values.
- As mesh refinement level increased, the overall energy levels and large-scale flow features produced by the STF method showed little change, but spectral analysis showed that higher wavenumber velocity modes were resolved
- Both volume and time averaging techniques for ensemble averaging were successfully demonstrated for the STF method. However, cases using volume averaging showed more rapid convergence to a statistically stationary state, while cases using time averaging showed a clear lag in the development of turbulent statistics, as expected.
- The simulation results are critically dependent on the value of the forcing time scale. A smaller time scale results in a stronger forcing term and increases the accuracy of the STF method in terms of agreement with target Reynolds stress values.
- Spatial filtering was shown to be an effective means of controlling the large-eddy length scale of the synthetically generated turbulent flow. A decrease in the filter time

scale resulted in a corresponding decrease in the integral length scale, as indicated by visualized velocity contours and by energy spectra.

Chapter V:

- The STF method can be straightforwardly extended to the case of spatially-developing freestream flow. Results showed that an appropriate choice of model parameters produced Reynolds stress and turbulent kinetic energy levels within 5% of user-defined target values in the forcing region. Downstream of the forcing region, the turbulent energy showed streamwise decay indicative of freestream turbulence.
- The effects of mesh refinement, varying forcing time scale, and spatial filtering for the freestream turbulence test case were consistent with results for the homogeneous turbulence case examined in Chapter IV.

Chapter VI:

- The STF method can be effectively extended to provide initial conditions for simulation of temporally developing shear layer flows. Results showed that mean velocity and Reynolds stress profiles were well predicted when an appropriate set of model parameters was employed.
- Mean velocity and Reynolds stress distributions obtained using the STF method were found to be relatively insensitive to mesh refinement, although the range of resolved turbulent scales increased as the characteristic mesh size was reduced.
- Consistent with results from Chapters IV and V, the accuracy of the STF method increased as the forcing time scale was reduced.

7.3. FUTURE WORK

This study presented one method for improving the performance of the dynamic hybrid RANS-LES (DHRL) model by more effectively prescribing the blending function between RANS and LES terms in the energy equation. Further improvements to the DHRL model are currently under consideration. These include implementation of a new blending function that identifies regions of the flow that should be resolved using a pure LES model, based on the level of resolved fluctuating strain rate. This form of DHRL allows wall-bounded regions to be addressed using the existing DHRL model formulation while separated and freestream regions are resolved using LES. Initial tests with this version have been documented and submitted for presentation and publication at the ASME 2021 IMECE Conference.

Further improvement to DHRL can potentially be obtained by adopting more advanced RANS models within the DHRL framework, for example by incorporating non-linear eddy viscosity models for the turbulent stress and heat flux terms. As currently implemented, the performance of the DHRL model depends on the inherent RANS model with a simple isotropic gradient-based diffusion model as shown in Chapter III, Eqs. (8, 23, and 24). Future work will investigate quadratic, cubic, or even explicit algebraic Reynolds stress models for the RANS component.

The STF method has successfully been tested and documented for homogeneous turbulent flow, freestream turbulent flow, and temporally-developing turbulent mixing layer flow. Future work will investigate the application to evolution of the mixing layer once the STF generated initial conditions are applied in a more complex domain. Extension of the method's capability to higher Mach number flows will also be considered. Additionally, application of the STF method

to wall-bounded turbulent channel flows is presently being investigated. For this application, the target Reynolds stress tensor components can be obtained from a precursor RANS simulation or prescribed based on planar averaging of available DNS results. Eventually, the STF method will be adopted directly in hybrid RANS-LES simulations to investigate the ability of the method to facilitate transition from RANS to LES resolution in critical areas of the simulation domain. For such an implementation, the RANS solution obtained as part of the DHRL simulation will be used to determine a target Reynolds stress distribution, rather than being prescribed prior to the simulation.

The development of improved DHRL capability coupled with the use of the STF method to enable rapid and accurate transition between modeling modes, will potentially yield a flexible and powerful modeling approach that can be used to tailor simulations that seamlessly blend RANS and LES type solutions based on the needs of the user.

LIST OF REFERENCES

[1] H. Tennekes, J.L. Lumley, A First Course in Turbulence, MIT Press, Cambridge, UK, 1972.

[2] U. Frisch, Turbulence; The Legacy of A.N. Kolmogorov, Cambridge University Press, Cambridge, UK, 1995.

[3] S.B. Pope, Turbulent Flows, Cambridge University Press, Cambridge, UK, 2000.

[4] J. Mathieu, J. Scott, An Introduction to Turbulent Flow, Cambridge University Press, Cambridge, UK, 2000.

[5] P.S. Bernard, J.M. Wallace, Turbulent Flow; Analysis, Measurement, and Prediction, John Wiley and Sons, Hoboken, NJ, USA, 2002.

[6] S.A. Thorpe, The Turbulent Ocean, Cambridge University Press, Cambridge, UK, 2005, p. 484.

[7] J.C. Wyngaard, Turbulence in the Atmosphere, Cambridge University Press, Cambridge, UK, 2010, p. 406.

[8] F.G. Schmitt, Y. Huang, Stochastic Analysis of Scaling Time Series: From Turbulence Theory to Applications, Cambridge University Press, Cambridge, UK, 2016, p. 220.

[9] M. Beniston, From Turbulence to Climate: Numerical Investigations of the Atmosphere with a Hierarchy of Models, Springer, 2012, p. 329.

[10] Stokes, G. (2009), " On the Theories of the Internal Friction of Fluids in Motion, and of the Equilibrium and Motion of Elastic Solids", In Mathematical and Physical papers (Cambridge Library Collection – Mathematics, pp. 75-129). Cambridge: Cambridge University Press, doi:10.1017/CBO9780511702242.005

[11] Hirsch, C., and Tartinville, B., 2009, "Reynolds-Averaged Navier-Stokes modeling for industrial applications and some challenging issues." Int. J. Computational Fluid Dynamics, 23, pp. 295–303.

[12] Spalart, P. R., 2000, "Strategies for turbulence modelling and simulations" Int. J. Heat Fluid Flow, 21, pp. 252-263.

[13] Bhushan, S., and Walters, D. K., 2012, "A dynamic hybrid RANS/LES modelling framework" Phys. Fluids, 24, No. 015103.

[14] Piomelli, U., Balaras, E., Pasinato, H., Squires, K. D., and Spalart, P. R., 2003, "The inner-outer layer interface in large-eddy simulations with wall-layer models," Int. J. Heat Fluid Flow, 24 (4), pp. 538-550.

[15] Schlüter, J. U., Pitsch, H., and Moin, P., 2004, "Large eddy simulation inflow conditions for coupling with Reynolds-averaged flow solvers," AIAA J., 42(3), pp. 478-484.

[16] Spalart, P. R. and Watmuff, J. H., 1993 "Experimental and Numerical Study of a Turbulent Boundary Layer with Pressure Gradients," J. Fluid Mech., 249, pp. 337– 371.

[17] Lund, T.S., Wu, X. and Squires, K.D., 1998, "Generation of Turbulent Inflow Data for Spatially-Developing Boundary Layer Simulations," J. of Comp. Phys., 140, pp. 233-258.

[18] Spalart, P.R., Strelets, M., and Travin, A., 2006 "Direct Numerical Simulation of Large-Eddy-Break-Up Devices in a Boundary Layer," Int. J. Heat and Fluid Flow, 27, pp. 902–910.

[19] Shur, M.L., Spalart, P.R., Strelets, M. Kh., and Travin, A.K., 2011, "A Rapid and Accurate Switch from RANS to LES in Boundary Layers Using an Overlap Region," Flow Turbul. Combust., 86, pp. 179–206.

[20] Araya, G., Castillo, L., Meneveau, C., and Cansen, K., 2011, "A Dynamic Multi-Scale Approach for Turbulent Inflow Boundary Conditions in Spatially Developing Flows," J. Fluid Mech., 670, pp. 581-605.

[21] Schlüter J. U., Pitsch H., and Moin P., 2005, "Outflow Conditions for Integrated Large Eddy Simulation/Reynolds-averaged Navier–Stokes Simulations," AIAA J., 43(1), pp. 156–164.

[22] Kraichnan, R. H., 1970, "Diffusion by a Random Velocity Field," Phys. Fluids, 13(1), pp. 22-31.

[23] Rogallo, R., "Numerical Experiments in Homogeneous Turbulence," Technical Memorandum 81315, NASA, September 1981.

[24] Orszag, S. and Patterson, G., 1972, "Numerical Simulation of Three-Dimensional Homogeneous Isotropic Turbulence," Phys. Rev. Lett., 28, pp. 76-79.

[25] Black, A. W. and Sparrow, E. M., 1967, "Experiments on turbulent heat transfer in a tube with circumferentially varying thermal boundary conditions" Trans. ASME, J. Heat Transf., 189, pp. 258-268.

[26] Quarmby, A. and Quirk, R., 1972, "Measurements of the radial and tangential eddy diffusivities of heat and mass in turbulent flow in a plain tube" Int. J. Heat Mass Transfer, 15, pp. 2309-2327.

[27] Maekawa, H., Kawada, Y., Kobayashi M., and Yamaguchi, H., 1991, "An experimental study on the spanwise eddy diffusivity of heat in a flat-plate turbulent boundary layer" Int. J. Heat Mass Transf., 34 (8), pp. 1991-1998.

[28] Kim J. and Moin P., 1989, "Transport of passive scalars in a turbulent channel flow in turbulent shear flows VI", (Edited by J. C. Andre et al.), pp. 85-96. Springer, Berlin.

[29] Kawamura, H., Abe, H., Matsuo Y., 1999, " DNS of turbulent heat transfer in channel flow with respect to Reynolds and Prandtl number effects" Int. J. Heat Fluid Flow, 20, pp. 196-207.

[30] Lu D.M. and Hetsroni G., 1995, "Direct numerical simulation of a turbulent open channel flow with passive heat transfer", Int. J. Heat Mass Transfer , 38, No. 17, pp. 3241-3251.

[31] Matsubara, K., Kobayashi, M., Maekawa, H. and Suzuki, K., 1998, "DNS of spanwise turbulent heat transfer in a channel", Turbulent Heat Transfer 2. Manchester, 1, pp. 1.23-1.32.

[32] Kawamura, H. and Kawamoto, N., 1998, "DNS and modeling of turbulent heat transfer in channel with spanwise mean temperature gradient," 13th Australian Fluid Mechanics Conference, Monash University, Australia, 13 -18 December.

[33] Kim, P. Moin, and Moser R., 1987, "Turbulence statistics in fully developed turbulent channel flow at low Reynolds number" J. Fluid Mech. 177, pp. 133-166 .

[34] Kasagi, N., Tonaita, Y., and Kuroda, A., 1992, " Direct numerical simulation of passive scalar field in a turbulent channel flow" J. Heat Transfer, Trans. ASME 114, pp. 598-606.

[35] Lyons S.L., Hanratty T. J. and McLaughlin J. B., 1991, "Direct numerical simulation of a passive heat transfer in a turbulent channel flow" Int. J. Heat Mass Transfer ,34, pp. 1149-1161.

[36] Walters, D.K., Bhushan, S., Alam, M.F. and Thompson, D.S., 2013, "Investigation of a dynamic hybrid RANS/LES modelling methodology for finite-volume CFD simulations," Flow Turbul. Combust. 91, No. 3, pp. 643-667.

[37] Shobayo O.O, Walters D., 2018, "Evaluation of performance and code-to-code variation of a dynamic hybrid RANS/LES model for simulation of backward-facing step flow," ASME. Fluids Engineering Division Summer Meeting, Volume 1: V001T08A002, doi:10.1115/FEDSM2018-83160.

[38] Spalart, P. R., Deck, S., Shur, M. L., Squires, K. D., Strelets, M., and Travin, A., 2006, “A new version of detached eddy simulation, resistant to ambiguous grid densities,” Theor. Comp. Fluid Dyn., 20, pp. 191-195.

[39] Shur, M. L., Spalart, P. R., Strelets, M., and Travin, A., 2008, “A hybrid RANS-LES model with delayed DES and wall-modelled LES capabilities,” Int. J. Heat Fluid Flow, 29, pp. 1638-1649.

[40] Menter, F. R., 1994, “Two-equation eddy-viscosity turbulence models for engineering applications,” AIAA J., 32, pp. 1598-1605.

[41] Fureby C. and Grinstein F. F., 1999, "Monotonically integrated large eddy simulation of free shear flows", AIAA J., 37, No. 5, pp. 544-556.

[42] Smagorinsky J., 1963, “ General circulation experiments with the primitive equations” Mon. Weath. Rev. 91 (3), pp. 99-164.

[43] Luke E. A., Tong X., and Chamberlain R., June 5,2016, “FlowPsi: An ideal gas flow solver-the user guide.” pp. 29-40.

[44] Toro E.F., Spruce M., and Speares M., 1994 “Restoration of the contact surface in the hll-riemann solver” Shock Waves, 4, pp. 25-34.

[45] Poe, N.M.W. and Walters, D.K., 2011 “A low- dissipation optimization-based gradient reconstruction (OGRE) in finite volume simulations” Proceedings of the ASME-JSME-KSME 2011 Joint Fluids Engineering Conference, July 24-29, Hamamatsu, Shizuoka, JAPAN.

[46] Moser, R. D., Kim, J., and Mansour, N. N., 1999 “ Direct numerical simulation of turbulent channel flow up to $Re_\tau = 590$” Phys. Fluids, 11 (4), 943-945.

[47] Roache, P.J., 1998, " Fundamentals of computational fluid dynamics", Hermosa Publishers, Albuquerque, New Mexico.

[48] Jamal T, Walters D., "Simulation of a 3D axisymmetric hill: Comparison of RANS and hybrid RANS-LES models," ASME Fluids Engineering Division Summer Meeting, Volume 1B, Symposia :V01BT25A010,doi: 10.1115/ FEDSM2016-7772.

[49] Jamal T., Walters D., Chitta V., "3D simulation of flow in a vortex cell using RANS and hybrid RANS-LES turbulence models," ASME International Mechanical Engineering Congress and Exposition, Volume 7: Fluids Engineering: V007T09A061 doi:10.1115/IMECE2017-70599.

[50] Kawamura H., Ohsaka K., Abe H.; Yamamoto K., "DNS of turbulent heat transfer in channel flow with low to medium-high Prandtl number fluid," Int. J. Heat Fluid Flow, 19 (5), pp. 482-491.

[51] Lee, S., Lele, S., and Moin, P., 1992, "Simulation of Spatially Evolving Compressible Turbulence and the Application of Taylor's Hypothesis," Phys. Fluids, 4, pp. 1521-1530.

[52] Lundgren, T. S., "Linearly Forced Isotropic Turbulence," Annual Research Briefs (Center for Turbulence Research, Stanford, CA, 2003), p. 461.

[53] Rosales, C., and Moniteau, C., 2005 "Linear Forcing in Numerical Simulations of Isotropic Turbulence: Physical Space Implementations and Convergence Properties," Phys. Fluids 17(9), 095106.

[54] Jarrin, N., Prosser, R., Uribe, J. C., Benhamadouche, S., and Laurence, D., 2006, "A Synthetic-eddy-method for Generating Inflow Conditions for Large Eddy Simulations," Int. J. Heat Fluid Flow, 27, pp. 585–593.

[55] Jarrin, N., Prosser, R., Uribe, J. C., Benhamadouche, S., and Laurence, D., 2009, "Reconstruction of Turbulent Fluctuations for Hybrid RANS/LES Simulations using a Synthetic-Eddy Method," Int. J. Heat Fluid Flow, 30, pp. 435–442.

[56] Keating, A., Piomelli, U., Balaras, E. and Kaltenbach, H.-J., 2004, "A Priori and A Posteriori Tests of Inflow Conditions for Large Eddy Simulation," Phys. Fluids (1994-present), 16(12), pp. 4696–4712.

[57] Spille-Kohoff, A., Kaltenbach, H.-J., 2001, "Generation of Turbulent Inflow Data with a Prescribed Shear-stress Profile," In: Liu, C., Sakell, L., Beutner, T. (eds.), DNS/LES Progress and Challenges, Proceedings of the Third AFOSR International Conference on DNS/LES, pp. 319–326. Greyden press, Columbus.

[58] De Laage de Meux, B., Audebert, B., Manceau, R. and Perrin, R., "Anisotropic Linear Forcing for Synthetic Turbulence Generation in Large Eddy Simulation and Hybrid RANS/LES Modeling," Phys. Fluids, 27, 035115.

[59] Luke, E. A., Tong, X., and Chamberlain, R., 2016 "FlowPsi: An Ideal Gas Flow Solver-The User Guide," https://github.com/libm3l/FlowPsi, pp. 29-40.

[60] Subbareddy, P. K., and Candler, G. V., 2009, "A Fully Discrete, Kinetic Energy Consistent Finite-Volume Scheme for Compressible Flows," J. Comp. Phys., 228(5), pp.1347-1364.

[61] Smagorinsky, J., 1963, "General Circulation Experiments with the Primitive Equations," Mon. Weath. Rev., 91(3), pp. 99-164.

[62] Fureby, C., and Grinstein, F. F., 1999, "Monotonically

Integrated Large Eddy Simulation of Free Shear Flows," AIAA J., 37(5), pp. 544-556.

[63] Germano, M., 1986, “Differential filters for the large eddy numerical simulation of turbulent flows,” Phys. Fluids 29, pp. 1755–1766.

[64] Tangermann, E., and Klein, M., 2020, “Controlled Synthetic Freestream Turbulence Intensity Introduced by a Local Volume Force,” J. Fluids 2020, 5(3), pp. 130.

[65] Shobayo, O.O., and Walters, D.K., 2020, “Evaluation of a Statistically Targeted Forcing Method for Synthetic Turbulence Generation in Large-Eddy Simulations and Hybrid RANS-LES Simulations,” ASME 2020 FEDSM conf. : July 13–15, doi.org/10.1115/FEDSM2020-20376, V003T05A043.

[66] Shobayo, O.O., and Walters, D.K., 2019 "Hybrid RANS-LES Simulation of Turbulent Heat Transfer in a Channel Flow with Imposed Spanwise and Streamwise Mean Temperature Gradient." ASME-JSME-KSME 2019 8th Joint Fluids Engr. Conf. Vol. 2: V002T02A052, doi.org/10.1115/AJKFluids2019-4920

[67] Liepmann H. W., and Laufer J., 1947 “Investigations of Free Turbulent Mixing,” NACA Tech. Note TN 1257.

[68] Wygnanski I., and Fiedler H. E., 1970 “The Two-dimensional Mixing Region,” J. Fluid Mech. 41, 327.

[69] Spencer B. W., and Jones B. G., 1971 “Statistical Investigation of Pressure and Velocity Fields in the Turbulent Two-stream mixing layer,” AIAA Paper No. 71-613.

[70] Batt R. G., 1977 “Turbulent Mixing of Passive and Chemically Reacting Species in a Low-speed Shear Layer,” J. Fluid Mech. 82, 53 .

[71] Bell J. H., and Mehta R. D., 1990 “Development of a two-stream mixing layer from tripped and untripped boundary layers,” AIAA J. 28, 2034 .

[72] Rogers M. M., and Moser R D., 1993 “The Three-dimensional Evolution of a Plane Mixing Layer: The Kelvin-Helmholtz Rollup,” J. Fluid Mech. 243, 183.

[73] Rogers, M. M., and Moser, R. D., 1994 “Direct Simulation of a Self-similar Turbulent Mixing Layer. Phys. Fluids 6, 903–923.

[74] Pantano, C., and Sarkar, S., 2002 “A Study of Compressibility Effects in the High-speed Turbulent Shear Layer using Direct Simulation,” J. Fluid Mech, 451, 329-371.

[75] Rogers M. M., Moser R. D., and Buell J. C., 1990 “A Direct Comparison of Spatially and Temporally Evolving Mixing Layers,” Bull. Am. Phys. Sot. 35, 2294 .

[76] Schmidt, S., Breuer, M., 2016 “Source Term Based Synthetic Turbulence Inflow Generator for Eddy-resolving predictions of an Airfoil flow including a Laminar Separation Bubble.,” Comput. Fluids, 146, pp. 1–22, doi: 10.1016/j.compfluid.2016.12.023.

[77] Klein, M., Chakraborty, N., Ketterl, S., 2017 “A Comparison of Strategies for Direct Numerical Simulation of Turbulence Chemistry Interaction in Generic Planar Turbulent Premixed Flames,” Flow Turbul. Combust., 99, pp. 955–971, doi:10.1007/s10494-017-9843-9.

[78] Spalart, P. R., and Watmuff, J. H., 1993 “Experimental and Numerical Study of a Turbulent Boundary Layer with Pressure Gradients,” J. Fluid Mech., 249, pp. 337– 371.

[79] Wu X., 2017 “Inflow Turbulence Generation Methods,” Annu. Rev. Fluid Mech., 49, pp. 23-49.

[80] Morgan, B., Larsson, J., Kawai, S., Lele, S.K., 2011 “Improving Low-frequency Characteristics of Recycling/rescaling Inflow Turbulence Generation,” AIAA J., 49(3), pp. 582–597.

[81] Dhamankar, N.S., Blaisdell, G.A., Lyrintzis, A.S., 2015 “An Overview of Turbulent Inflow Boundary Conditions for Large Eddy Simulations,” 22nd AIAA comp. fluid dynamics conf., 2015. AIAA Paper 2015–3213.